Numerical Modeling of Compressible Two-Phase Flows with a Pressure-Based Method

A thesis accepted by the
Faculty of Aerospace Engineering and Geodesy
of the Universität Stuttgart
in partial fulfillment of the requirements for the degree of
Doctor of Engineering Sciences (Dr.-Ing.)

by

Markus Boger

born in Heilbronn

Main-referee	:	Prof. Dr. rer. nat. Claus-Dieter Munz
Co-referee	:	Prof. Dr.-Ing. Michael Dumbser
Date of defence	:	5 December 2013

Institute of Aerodynamics and Gas Dynamics
University of Stuttgart

2014

Für meine Eltern

I am always doing that which I can not do, in order that I may learn how to do it.
Pablo Picasso

Jede Lösung eines Problems ist ein neues Problem.
Johann Wolfgang von Goethe

Preface

This thesis is the result of four years of work as academic employee at the Institute of Aerodynamics and Gas Dynamics (IAG) at the University of Stuttgart.

First of all, I want to thank my doctoral supervisor Prof. Dr. Claus-Dieter Munz for giving me the opportunity to develop this dissertation in his research group and for providing me with excellent working conditions and scientific freedom. Furthermore, I thank Prof. Dr. Michael Dumbser for being co-referee.

For the pleasant working atmosphere I want to thank all my colleagues at the IAG. Special thanks to Dr. Felix Jaegle for all the fruitful discussions in the field of multiphase flows.

Thanks also to my colleagues from the Institute of Aerospace Thermodynamics (ITLR) at the University of Stuttgart for providing me with support for my work with the FS3D code, particularly Philipp Rauschenberger and Dr. Jan Schlottke.

This work was financed by the Deutsche Forschungsgemeinschaft (DFG) in the context of the Stuttgart Research Center for Simulation Technology (SimTech).

Last but not least, I want to express my gratitude to everyone who supported me during the last years, especially my family.

Stuttgart, 15 February 2014

Markus Boger

Contents

Symbols

b	Covolume
c	Speed of sound
C	Courant number
e	Total energy per unit volume
e_{kin}	Kinetic energy
f	Volume fraction of the liquid phase
$\vec{f}_\gamma$	Capillary force
H	Height function
i, j, k	Cell indices
$\boldsymbol{I}$	Unity matrix
k_0	Stiffness parameter of the Tait equation of state
$\vec{k}$	Specific body force
M	Mach number
m	Wave slope
n	Time level
$\vec{n}$	Normal vector
p	Pressure
p^*	Pressure in the vicinity of the compressible-incompressible interface
p_∞	Stiffness parameter of the stiffened gas equation of state
p_0	Reference pressure of the Tait equation of state
$p^{(0)}$	Thermodynamic background pressure
$p^{(2)}$	Hydrodynamic pressure
$p^{(2)*}$	Predictor of the hydrodynamic pressure of the MPV scheme
$p^{(2)'}$	Pressure in a $M = 0$ flow region, combining thermodynamic and hydrodynamic pressure
q	Time step ratio of the SBDF method
r	Ratio of wave speeds
R	Droplet radius

s	Slope for the spatial reconstruction (MUSCL approach)
t	Time
T	Oscillation period
$\boldsymbol{T}$	Capillary pressure tensor
u, v, w	Velocity components
$\vec{U}$	Vector of conservative variables
v^*	Velocity in the vicinity of the compressible-incompressible interface
$\vec{v}$	Velocity vector
$\vec{v}^*$	Predictor velocity of the MPV scheme
$\tilde{\vec{v}}$	Predictor velocity of the FS3D code
$\vec{W}$	Vector of primitive variables
x, y, z	Spatial coordinates
$\vec{x}$	Vector of spatial coordinates

Greek symbols

γ	Adiabatic exponent
δ_S	Delta function concentrated on the surface
$\delta\vec{v}$	Velocity corrector of the MPV scheme
$\delta p^{(2)}$	Pressure corrector of the MPV scheme
Δt	Time step
$\Delta x, \Delta y, \Delta z$	Length of the computational cell edges
ϵ	Specific internal energy
κ	Curvature
μ	Dynamic viscosity
ρ	Density
ρ_0	Reference density of the Tait equation of state
ρ^*	Density in the vicinity of the compressible-incompressible interface
$\rho^{(0)}$	Thermodynamic background density
σ	Surface tension coefficient
Φ	Level set variable

ω	Angular frequency
Ω	Spatial domain

Subscripts

ref	Reference value

Superscripts

$'$	Dimensionless value
ex	Explicit
im	Implicit

Abbreviations

AUSM	Advection Upstream Splitting Method
BC	Boundary condition
CFD	Computational fluid dynamics
CFL	Courant-Friedrichs-Lewy
CSF	Continuum surface force
CSS	Continuum surface stress
CV	Control volume
DG	Discontinuous Galerkin
DNS	Direct Numerical Simulation
FS3D	Free Surface 3D
IC	Initial condition
MAC	Marker and cell
MPV	Multiple Pressure Variables
MUSCL	Monotone Upstream-centered Schemes for Conservation Laws
ODE	Ordinary differential equation
PDE	Partial differential equation
PLIC	Piecewise linear interface calculation
RK2CN	Runge-Kutta second order Crank-Nicolson time discretization
SBDF	Semi-implicit backward differentiation formula
VOF	Volume of fluid

Kurzfassung

Diese Arbeit beschäftigt sich mit der direkten numerischen Simulation (DNS) kompressibler und inkompressibler Mehrphasenströmungen und hat als Ziel die Erweiterung eines inkompressiblen Zweiphasenlösers in den Bereich kompressibler Strömungen.

Ausgangspunkt ist der existierende Mehrphasenlöser FS3D zur Simulation dreidimensionaler, inkompressibler Strömungen. Für diesen Code wird die Modellierung der Oberflächenspannung im Hinblick auf die sogenannten parasitären Strömungen detailliert untersucht. Hierbei handelt es sich um numerisch verursachte, unphysikalische Geschwindigkeiten. Es wird gezeigt, dass ihr Ausmaß durch die Verwendung einer geeigneten numerischen Approximation (Balanced-Force-Diskretisierung) um mehrere Größenordnungen reduziert werden kann.

Der Schwerpunkt der Arbeit liegt auf der Erweiterung des inkompressiblen, druckbasierten numerischen Verfahrens in den Bereich kompressibler Mehrphasenströmungen. Hierzu werden sowohl der physikalische als auch der mathematische Hintergrund der Gleichungen für kompressible und inkompressible Strömungen diskutiert und es wird der Übergang von kompressibler zu inkompressibler Strömung aufgezeigt. In diesem Zusammenhang werden grundlegende eindimensionale Untersuchungen zur Kopplung kompressibler und inkompressibler Strömungsgebiete präsentiert. Basierend auf diesen Betrachtungen werden mehrere iterative Kopplungsmethoden abgeleitet und anhand von Testrechnungen validiert.

Das Multiple-Pressure-Variables-Verfahren (MPV) wird vorgestellt, welches die Erweiterung inkompressibler Löser in den kompressiblen Bereich ermöglicht. Das Verfahren beruht auf einer asymptotischen Druckzerlegung, welche die unterschiedliche Bedeutung des Druckes für kompressible und inkompressible Strömungen berücksichtigt. Auf diese Weise ist der inkompressible Grenzwert der kompressiblen Gleichungen definiert und nicht singulär. Die MPV-Methode wird zunächst für kompressible, einphasige Strömungen eingeführt und anschließend auf kompressible Mehrphasenströmungen erweitert. Hierbei spielt die Behandlung der Phasengrenzfläche und der dort auftretenden Sprünge in den Materialeigenschaften und Zustandsgleichungen eine zentrale Rolle. Während das abgeleitete druckbasierte Verfahren den Dichtesprung zwischen den

beiden Phasen verschmiert, weist die Thermodynamik einen scharfen Sprung über die Phasengrenze hinweg auf. Im Gegensatz zu vielen dichtebasierten Mehrphasenlösern leidet das MPV-Verfahren nicht unter Druck- und Geschwindigkeitsoszillationen am Ort der Phasengrenze. Dies lässt sich auf die Verwendung des Druckes als primäre Variable zurückführen, was im Rahmen einer detaillierten Analyse des numerischen Verfahrens gezeigt wird. Die MPV-Methode wird durch mehrere ein- und zweiphasige, eindimensionale Riemannprobleme validiert. Hierbei liegt der Fokus für die einphasigen Strömungen auf Untersuchungen, die die Shock-Capturing-Eigenschaften des Verfahrens und seine Fähigkeit zur Simulation von Wellenausbreitung betreffen. Das MPV-Verfahren zeigt dabei, dass es sowohl für ein- als auch für zweiphasige Riemannprobleme sehr gute Ergebnisse liefert. Abschließend werden Simulationsergebnisse von dreidimensionalen Stoß-Tropfen-Interaktionen präsentiert.

Abstract

This work is directed towards the direct numerical simulation (DNS) of compressible and incompressible multiphase flows. The main objective is the extension of an incompressible two-phase solver to the compressible flow regime.

The starting point is the existing multiphase solver FS3D for the simulation of three-dimensional, incompressible flows. For this code, the topic of surface tension modeling is looked at in detail with respect to the so-called parasitic currents. These spurious, unphysical velocities are caused by the numerical approximation of surface tension and a balanced-force algorithm is presented that considerably reduces the parasitic currents by several orders of magnitude.

The main focus of this thesis is on the extension of an incompressible, pressure-based numerical approach to the simulation of compressible multiphase flows. For this purpose, the physical and mathematical background of the governing equations for incompressible and compressible flows is discussed and the transition from the compressible to the incompressible regime is addressed. In this context, fundamental investigations for the coupling of compressible and incompressible flow regions are presented in one space dimension. On the basis of these considerations, several iterative coupling schemes are derived and validated with the help of generic test cases.

The pressure-based Multiple Pressure Variables (MPV) method that allows the extension of an incompressible flow solver to the compressible regime is presented. The numerical scheme builds upon an asymptotic pressure decomposition taking into account the different roles of pressure for incompressible and compressible flows. This avoids the singular incompressible limit of the compressible flow equations. At first, the MPV method is introduced for single-phase flows. Then its extension to compressible two-phase flows is presented. In this context, the treatment of the material interface between the two fluids and the corresponding jump in the material properties and the equations of state play a crucial role. While the present approach numerically smears the density jump between the two phases, the thermodynamic transition is a sharp one. Contrary to many density-based two-phase flow solvers, the MPV scheme does not suffer from oscillations in pressure and velocity at the interface location due to the use of pressure as primary variable. A detailed analysis of this behavior is presented. Finally, the MPV scheme proves to accurately solve one-dimensional single- and two-phase Riemann problems. For the single-phase

flows, the focus is on the wave propagation and shock-capturing properties of the MPV method. In three space dimensions, the numerical scheme is successfully applied to the computation of shock-droplet interactions.

1. Introduction

The focus of this work is on the simulation of multiphase flows characterized by the presence of a gas-liquid interface that separates two immiscible fluids. This kind of flow contains gas and liquid at the same time where the components may be from a single fluid that is present in its gaseous and liquid phase or they come from different fluids. Yet, in the context of the present thesis phase changes are not taken into account. Apart from gas-liquid interfaces, it is also possible to have liquid-liquid interfaces between different immiscible liquids like oil and water. However, although being in principle accessible by the presented numerical methods, the latter are not within the scope of research of this work. In the following, a short motivation is given that illustrates the significance of multiphase flows in nature and technical applications and it is explained why their numerical investigation is of special interest. Then, a general overview over the prerequisites of numerical simulations is given. The different steps of a numerical simulation are clarified in general and for the simulation of multiphase flows in particular. Afterwards, an introduction to the numerical simulation of two-phase flows is given, including references to already existing work in the literature. Finally, the objectives of this work are listed and an outlook on the structure of this thesis is given.

1.1. Motivation

Multiphase flows are omnipresent in daily life and a lot of examples can be found with regard to their occurrence in nature and in technical applications.

Two-phase flows with a gas-liquid interface play an important role in meteorology for the investigation of clouds and rain drops. Another relevant phenomenon is groundwater flow, where the flow of an air-water mixture through the porous soil is studied. Fundamental processes of the oil production are also described by multiphase flows, as the oil coming from the underground is usually mixed with gas. An example that includes two liquids is the oil propagation after an oil spill in the ocean.

Some technical applications come from the field of power plants. Here, the design of boilers used for the steam production to drive turbines and the cooling of nuclear reactors are examples that include multiphase flows. Cavitation is another important phenomenon that has to be taken into account for the construction of pumps, valves and hydraulic systems, for example. Cavitation is induced in such devices if the pressure locally drops below the vapor pressure limit. In such a case, phase change occurs and gas bubbles are created. Their presence influences the functioning of the device and the bubble collapse may additionally cause drastic damages.

Liquid sprays are of special interest for many technical processes in divers fields. They range from applications in the food industries, agriculture and painting to medical sprays. However, one of the most important field of application is the fuel injection into combustion engines and a lot of effort has already been spent in understanding fuel atomization and evaporation.

This list is long enough to prove the importance of multiphase flows and the strong interest linked to their investigation, but it is far from being complete and a lot more examples can be found.

The experimental investigation of two-phase flows is very often difficult and cumbersome. There is only limited access to measure the temperature and pressure distribution inside droplets and gas bubbles and it is also hard to determine an internal velocity distribution there. This is the reason why numerical simulations are quite appealing for the investigation of two-phase flows.

In general, the last decades have shown a strong increase in the development and application of numerical methods in the academic and industrial context. There is a trend to combine numerical simulations with experiments, such that the expensive experimental investigations can be reduced to a minimum and may partially be replaced by numerical computations. This development is driven by the steadily growing computer performance. In comparison to an experimental investigation, numerical simulations very often give faster results and are cheaper. This leads to a strong interest to intensify the development of new numerical approaches for computational fluid dynamics (CFD), including the simulation of multiphase flows that are even more complex to handle on the numerical level than standard single-phase flows.

The following section provides a brief introduction to the structure of CFD simulations, where the focus is on the simulation of multiphase flows.

1.2. Numerical flow simulation

To perform a numerical simulation, different steps are required that can be summarized in a simulation chain, following Hirsch [1]. It will be shown that each part of the simulation chain introduces errors and uncertainties to the numerical approach. Models and assumptions are introduced that often contain simplifications to the real world phenomenon and that are characterized by empiricism. Therefore, the results of a numerical simulation can never be completely in accordance with the real world, as there always remains a certain, often undefined, level of error. This fact has to be taken into account when the final simulation results are judged and interpreted. The simulation chain is displayed in a schematic picture in Fig. 1.1 and the corresponding steps are described in the following

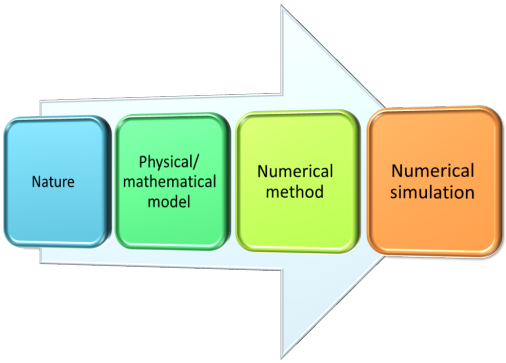

Figure 1.1.: The simulation chain.

1.2.1. Simulation chain

The first step in the simulation chain is the description of fluid flows in nature by physical models. This is done choosing the appropriate flow equations. In the context of most CFD simulations, the flow phenomena can be described by the viscid Navier-Stokes equations or the inviscid Euler equations. In order to stay as close as possible to the real world phenomena described by the equations, a direct numerical simulation (DNS) shall be performed for the subsequent in-

vestigations. This means that the equations are solved directly without further simplifications or the introduction of additional physical models.
In a next step, these equations are looked at in more detail. Generally, they are sets of nonlinear partial differential equations that are not easy to handle from a mathematical point of view. Because of their nonlinearity, they allow discontinuities like shock waves and a general analytical solution for such a three-dimensional set of equations is not available.
The solution of the equations requires the discretization of the mathematical model and the use of numerical methods. For this purpose, the equations are discretized in space on a computational mesh, such that the continuity in space is replaced by a finite number of points or control volumes. On this mesh, the equations have to be evaluated and this includes the introduction of discrete quantities as well as the discrete evaluation of their derivatives. If the scope of research is on unsteady phenomena, a temporal discretization is needed, too.
Once all these aspects have been taken care of, a numerical simulation can be performed. The knowledge of the assumptions, simplifications and resulting limitations of all the above steps is crucial to obtain reliable computational results and to be able to reasonably interpret them. It should be clear that every physical model just describes a part of nature and is restricted to the particular assumptions and circumstances it is based on. Furthermore, the numerical discretization introduces additional limitations.
In the following, the different parts of the simulation chain are discussed in more detail in the context of this thesis. It is shown that this work addresses all chain links ranging from basic considerations of the physical and mathematical modeling of nature to a detailed analysis of a numerical discretization scheme and its properties.

1.2.1.1. Physical and mathematical modeling

The choice of the physical model for two-phase flows is not trivial as is illustrated below.
Generally, the flow can be described by the Navier-Stokes or the Euler equations, where the latter exclude viscous effects and heat conduction. Both of them are sets of partial differential equations that describe the conservation of mass, momentum and energy. Including viscosity and heat conduction, the Navier-Stokes equations are closer to the real world phenomena than the Euler equations. However, the simplifications of the Euler equations are justified for certain flow regimes. This is for example the case when gas dynamic effects like shock waves are dominant and the influences of viscosity are negligible.

For such flows, the results of the Euler and the Navier-Stokes equations are virtually identical to each other and this justifies the use of the simpler Euler equations that are easier to handle from a numerical point of view. But once viscosity is getting more important, the Euler equations give wrong results and it is necessary to switch to the Navier-Stokes equations.
To make things even more complex, both sets of equations can be used in a compressible or incompressible formulation characterized by different underlying physical assumptions. In the case of a compressible flow, the conservation equations for mass, momentum and energy are coupled and the resulting system is closed by an equation of state that relates pressure, density and internal energy to each other and therefore thermodynamically characterizes a fluid. For the incompressible flow equations, hydrodynamics is decoupled from thermodynamics. This corresponds to the decoupling of the energy equation from the mass and momentum conservation equations. The incompressible flow equations only take into account hydrodynamic effects, as only the mass and momentum equations are solved. This separates internal and kinetic energy from each other and the incompressible fluid is not described by an equation of state. The energy equation finally degenerates to a transport equation in the absence of heat conduction.
Furthermore, the role of pressure is different for compressible and incompressible flows. In the compressible flow regime, the pressure has a hydrodynamic and a thermodynamic meaning, it has to obey an equation of state. For an incompressible flow, the pressure loses its thermodynamic importance as there is no equation of state. It is of purely hydrodynamic nature and has to guarantee that the zero divergence constraint of the velocity is satisfied.
All these simplifications for the incompressible regime are justified if the flow is dominated by hydrodynamic effects as it is the case for low speed flows with small pressure and temperature gradients.
From a mathematical perspective, the difference between the compressible and the incompressible flow equations is also of interest. The inviscid compressible equations are of hyperbolic nature while their incompressible counterpart is hyperbolic-elliptic. This has direct consequences on the physical phenomena that are captured by the equations. The propagation of pressure waves can be described with the hyperbolic compressible equations. However, the incompressible flow equations are of elliptic nature implying that pressure waves move infinitely fast and that they cannot be simulated in this context.
This gives a first impression that it is important to know about the basic assumptions and limitations of the flow equations. Moreover, the different mathematical properties require different numerical approaches as is pointed

out in the following section.

1.2.1.2. Numerical methods

A lot of different numerical schemes are available for CFD computations. All of them have their advantages and drawbacks. In the context of this thesis, the interest is in the simulation of compressible and incompressible flows and for this purpose, the flow solvers can be classified into two categories: density- and pressure-based methods.
Incompressible flows are solved with pressure-based approaches. For such a method, pressure is the primary variable. Usually, a Poisson equation for pressure is solved and the velocity update is performed on the basis of the new pressure values [1, 2]. In contrast, a density-based solver is commonly employed to solve the compressible flow equations. These methods use density as primary variable and solve the conservation equations of mass, momentum and energy. Pressure is then determined via density and energy that are inserted into the equation of state.
With respect to the spatial and temporal discretization, the two approaches differ as well. While a collocated grid arrangement is used for the density-based solvers, many pressure-based methods use a staggered grid arrangement that facilitates the evaluation of the pressure Poisson equation [3]. The temporal discretization is usually purely explicit or implicit for the density-based methods. Pressure-based methods often employ a semi-implicit time discretization where the convective terms are treated in an explicit manner while the elliptic Poisson equation has to be solved in an implicit way.
In general, density-based schemes have problems to approach the incompressible limit. This limit is singular, the role of pressure changes, kinetic and internal energy are decoupled and the system of equations gets stiff. It is possible to avoid this stiff behavior introducing an asymptotic expansion of the pressure [4–7] and corresponding numerical schemes have already been proposed in literature [7–11]. They allow the extension of incompressible pressure-based flow solvers to the compressible regime. The so-called multiple pressure variables (MPV) approach [7,10,11] is such a method and it is used in the following to compute compressible flows with a pressure-based method.

1.2.1.3. Numerical simulations

In a last step, the numerical methods are applied to the real world phenomenon of interest by starting the computation. The corresponding computational re-

sults can then be post-processed and visualized and the outcome may be interpreted physically. For this interpretation, the above discussed simplifications and characteristics of the numerical schemes have to be kept in mind.
In the case of the present work, one- and three-dimensional simulations have been performed. Their focus has been on the validation and verification of the developed numerical methods for two-phase flows and not on large scale high performance computing. For some of the one-dimensional calculations, exact analytical solutions have been available and they are compared to the numerical results in order to assess the computational methods.
After this general description of the CFD simulation process, the following section provides a more detailed introduction to the DNS of two-phase flows including the resolution of the material interface.

1.3. Direct numerical simulation of two-phase flows with interface resolution

The simulation of multiphase flows is characterized by large jumps in the material properties across the interface separating two phases. An additional difficulty is the resolution and tracking of the interface itself. Both issues are of crucial importance for incompressible and compressible flows.
A lot of work has already been done in the field of interface tracking. Different methods have been introduced, each of them has its specific strengths and weaknesses. Following [12] the schemes can be grouped into two categories, the first group consists of the so-called moving and adaptive grid methods and the second group comprises the fixed grid methods.
For a moving grid method, the grid cell boundaries are always aligned to the interface. This allows to accurately separate the different phases from each other. Every grid cell only contains one fluid type and the solution of the corresponding flow equations can be done separately for each fluid. The interaction between the fluids is controlled by explicit jump conditions at the interface location. A variety of such schemes can be found in [12] and more recently Nguyen *et al.* [13] proposed a discontinuous Galerkin (DG) method on adaptive, interface-aligned grids. A considerable disadvantage of such methods is the constant remeshing that has to be performed when the interface is moving, as the mesh generation is quite expensive and cumbersome. Topology changes like they occur during the breakup and merging of interfaces are also very difficult to handle for these methods.
For the fixed grid methods the interface is not aligned to the cell boundaries.

Different classes of fixed grid methods exist. In particle methods, marker particles are placed at the location of the interface. These particles are advected by the fluid velocity in a Lagrangian way [12,14]. The interface can be tracked accurately by this approach, but the treatment of interface breakup and merging is difficult. Another widespread method for incompressible flows is the volume of fluid (VOF) approach of Hirt and Nichols [15] described in more detail in section 2.7.1. The basic idea of the VOF method is to indirectly capture the interface by tracking the volume fraction of the different phases. The interface geometry has then to be reconstructed on the basis of the volume fractions. This method can only be applied to incompressible flows in its original form, as it is based on volume conservation that is not guaranteed for compressible flows. The level set approach [16,17] (cf. section 2.7.2 for more details) represents the interface by the zero level set of a continuous function that is often equivalent to a signed distance function in relation to the interface. This method also captures the interface in an indirect way, but it is applicable to incompressible as well as compressible flows. It can easily be implemented numerically, however special care has to be taken in order to guarantee that the level set function remains a distance function during the computation [17]. Moreover, the level set method is known to be not strictly mass-conserving. So far, a lot of effort has been spent to improve the mass conservation properties of the level set method. The proposed remedies include the discretization of the level set function by a high-order numerical scheme [18,19] as well as the use of local grid refinement in the vicinity of the interface [20,21]. There also exist level set methods for incompressible flows that use the VOF method to minimize the mass losses [22–24].
There are various physical phenomena that are linked to the interface topology and its location, like surface tension and evaporation. The effects of the capillary forces can be included in the incompressible flow equations using well-established surface tension models [25, 26]. However, special attention has to be paid to a correct, balanced-force implementation of the models in order to prevent unphysical spurious velocities [27]. These spurious currents are caused by discretization errors of the surface tension force and an inaccurate estimation of the surface curvature. In the context of this work, the implementation of a balanced-force surface tension model is presented that effectively reduces the spurious currents by several orders of magnitude. It follows the discretization of François *et al.* [27] and uses a curvature estimation based on the height function approach of Popinet [28].
For incompressible flows thermodynamic effects are not taken into account by the flow equations and therefore evaporation processes cannot be described by

an equation of state and have to be modeled [29]. However, this modeling is only admissible in a certain range of temperature and pressure. Once there are important temperatures and pressures, the compressible flow equations have to be used in order to correctly simulate the flow under extreme ambient conditions. In the following, the differences between incompressible and compressible two-phase flow simulations are addressed.
The DNS of two-phase flows including the resolution of the material interface is often performed on the basis of the incompressible Navier-Stokes equations. Typical technical applications concern droplets in an air environment at ambient pressure. In such a configuration, the liquid itself can be considered to be almost incompressible. Usually, the droplets are moving at low speed, such that the compressibility of the gas can also be neglected. Under these circumstances the use of the incompressible flow equations is justified: kinetic and internal energy are decoupled resulting in the separation of thermodynamics and hydrodynamics. In the absence of phase change, such flows are dominated by hydrodynamics and an equation of state is not needed as the thermodynamic state of the fluid is virtually constant. However, in the case of droplets at high speed at least the gaseous phase should be described by the compressible flow equations.
If the propagation of pressure waves inside the droplet is not of interest, it might be favorable to treat the liquid as incompressible while the compressibility effects are only taken into account in the gas phase. Such a treatment avoids small time steps as the fast pressure waves inside the liquid are not resolved by the numerical scheme and therefore do not slow down the computation. In the course of this work, a fundamental one-dimensional investigation for such a compressible-incompressible coupling is carried out in the absence of phase change and surface tension. The incompressible liquid domain can be described by the analytical solution of the one-dimensional incompressible Euler equations. The coupling to the compressible flow is established in an iterative way, based on jump conditions for pressure and velocity across the interface and the solution of a half-Riemann problem on the compressible side of the interface. At the interface location, the coupling algorithms deliver the numerical flux terms to the adjacent compressible flow solver, similar to a boundary condition. To take care of the different meaning that pressure has for compressible and incompressible flows, the pressure decomposition of the MPV approach is used [7, 10, 11]. Different coupling schemes are presented taking into account the effects of hydrodynamics, thermodynamics and a combination of both.
In the context of fuel injection processes, more extreme ambient conditions have to be faced that are characterized by an augmented pressure and temperature.

Especially for strong pressure and temperature gradients in the flow field, the thermodynamic description of the fluids by an equation of state can no longer be neglected and has to be taken into account by the numerical simulation in order to get accurate results. This requires the use of the compressible flow equations for both phases.
For the simulation of fully compressible multiphase flows additional difficulties come into play. Besides the large jumps in the material properties, the equation of state is different on either side of the material interface. As the fluids can differ significantly in their properties, their equations of state are also very dissimilar in nature. In this context, problems may arise due to the numerical smearing of the density across the material interface. The interface represents a contact discontinuity that is smeared over several grid cells by standard shock-capturing schemes. When the smeared density is inserted into the different equations of state an unphysical pressure is caused. From a mathematical point of view, this represents a stiff problem and the change in the equation of state is very challenging as it results quite often in spurious pressure and velocity oscillations in the vicinity of the interface. To prevent these oscillations several interface treatment approaches have been derived that can be grouped into two categories: diffuse and sharp interface methods.
Sharp interface approaches treat the interface as a distinct discontinuity. This is equivalent to a discontinuous transition in material properties and in the equation of state. A very popular sharp interface approach is the ghost fluid method of Fedkiw *et al.* [30]. The basic idea of the scheme is to solve two single-phase Riemann problems at the location of the interface in order to avoid problems with unphysical intermediate density values. For this purpose, the interface is tracked by a level set method and ghost cells are introduced in the vicinity of the interface. The ghost values are computed using an entropy based extrapolation and finally a standard Riemann solver can be used to compute the fluxes at the material interface. This approach is oscillation-free for general equations of state and density ratios. However, Liu *et al.* showed that the method has problems to handle strong shocks and they proposed a more robust ghost fluid approach in [31].
On the contrary, the basic idea of diffuse interface methods is a smooth transition between two fluids including a numerical mixing of fluid properties. The difficulty for such methods is to establish a mathematically, physically and numerically consistent mixing. Especially with regard to the different equations of state, the transition has to be realized in a thermodynamically consistent way. The diffuse interface methods can be sub-divided into rather simple methods using a single velocity and pressure distribution in the whole computational

domain for both fluids (one-pressure, one-velocity models) and the more elaborated two-pressure, two-velocity approaches.
Such a one-velocity, one-pressure-model has for example been proposed by Karni, who developed a nonconservative numerical method for the Euler equations in primitive variables [32]. The approach eliminates the spurious oscillations, but due to its conservation errors it is only applicable to shocks of moderate strength. For one-dimensional flows obeying the perfect gas equation of state, Abgrall presented a numerical approach that solves the conservation equations and imposes further conditions on the energy that guarantee that the pressure stays constant across the interface [33]. Given these additional conditions, the scheme is also not fully conservative, but it still allows the calculation of strong shock waves. Saurel and Abgrall extended this method in [34] to multi-dimensions and the more general stiffened gas equation of state that allows the simulation of multiphase problems with liquid and gaseous phases. As is obvious, these models often contain limiting assumptions with respect to their conservation properties and the equations of state that can be used.
A class of more general and sophisticated diffuse interface methods are the two-pressure, two-velocity models that solve the conservation laws for mass, momentum and energy by individual equations for each fluids, where the coupling is established by nonconservative terms in the conservation equations. These schemes build on the Baer-Nunziato model introduced in [35] to describe the deflagration-to-detonation transition in reactive granular materials. Since then, a lot of effort has been put into the enhancement of this approach giving rise to several derivatives of the original method, as they are described for example in [36, 37].
The DNS of compressible multiphase flows is still a very active field of research, where numerous approaches are proposed by several researchers. While there are various ways of treating the interface including the jump in material properties and the equation of state, the majority of the numerical schemes builds upon a density-based flow solver for the underlying flow equations. In contrast, the focus of this thesis is on the DNS of compressible multiphase flows with a pressure-based method.
For this purpose, the MPV method for single-phase flows is extended to the compressible flow regime in the context of multiphase flows. The numerical approach for the extension can be considered as a mixture of diffuse and sharp interface treatment. On the one hand, the thermodynamic transition between the fluids is happening in a sharp manner. On the other hand, the density is numerically smeared. Due to the pressure-based approach, pressure is used as primary variable and this facilitates the prevention of unphysical pressure

oscillations at the interface, as it will be shown. The presented MPV method for multiphase flows can be used to extend incompressible multiphase flow solvers to the compressible regime.

1.4. Objectives

The principal objective of this work is the development of a pressure-based numerical approach for the simulation of compressible multiphase flows. In this context, the following aspects are covered:

- Starting from an existing incompressible multiphase code, the modeling of surface tension and the reduction of parasitic currents are addressed in the context of the incompressible Navier-Stokes equations.
- The relationship between the compressible and the incompressible flow equations is investigated. Fundamental one-dimensional investigations are performed to derive procedures for the coupling of compressible and incompressible flow regions.
- The main focus is on the extension of the pressure-based MPV method to the DNS of compressible two-phase flows including the resolution of the interface.
- The MPV scheme is assessed with respect to single- and two-phase flows.

According to the above introduced simulation chain (cf. Fig. 1.1), this includes work in all of the different fields: The physical and mathematical modeling is addressed by the fundamental investigations for the coupling of compressible and incompressible flow regions. The numerical methods are covered by the investigations concerning the MPV method and its extension to two-phase flows. Moreover, surface tension is related to the physical as well as to the numerical modeling. Finally, the MPV method is assessed by numerical simulations.

1.5. Outline

The outline of this thesis is as follows: In the next chapter the governing equations of this work are introduced and it is shown how the transition from the compressible to the incompressible flow regime can be made. Chapter 3 deals with a fundamental investigation of the coupling of compressible and incompressible flow regions. The differences between the two flow regimes with respect to the physical and mathematical background are discussed and iterative

coupling procedures are presented in one space dimension. Chapter 4 introduces the numerical schemes that are used and extended in this work. This comprises the incompressible FS3D code, including the numerical treatment of surface tension, and the pressure-based MPV method for compressible and incompressible flows with its extension to compressible multiphase flows. The computational results of the numerical schemes in one and three space dimensions are shown and discussed in detail in chapter 5. Chapter 6 summarizes this thesis and provides open questions and an outlook on future work.

2. Equations

The governing equations are introduced in the following. This includes the Euler equations in compressible and incompressible form as well as the incompressible Navier-Stokes equations.
Special attention is paid to the transition from the compressible to the incompressible flow regime. For this purpose an asymptotic pressure decomposition is introduced to avoid the otherwise singular incompressible limit of the flow equations. The one-dimensional Euler equations in the zero Mach number limit are looked at in more detail, as they can be solved analytically. The corresponding solutions for a perfect gas and a Tait fluid are presented. For the incompressible three-dimensional flow regime, the Navier-Stokes equations are given for two-phase flows and the pressure jump due to surface tension at material interfaces is discussed. In the context of the DNS of two-phase flows, two interface tracking methods are described: the VOF approach for incompressible flows and the level set method for incompressible as well as compressible flows.

2.1. The compressible Euler equations

The three-dimensional conservation equations for mass, momentum and total energy are known in compressible gas dynamics as the Euler equations and they describe inviscid flows without gravitational and external forces and heat conduction

$$\frac{\partial \rho}{\partial t} + \nabla \cdot (\rho \vec{v}) = 0\,, \tag{2.1}$$

$$\frac{\partial (\rho \vec{v})}{\partial t} + \nabla \cdot [(\rho \vec{v}) \circ \vec{v}] + \nabla p = 0\,, \tag{2.2}$$

$$\frac{\partial e}{\partial t} + \nabla \cdot [\vec{v}\,(e+p)] = 0\,. \tag{2.3}$$

Here, ρ denotes the density, p the pressure, $\vec{v}$ the velocity, t the time and e the total energy per unit volume. The total energy e consists of the internal

energy ϵ and the kinetic energy

$$e = \rho\epsilon + \frac{1}{2}\rho\left|\vec{v}\right|^2. \tag{2.4}$$

The system (2.1)-(2.3) has to be closed with an equation of state that relates pressure to density and internal energy. For gaseous fluids the perfect gas equation of state is well-known

$$p = (\gamma - 1)(e - \frac{\rho}{2}\left|\vec{v}\right|^2), \tag{2.5}$$

with γ being the adiabatic exponent. In the above formulation, the internal energy already has been replaced by the total energy minus the kinetic energy. For liquids like water, the Tait equation of state is frequently applied

$$p = (\gamma - 1)(e - \frac{\rho}{2}\left|\vec{v}\right|^2) - \gamma(k_0 - p_0), \tag{2.6}$$

where p_0 is a reference pressure and k_0 determines the compressibility of the fluid. However, there also exists the so-called stiffened gas equation of state [34] that combines the two previous equations (2.5)-(2.6) and that is used in the following

$$p = (\gamma - 1)(e - \frac{\rho}{2}\left|\vec{v}\right|^2) - \gamma p_\infty. \tag{2.7}$$

The constant p_∞ characterizes the compressibility of the fluid. It is obvious that equation (2.7) includes the perfect gas equation of state (2.5) by choosing $p_\infty = 0$ as well as the Tait fluid equation of state (2.6) for $p_\infty = (k_0 - p_0)$. The Tait equation of state is also known in the following form that does not include the energy variable

$$p = k_0\left(\left(\frac{\rho}{\rho_0}\right)^\gamma - 1\right) + p_0, \tag{2.8}$$

with ρ_0 as reference density.

2.2. The incompressible Euler equations

For the incompressible case, the three-dimensional Euler equations reduce to the conservation of mass and momentum

$$\frac{\partial\rho}{\partial t} + \nabla\cdot(\rho\vec{v}) = 0\,, \tag{2.9}$$

$$\frac{\partial(\rho\vec{v})}{\partial t} + \nabla\cdot[(\rho\vec{v})\circ\vec{v}] + \nabla p = 0\,. \tag{2.10}$$

The energy equation (2.3) is not needed to describe the flow field, as internal energy and kinetic energy are decoupled for isothermal flows. This corresponds to the decoupling of thermodynamics and hydrodynamics and therefore an equation of state is not present in the case of incompressible flows.
For an incompressible flow, the material derivative of the density is equal to zero:

$$\frac{D\rho}{Dt} = \frac{\partial \rho}{\partial t} + \vec{v} \cdot \nabla \rho = 0. \tag{2.11}$$

The mass conservation equation (2.9) can be rewritten in terms of the material derivative

$$\frac{D\rho}{Dt} + \rho \nabla \cdot \vec{v} = 0, \tag{2.12}$$

such that it is obvious that for an incompressible flow with $\frac{D\rho}{Dt} = 0$ the mass conservation equation reduces to a divergence constraint for the velocity field

$$\nabla \cdot \vec{v} = 0. \tag{2.13}$$

For homogeneous incompressible fluids, the different parts of the material derivative are even independently equal to zero:

$$\frac{\partial \rho}{\partial t} = 0, \tag{2.14}$$

$$\nabla \rho = 0. \tag{2.15}$$

However, the two parts do not have to be equal to zero simultaneously and therefore the density does not necessarily have to be constant. An example for an incompressible flow with varying density are density stratifications in the ocean.
Furthermore, the incompressible, zero Mach number limit of the compressible Euler equations shows that the density is also allowed to vary temporally while it is spatially constant in the considered control volume. This is equivalent to a global compression of the control volume and results in a nonzero divergence constraint for the velocity. This notion of a zero Mach number flow is introduced in detail by the following asymptotic considerations for the transition from the compressible to the incompressible regime and the corresponding zero Mach number equations.

2.3. The transition from compressible to incompressible flow

For small Mach numbers $M \to 0$ the compressible equations (2.1)-(2.3) approach the incompressible limit case. However, the incompressible limit of the above system is singular as the speed of sound and the flow velocity differ by several orders of magnitude. The singular behavior is more obvious from the dimensionless compressible Euler equations that are obtained using the following set of non-dimensional variables:

$$x' = \frac{x}{x_{ref}}, \quad \rho' = \frac{\rho}{\rho_{ref}}, \quad \vec{v'} = \frac{\vec{v}}{|\vec{v}_{ref}|}, \quad p' = \frac{p}{p_{ref}}, \quad t' = \frac{t\,|\vec{v}_{ref}|}{x_{ref}}, \tag{2.16}$$

where the subscript *ref* denotes the reference values and $'$ marks the dimensionless variables.

Usually, the compressible equations are non-dimensionalized choosing the reference pressure as $p_{ref} = \rho_{ref}\,|\vec{v}_{ref}|^2$. However, in the present case the pressure is attributed an independent reference value to take into account the scale differences of fluid velocity and speed of sound when the incompressible limit is approached. While the fluid velocity has its own reference velocity $\vec{v}_{ref}$ the speed of sound is non-dimensionalized by

$$c_{ref} = \sqrt{\frac{p_{ref}}{\rho_{ref}}}. \tag{2.17}$$

Together with the reference velocity $\vec{v}_{ref}$, a parameter called global flow Mach number M can be introduced

$$M = \frac{|\vec{v}_{ref}|}{\sqrt{p_{ref}/\rho_{ref}}}, \tag{2.18}$$

that determines the compressibility of the flow. The parameter M directly relates the reference velocities for the flow velocity $\vec{v}_{ref}$ and the speed of sound c_{ref} that are of the same order of magnitude for compressible flows, hence the Mach number parameter is equal to one. For incompressible flows, the Mach number parameter tends to zero as the speed of sound approaches infinity.

Inserting these non-dimensional variables into the Euler equations (2.1)-(2.3),

the following system is obtained

$$\frac{\partial \rho'}{\partial t'} + \nabla \cdot (\rho' \vec{v'}) = 0\,, \tag{2.19}$$

$$\frac{\partial (\rho' \vec{v'})}{\partial t'} + \nabla \cdot \left[(\rho \vec{v'}) \circ \vec{v'} \right] + \frac{1}{M^2} \nabla p' = 0\,, \tag{2.20}$$

$$\frac{\partial e'}{\partial t'} + \nabla \cdot \left[\left(e' + p' \right) \vec{v'} \right] = 0\,. \tag{2.21}$$

The non-dimensional conservation equations for mass and energy still look the same, but the Mach number parameter M appears in the momentum equation (2.20). It is obvious that the equation is stiff for small values of M and that the incompressible limit $M \to 0$ is even singular and has to be further investigated. The superscript $'$ of the dimensionless variables is omitted in the following.

2.3.1. Asymptotic pressure decomposition

In order to get more insight into the incompressible limit, an asymptotic expansion of the primitive flow variables $\vec{W}$ in dependence of the global flow Mach number has been introduced by several authors in literature [4–6]

$$\vec{W} = \vec{W}^{(0)} + M\vec{W}^{(1)} + M^2\vec{W}^{(2)} + \ldots \qquad \text{with} \quad \vec{W} = (\rho, \vec{v}, p). \tag{2.22}$$

The asymptotic considerations for the low Mach number limit show that the leading order terms of density and velocity converge to their incompressible counterpart. Whereas the pressure splits into two main parts in dependence of the global Mach number M:

$$p(\vec{x}, t) = p^{(0)}(t) + M^2 p^{(2)}(\vec{x}, t). \tag{2.23}$$

The leading order pressure term $p^{(0)}$ is spatially constant and satisfies the equation of state in the limit case $M = 0$. It may be considered as a thermodynamic background pressure in such a zero Mach number region. The pressure $p^{(2)}$ is the hydrodynamic pressure of the $M = 0$ limit equations and guarantees the divergence constraint for the velocity.
The pressure decomposition is now introduced into the Euler equations (2.19)-(2.21). From the momentum equation (2.20) it can be seen that due to the pressure splitting, the term $\frac{1}{M^2}\nabla p$ in the compressible equations remains bounded in the zero Mach number limit and tends to $\nabla p^{(2)}$. In order to further clarify the incompressible limit, the compressible energy equation (2.21) is written in

terms of pressure and kinetic energy. For this purpose, the non-dimensional stiffened gas equation of state is used that relates pressure and internal energy to each other

$$p = (\gamma - 1)(e - M^2 \underbrace{\frac{\rho}{2}\left|\vec{v}^2\right|}_{e_{kin}}) - \gamma p_\infty . \tag{2.24}$$

Replacing the total energy in equation (2.21) with the help of the above equation of state and introducing the pressure decomposition of equation (2.23) into the Euler equations, they may be written as

$$\frac{\partial \rho}{\partial t} + \nabla \cdot (\rho \vec{v}) = 0 \,, \tag{2.25}$$

$$\frac{\partial (\rho \vec{v})}{\partial t} + \nabla \cdot [(\rho \vec{v}) \circ \vec{v}] + \nabla p^{(2)} = 0 \,, \tag{2.26}$$

$$\begin{aligned} \frac{\partial}{\partial t}\left(p^{(0)} + M^2 p^{(2)} + (\gamma - 1) M^2 e_{kin}\right) + \\ \nabla \cdot \left[\vec{v}\left((\gamma - 1) M^2 e_{kin} + \gamma (p^{(0)} + M^2 p^{(2)} + p_\infty)\right)\right] = 0 \,. \end{aligned} \tag{2.27}$$

This is a pure reformulation of the Euler equations (2.1)-(2.3) with the pressure decomposition of equation (2.23) under the assumption of a given background pressure $p^{(0)}(t)$. The incompressible limit equations are now easily obtained by letting M tend to zero ($M \to 0$):

$$\frac{\partial \rho}{\partial t} + \nabla \cdot (\rho \vec{v}) = 0 \,, \tag{2.28}$$

$$\frac{\partial (\rho \vec{v})}{\partial t} + \nabla \cdot [(\rho \vec{v}) \circ \vec{v}] + \nabla p^{(2)} = 0 \,, \tag{2.29}$$

$$\frac{\partial}{\partial t}\left(p^{(0)}\right) + \nabla \cdot \left(\gamma (p^{(0)} + p_\infty) \vec{v}\right) = 0 \,. \tag{2.30}$$

These zero Mach number limit equations include the possibility for changes of the background pressure and density in time due to a compression from the boundary. Both quantities are always constant in space. If no compression from the boundary occurs, then the thermodynamic pressure becomes constant in space and time and equation (2.30) is equal to the divergence-free constraint of equation (2.13). Moreover, the system of equations (2.28)-(2.30) is then equivalent to the incompressible Euler equations (2.9)-(2.13).
The asymptotic considerations of Klainerman *et al.* [6] concerning the transition from the compressible to the incompressible flow regime have been derived for isentropic flows. They have been extended to non-isentropic flows by Klein [7]

in order to take into account variable densities and a temporal variation of the background pressure in the zero Mach number limit. On the basis of these considerations, Munz *et al.* derived the multiple pressure variables approach (MPV) in primitive [10] and conservative [11] formulation. Basically, the MPV method builds on the pressure decomposition of equation (2.23) that is now discussed in more detail.

2.3.1.1. The background pressure $p^{(0)}$

Following [11], a few remarks can be made on the background pressure $p^{(0)}$. First of all, it is spatially constant but allowed to change over time. In the incompressible limit, it is the background pressure $p^{(0)}$ that formally satisfies an equation of state such that the singular incompressible limit of the compressible flow equations can be avoided. The background pressure $p^{(0)}$ can be defined as the spatially averaged pressure in the computational domain Ω

$$p^{(0)}(t) = \frac{1}{|\Omega|} \int_{\Omega} p d\Omega. \tag{2.31}$$

The temporal evolution of the background pressure $p^{(0)}$ is described by the energy equation (2.27). For this purpose it has to be reformulated into a pressure equation using the mass equation (2.25) and the momentum equation (2.26)

$$\frac{\partial p^{(0)}}{\partial t} + \gamma(p^{(0)} + p_{\infty})\nabla \cdot \vec{v} = 0. \tag{2.32}$$

The background pressure $p^{(0)}$ is constant in space but is allowed to vary over time such that the above equation can be rewritten as

$$\frac{dp^{(0)}}{dt} = -\gamma(p^{(0)} + p_{\infty})\nabla \cdot \vec{v}. \tag{2.33}$$

As a next step the Gauss theorem is applied to the divergence operator

$$\nabla \cdot \vec{v} = \int_{\partial\Omega} (\vec{v} \cdot \vec{n}) dA, \tag{2.34}$$

where $\vec{n}$ is the unit normal vector that is directed outward on the boundary $\partial\Omega$. This integral describes the effects of a global compression of the domain Ω. If the domain boundaries are in a relative motion to each other, the background pressure changes due to a compression from the boundaries.

Finally, the equation for the temporal evolution of $p^{(0)}$ is obtained by averaging equation (2.33) in space over the domain Ω and by replacing the velocity divergence by the Gauss theorem following equation (2.34)

$$\frac{dp^{(0)}}{dt} = -\frac{\gamma(p^{(0)} + p_\infty)}{|\Omega|} \int_{\partial\Omega} (\vec{v} \cdot \vec{n}) dA. \tag{2.35}$$

The equations (2.33) and (2.35) allow the formulation of a divergence constraint for the velocity $\vec{v}$

$$\nabla \cdot \vec{v} = \frac{1}{|\Omega|} \int_{\partial\Omega} (\vec{v} \cdot \vec{n}) dA. \tag{2.36}$$

It is evident that the divergence of the velocity directly depends on a surface integral over the domain boundaries and therefore on the effects of outer compression due to a relative motion of the domain boundaries. In the absence of any outer compression, the surface integral vanishes and the incompressible, divergence-free constraint for the velocity is recovered

$$\nabla \cdot \vec{v} = 0. \tag{2.37}$$

In the context of such a classical incompressible flow, $p^{(0)}$ is not only constant in space but also in time according to equation (2.35).

2.3.1.2. The hydrodynamic pressure $p^{(2)}$

In the asymptotic context, the hydrodynamic pressure $p^{(2)}$ helps to avoid the singular limit of the momentum equation (2.20). Moreover, it has to guarantee the zero divergence constraint for the velocity in the case of incompressible flows.
The hydrodynamic pressure $p^{(2)}$ is the primary variable of the numerical scheme resulting in the solution of a Poisson equation for $p^{(2)}$. For compressible flows, the sum of $p^{(0)}$ and $p^{(2)}$ has to satisfy an equation of state.

2.4. One-dimensional solution of the Euler equations in the zero Mach number limit

In the following, the focus is on the one-dimensional Euler equations for which analytical solutions for a perfect gas and a Tait fluid can be derived in the spatial domain $\Omega = [a, b]$ in the zero Mach number limit. The one-dimensional scalar velocity is simply denoted v subsequently. A local coordinate x is introduced whose origin is located at the left boundary of Ω. Moreover, according to

the asymptotic expansion (2.22) the density is decomposed into a background density $\rho^{(0)}$ and a density $\rho^{(2)}$ that includes density changes due to hydrodynamic effects

$$\rho(\vec{x},t) = \rho^{(0)}(t) + M^2\rho^{(2)}(\vec{x},t). \tag{2.38}$$

Together with the pressure decomposition of equation (2.23) the asymptotic expansion of the density is inserted into the Euler equations for the subsequent investigations. The leading order pressure and density terms $p^{(0)}$ and $\rho^{(0)}$ satisfy the equation of state in the limit case $M = 0$. This zero Mach number regime is considered in more detail in one space dimension in the following.

2.4.1. Perfect gas

The zero Mach number Euler equations (2.28)-(2.30) are reduced to one space dimension for the perfect gas, setting $p_\infty = 0$. The density $\rho^{(0)}$ is assumed to be constant in space, but may vary in time according to a compression from the boundaries like it is the case for the pressure $p^{(0)}$. Under these assumptions, the equations (2.28)-(2.30) can finally be written as

$$\rho_t^{(0)} = -\rho^{(0)}v_x, \tag{2.39}$$

$$v_t + vv_x = -\frac{1}{\rho^{(0)}}p_x^{(2)}, \tag{2.40}$$

$$v_x = -\frac{1}{\gamma p^{(0)}}\frac{dp^{(0)}}{dt}, \tag{2.41}$$

where the subscripts x and t designate the corresponding partial spatial and temporal derivatives. Equation (2.41) shows that the original energy equation drastically simplifies in the one-dimensional $M \to 0$ case and reduces to an evolution equation for the background pressure $p^{(0)}$.
Starting from the equations above, the analytical solution can be determined in the domain Ω. From equation (2.41), the time dependent solution of the background pressure $p^{(0)}$ for a perfect gas in the limit case $M \to 0$ is obtained as

$$p^{(0)}(t) = p^{(0)}(t=0) \cdot e^{-\gamma \int_0^t \frac{v_b(\tau)-v_a(\tau)}{|\Omega|}d\tau}, \tag{2.42}$$

where v_a and v_b designate the velocities at the left and the right boundary of the $M = 0$ region $\Omega = [a,b]$. Furthermore, as the pressure $p^{(0)}$ only depends on time it is evident from equation (2.41) that the velocity gradient is always spatially constant and therefore the velocity field has to be linear in space

$$v(x,t) = v_a(t) + \frac{x}{|\Omega|}(v_b(t) - v_a(t)). \tag{2.43}$$

The relation for the background density $\rho^{(0)}$ results from equation (2.39) as

$$\rho^{(0)}(t) = \rho^{(0)}(t=0) \cdot e^{-\int_0^t \frac{v_b(\tau)-v_a(\tau)}{|\Omega|} d\tau}. \tag{2.44}$$

In a last step, the momentum equation (2.40) can be reformulated to calculate the hydrodynamic pressure $p^{(2)}$

$$p_x^{(2)} = -\rho^{(0)}(v_t + v \cdot v_x). \tag{2.45}$$

Insertion of equation (2.43) and a final integration with respect to x finally lead to

$$\begin{aligned} p^{(2)}(x,t) = \quad & -\rho^{(0)}(t) \left((v_a)_t + v_a \tfrac{v_b - v_a}{|\Omega|} \right) x - \\ & \tfrac{\rho^{(0)}(t)}{2|\Omega|} \left((v_b)_t - (v_a)_t + \tfrac{(v_b - v_a)^2}{|\Omega|} \right) x^2. \end{aligned} \tag{2.46}$$

The pressure $p^{(2)}$ is determined by equation (2.46) up to an integration constant. This constant depends on the pressure boundary conditions. In a general case without pressure boundary conditions, any constant pressure can be added to $p^{(2)}$ and in equation (2.46) the integration constant is simply chosen to be zero.
In the end, the solutions for the spatially constant background pressure $p^{(0)}(t)$ and density $\rho^{(0)}(t)$ are obtained, as well as the relation for the temporal and spatially variable hydrodynamic pressure $p^{(2)}(x,t)$. In all the cases, the knowledge of the velocity at the domain boundaries is a prerequisite to evaluate the relations for density and pressure, whereas the solution of $p^{(2)}(x,t)$ also depends on the temporal derivative of the velocity.

2.4.2. Tait fluid

Similar to the above derivations for the perfect gas, the zero Mach number Euler equations can also be solved analytically using the Tait equation of state (2.6). For this purpose, the non-dimensional stiffened gas equation of state (2.24) with $p_\infty = (k_0 - p_0)$ is used.
The change of the equation of state only affects the energy equation. Finally, the one-dimensional version of the equations (2.28)-(2.30) is written as follows

for the Tait equation of state

$$\rho_t^{(0)} = -\rho^{(0)} v_x, \tag{2.47}$$

$$v_t + v v_x = -\frac{1}{\rho} p_x^{(2)}, \tag{2.48}$$

$$v_x = -\frac{1}{\gamma(p^{(0)} + k_0 - p_0)} \frac{dp^{(0)}}{dt}. \tag{2.49}$$

The exact solution for the pressure $p^{(0)}$ is obtained in an analogous way to the perfect gas case

$$p^{(0)}(t) = p_0 - k_0 + (p^{(0)}(t=0) - p_0 + k_0) \cdot e^{-\gamma \int_0^t \frac{v_b(\tau) - v_a(\tau)}{|\Omega|} d\tau}. \tag{2.50}$$

Since the change in the equation of state only influences the energy equation, it is just the relation for the pressure $p^{(0)}$ that has to be adapted, while the solutions for the density $\rho^{(0)}$ (cf. equation (2.44)) and the hydrodynamic pressure $p^{(2)}$ (cf. equation (2.46)) stay unchanged.

2.5. The incompressible Navier-Stokes equations for two-phase flows

The incompressible Navier-Stokes equations for two-phase flows are given by the continuity equation and the momentum equation

$$\nabla \cdot \vec{v} = 0, \tag{2.51}$$

$$\frac{\partial(\rho\vec{v})}{\partial t} + \nabla \cdot (\rho\vec{v}) \circ \vec{v} = -\nabla p + \rho\vec{k} + \nabla \cdot \mu[\nabla\vec{v} + (\nabla\vec{v})^T] + \vec{f}_\gamma \delta_S. \tag{2.52}$$

Here μ is the dynamic viscosity, $\rho\vec{k}$ takes into account body forces, the term $\vec{f}_\gamma$ is a body force that represents the influence of surface tension in the vicinity of the interface and δ_S is a delta function concentrated on the surface. Apart from the volume force $\vec{f}_\gamma$ for the surface tension, the momentum equation (2.52) resembles that of a single-phase flow. This is the so-called one-fluid formulation for incompressible two-phase flows where the coupling of the two fluids is provided by variable material properties ρ and μ and the surface tension term $\vec{f}_\gamma$ that acts at the interface location [38].

2.6. Surface tension

At an interface separating two immiscible fluids a pressure jump

$$p_2 - p_1 \equiv \Delta p = \sigma\kappa, \tag{2.53}$$

appears according to the Young-Laplace equation [39]. Here σ is the surface tension coefficient and κ represents the curvature that is defined as

$$\kappa = -\nabla \cdot \vec{n}, \tag{2.54}$$

with $\vec{n}$ being the surface normal pointing from the fluid to the gas phase. Hence, surface tension is directly proportional to the curvature κ in the present case, as σ is taken to be constant. Several numerical models have been developed in order to include surface tension into the incompressible Navier-Stokes equations.
As is obvious from equation (2.52), for incompressible flows surface tension is accounted for as a volume force in the momentum equation. Due to the delta function δ_S the corresponding force $\vec{f_\gamma}$ on the right-hand side of the equation is only present at the interface while it vanishes in grid cells away from the interface.

2.7. Interface tracking methods

For the DNS of two-phase flows, the interface location and resolution is of crucial interest. Therefore, an additional transport equation is introduced to describe the movement of the material interface between the two fluids. There are several well-established interface tracking schemes that have already been introduced briefly in section 1.3. In the following the VOF and the level set method are presented, that are both used in this work.
The VOF method has originally been designed for incompressible flows as the density field is reconstructed from the volume fractions at each time step. For a VOF extension to compressible flows, especially in cells containing gas and liquid, the determination of density and internal energy of the two fluids has to be done applying special methods [34,40]. The level set method can directly be applied to compressible as well as incompressible flows.

2.7.1. The volume of fluid (VOF) method

The volume of fluid method was developed by Hirt and Nichols [15]. It is based on a conservation equation for the volume of the liquid phase and therefore it is

suited to incompressible flow simulations. For the representation of the phases, an additional variable f is introduced which represents the volume fraction of the liquid phase

$$f = \begin{cases} 0 & \text{in the gaseous phase,} \\ 0 < f < 1 & \text{in cells containing a part of the interface,} \\ 1 & \text{in the liquid phase.} \end{cases} \tag{2.55}$$

A two-dimensional example is given by Fig. 2.1.

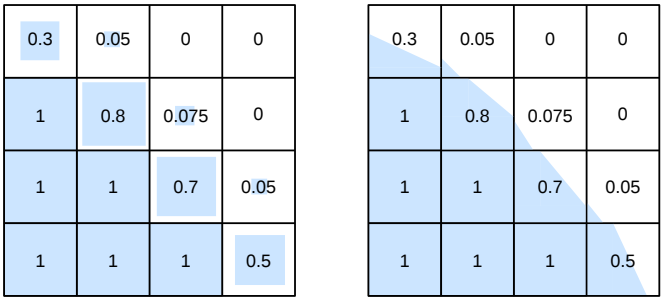

(a) Discrete distribution of the liquid volume fraction f; interface location unknown.

(b) Interface is linearly reconstructed following the PLIC approach.

Figure 2.1.: Representation of the fluid phases by the volume fraction variable f of the VOF method.

The movement of the interface is tracked via the transport of the volume fraction f by the following transport equation

$$\frac{\partial f}{\partial t} + \vec{v} \cdot \nabla f = 0. \tag{2.56}$$

For incompressible flows, the equation can be reformulated in a conservative way because of the divergence constraint for velocity $\nabla \cdot \vec{v} = 0$

$$\frac{\partial f}{\partial t} + \nabla \cdot (f\vec{v}) = 0. \tag{2.57}$$

The volume fraction itself only contains the information about the cell average of the liquid volume, as is obvious from Fig. 2.1(a) and the location of the interface is unknown. Simple advection of the volume fraction f leads to a smearing of f and therefore of the interface that yet has to be kept sharply resolved. Thus, at every time step, the interface is linearly reconstructed on the basis of a piecewise linear interface calculation (PLIC) algorithm [41]. This geometrical reconstruction is illustrated for the two-dimensional case in Fig. 2.1(b). Based on the reconstruction, the liquid and gaseous fluxes across the cell faces are determined and the interface is prevented from being smeared across several grid cells during the advection.
In the context of the investigations linked to unphysical parasitic currents, the VOF method is looked at in more detail in section 4.3, especially with respect to the computation of surface curvature on the basis of the VOF volume fractions.

2.7.2. The level set method

Based on Osher *et al.* [16], a level set variable Φ is initialized as a signed distance function with respect to the interface. Hence, its zero level set determines the interface position. The level set distribution for a spherical droplet with radius $R = 0.25$ is illustrated in Fig. 2.2 on a plane through its center. The initialization as a distance function is obvious, the levels inside the droplet have a negative sign while they are positive outside.
In order to track the interface movement, the following transport equation in primitive variables can be used

$$\frac{\partial \Phi}{\partial t} + \vec{v} \cdot \nabla \Phi = 0. \tag{2.58}$$

The level set function is advected by the fluid velocity $\vec{v}$. In the given case, interface and fluid velocity are equal to each other as phase transition is not taken into account.
If equation (2.58) is used in the context of a numerical scheme designed for the solution of conservation laws, it might be more convenient to treat the level set function in a conservative manner to easily implement it into the solver. For this purpose, equation (2.58) is modified in the following way

$$\frac{\partial \Phi}{\partial t} + \nabla \cdot (\vec{v}\Phi) = \Phi \nabla \cdot \vec{v}. \tag{2.59}$$

However, it is obvious that in contrast to the VOF transport equation (2.57) for incompressible flows, a new term appears on the right-hand side of the equation.

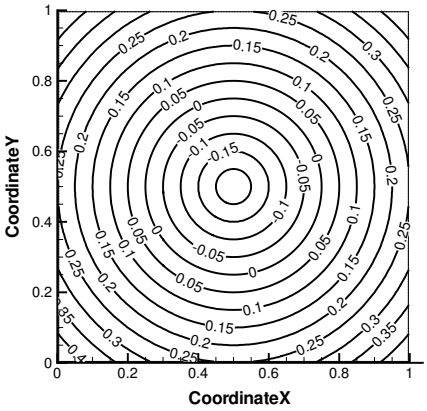

Figure 2.2.: Level set function Φ for a spherical droplet of radius $R = 0.25$ (cut through the droplet center).

As the velocity field has a divergence that is different from zero in the case of compressible flows, this new term has to be taken care of. For incompressible flows with $\nabla \cdot \vec{v} = 0$, equation (2.59) is automatically in conservative formulation as the term on the right-hand side vanishes.

3. Coupling of compressible and incompressible flow regions

In the following chapter the development of different iterative methods for the coupling of compressible and incompressible (zero Mach number) flow regions in one space dimension is presented. The description follows the investigations in [42] and the one-dimensional scalar velocity is denoted v in this chapter.

The numerical simulation of multiphase flows that include liquid droplets and gas is often based on the incompressible Navier-Stokes equations assuming both fluids to be incompressible. But, there are several applications for which the treatment as overall incompressible flow becomes inaccurate, such as the injection and combustion of fuel droplets or shock induced mixing of liquids, where density changes cannot be neglected at least in the gas phase.

One approach to overcome this problem is to treat gas and liquid both as compressible fluids. In this fully compressible treatment, the liquid is also modeled by the compressible flow equations with an appropriate equation of state. As already discussed in section 1, this coupling bears some difficulty, because the change of the equation of state at the interface often generates pressure and velocity oscillations if no special interface treatment is applied [43]. To prevent such unphysical oscillations, there exist different numerical schemes that can be classified into diffuse and sharp interface methods (cf. section 1.3). Considering both fluids as compressible, thermodynamics and fluid flow are strongly coupled. Additionally, the compressible treatment of the liquid phase introduces large scale differences in the speed of sound that is very high in the weakly compressible fluid in comparison to the gas phase. This represents a severe restriction for the computational time step within an explicit time approximation or leads to a bad condition number in an implicit time approximation and finally results in a dramatical increase of computation time.

There is an alternative to the fully compressible treatment of both phases. In the case of a sharp interface coupling of compressible and incompressible domains, both regions can be numerically modeled by appropriate approaches. But, this is also not too simple because the governing equations are different.

Such an incompressible-compressible coupling was already proposed by Caiden *et al.* [44]. They used a sharp interface tracking within a ghost fluid approach for the coupling. Their coupling conditions are based on the requirement that velocity as well as pressure are continuous across the material interface. The pressure on the compressible side is coupled with the hydrodynamic pressure from the incompressible region.
In the following, a compressible-incompressible coupling is realized on the basis of the asymptotic pressure decomposition of equation (2.23) introduced for the zero Mach number limit. The investigations are focused on a detailed study in one space dimension and give insight into the basic coupling of the two flow regions without surface tension and dissipative effects.
At first, jump conditions for velocity and pressure across the compressible-incompressible interface are described. On the basis of these conditions, iterative coupling schemes are presented that connect the solution of a half-Riemann problem on the compressible side to the analytical solution of the zero Mach number Euler equations on the incompressible side. The coupling algorithms are designed to provide the numerical fluxes to the adjacent compressible flow solver at the compressible-incompressible interface and therefore they act as boundary condition.

3.1. Jump conditions at a compressible-incompressible interface

Across an interface between compressible and incompressible flows, the following jump conditions are supposed to hold true in the one-dimensional case without surface tension, viscosity and mass transfer

$$[v] = 0, \tag{3.1}$$

$$[p] = 0, \tag{3.2}$$

where the brackets $[\cdot]$ indicate the jump in the enclosed quantity. This is consistent with the demand for continuity of velocity and pressure across the interface. The density stays uncoupled and can therefore be discontinuous.

3.2. Two generic examples

In the following, two generic test cases are presented to motivate and assess the coupling procedures. The first case is dominated by the effects of hydrodynamics as the liquid region is accelerated due to a pressure gradient at the

domain boundaries. The second example describes the pure, symmetric compression of a liquid region and because of the symmetry only half of the domain is considered.

3.2.1. Hydrodynamic test problem

The focus of the first test is on the hydrodynamic behavior of the incompressible region and follows the test case configuration of [44]. It describes the hydrodynamic acceleration of a zero Mach number region by a pressure gradient. For this purpose, the test setting of Fig. 3.1 is used that shows the setup in the space-time domain. The pressures, velocities and densities in the different flow regions are given and denoted by the subscripts l and r for the left and right compressible flow region. In the vicinity of the interface, the flow variables in the compressible domain are additionally marked by the superscript $*$.

The incompressible domain is connected to two compressible flow regions, where there is an initial pressure gradient imposed on the incompressible region. As $p_l \neq p_r$, the incompressible domain is set in motion and the coupling of the momentum across the interface cannot be neglected. The $*$ values in the vicinity of the interface are obtained as solution of a half-Riemann problem. The test case is used to assess two different coupling algorithms. First, the compressible interface pressure p^* is coupled to the hydrodynamic pressure $p^{(2)}$ of the $M = 0$ region, while the thermodynamic pressure $p^{(0)}$ is neglected. Then, a second coupling scheme is presented that couples the pressure of the compressible region to the hydrodynamic pressure $p^{(2)}$ and the thermodynamic background pressure $p^{(0)}$ of the zero Mach number region.

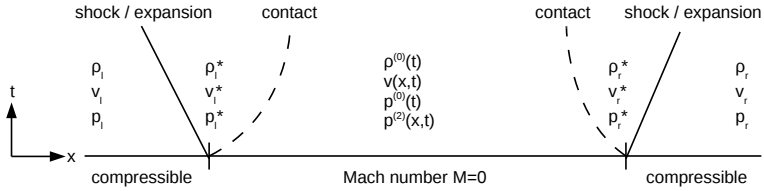

Figure 3.1.: Test case setup for the hydrodynamic acceleration of an incompressible domain.

3.2.2. Pure compression test problem

The second example is a pure compression of a liquid region by a pressure wave from the compressible region. This example may be thought of as the compression of a radially symmetric droplet which is compressed by a higher pressure from outside. The transfer of momentum is neglected and the focus is solely on the compression of the droplet. Therefore, an acoustic wave is generated that travels through the compressible region and finally impinges on the interface between the compressible and the $M = 0$ region and causes a compression of the zero Mach number region. To simplify this problem, the planar case is considered as it is depicted in Fig. 3.2 in the space-time domain. In contrast to the above test case, this case is not accessible by the approach of Caiden *et al.* [44], as they do not take into account any compressibility effects.

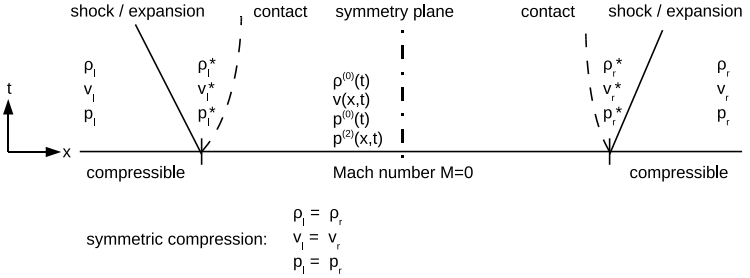

Figure 3.2.: Compression of a radially symmetric droplet.

It is obvious from Fig. 3.2 that the problem is symmetric as $p_l = p_r$, $\rho_l = \rho_r$, $v_l = v_r$ and therefore, only the left half of the domain is considered prescribing a symmetry boundary condition at the center of the $M = 0$ domain as it is displayed in Fig. 3.3. To simulate this test case, an algorithm is presented that couples the compressible interface pressure p^* to the thermodynamic pressure $p^{(0)}$ of the zero Mach number domain. For this coupling, the hydrodynamic pressure $p^{(2)}$ is neglected and its effects are not taken into account.

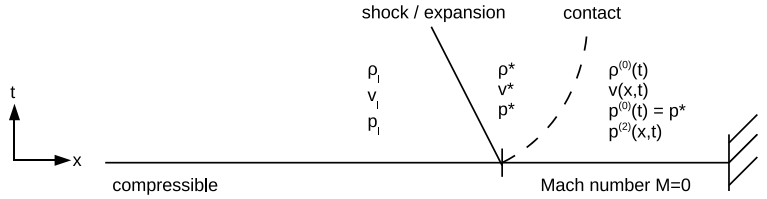

Figure 3.3.: Test case setup for the compression of a radially symmetric droplet. Only the left half of the original setting is considered using a symmetry boundary condition.

3.3. Iterative coupling procedures

In the following, three different algorithms are presented for the coupling of a compressible flow with a zero Mach number flow in one space dimension. While the compressible flow region is discretized and solved by a numerical scheme, the zero Mach number region is treated analytically on the basis of the equations derived in section 2.4. The link between the two different flow domains is established by the jump conditions of section 3.1 that require the equality of pressure and velocity across the interface. In general, the interface represents a boundary of the compressible flow region and the coupling algorithm delivers the quantities needed for the evaluation of the compressible flux at the interface location, given in one space dimension by

$$f = \begin{pmatrix} \rho v \\ \rho v^2 + p \\ v(e+p) \end{pmatrix}. \tag{3.3}$$

This means that the coupling approaches act like boundary conditions that prescribe the compressible flux terms. The flux calculation is based on the evaluation of a half-Riemann problem on the compressible side of the interface and the analytical equations of the zero Mach number region on the other side of the interface. The process is controlled by the jump conditions given by the equations (3.1)-(3.2). The scheme iterates until the equality of pressure and velocity across the interface is reached.
A schematic of the half-Riemann problem and the two flow regions is given in Fig. 3.4. It can be seen that the compressible state, marked by the subscript

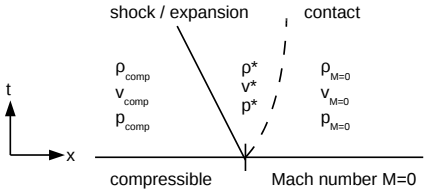

Figure 3.4.: Half-Riemann problem at the interface between the compressible and the zero Mach number flow region.

comp is connected to the zero Mach number flow, indicated by the subscript $M = 0$, by the solution of the half-Riemann problem. The evaluation of the shock or expansion relations on the basis of the compressible flow variables gives the compressible star state next to the contact discontinuity. According to the jump conditions, the equality of velocity and pressure has to be guaranteed

$$v^* = v_{M=0}, \tag{3.4}$$

$$p^* = p_{M=0}, \tag{3.5}$$

and this is done by iterating over pressure and velocity solving the half-Riemann problem and the exact relations for the $M = 0$ region, until the termination criterion is satisfied.

The difficulty in the coupling arises due to the fact that the pressure has different meanings in the Mach number zero and the compressible region. While in the compressible region the pressure is coupled with all other variables by the equation of state, the pressure in the Mach number zero equations splits into two parts, the spatially constant thermodynamic background pressure $p^{(0)}$ and the hydrodynamic one $p^{(2)}$. Moreover, in the zero Mach number limit, the connection between the two pressures $p^{(0)}$ and $p^{(2)}$ is lost as they are completely decoupled from each other. For this reason, the coupling of a compressible to a zero Mach number region requires assumptions with respect to the pressure coupling.

Three different schemes have been developed that differ in the way the hydrodynamic and thermodynamic pressure of the zero Mach number region are coupled to the compressible pressure. For this purpose, different assumptions are necessary for the zero Mach number pressure term $p_{M=0}$ that is coupled to the compressible pressure p^* at the interface:

- The first scheme is a purely hydrodynamic coupling and the compressible pressure p^* is supposed to be equal to the hydrodynamic pressure $p^{(2)}$, while the thermodynamic pressure $p^{(0)}$ is neglected

$$p^* = p^{(2)}. \tag{3.6}$$

- The second algorithm represents a purely thermodynamic coupling approach, where the compressible pressure p^* is coupled to the thermodynamic pressure $p^{(0)}$ of the zero Mach number region, while the hydrodynamic pressure $p^{(2)}$ is neglected

$$p^* = p^{(0)}. \tag{3.7}$$

- In a third approach, a combination of thermodynamic and hydrodynamic effects is considered for the zero Mach number region. Here, the compressible pressure p^* is coupled to both, the hydrodynamic pressure $p^{(2)}$ and a spatially constant background pressure $p^{(0)}$. As stated by the incompressible equations, the hydrodynamic pressure $p^{(2)}$ is just determined up to a constant as only its gradient is used in the momentum equation (2.29). The pressure $p^{(2)'}$ is introduced in the zero Mach number region, which is continuous to the compressible pressure at the interface. This pressure is then split into the hydrodynamic and thermodynamic part according to

$$p^{(2)} := p^{(2)'} - \frac{1}{|\Omega|}\int_\Omega p^{(2)'} d\Omega = p^{(2)'} - p^{(0)}. \tag{3.8}$$

  Hence, the mean value of $p^{(2)'}$ is accumulated in the thermodynamic background pressure $p^{(0)}$, which may vary in time by a global compression of the zero Mach number domain and which is defined in equation (2.31) as the mean pressure.

All algorithms are designed to provide the compressible fluxes at the domain boundaries of the compressible flow region needed to update the flow solution during one computational time step. In the following, the three algorithms are presented in detail.

3.3.1. Coupling procedure based on the hydrodynamic pressure

This algorithm couples the pressure p^* of the compressible region with the hydrodynamic pressure $p^{(2)}$ of the zero Mach number region

$$p^* = p^{(2)}, \tag{3.9}$$

where the thermodynamic pressure $p^{(0)}$ is neglected. Moreover, a compression of the domain from the boundaries (cf. equation (2.36)) is not allowed, such that the velocity has to be divergence-free $v_x = 0$. In one space dimension, this is equivalent to a spatially constant velocity. For this case the zero Mach number limit does not allow any compressible effects and coincides with the fully incompressible equations. The algorithm is suited to treat the hydrodynamic acceleration of an incompressible flow domain driven by a pressure gradient as it is described in section 3.2.1. At the compressible-incompressible interface, the coupling algorithm gives the compressible flux based on an iterative procedure that combines the solution of a half-Riemann problem on the compressible side and the exact solution of the incompressible domain. The iteration is controlled by the jump conditions (3.1)-(3.2) and it is stopped once the velocity satisfies the corresponding termination criterion.

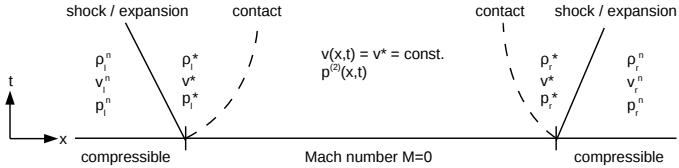

Figure 3.5.: Half-Riemann problems for the hydrodynamic coupling. The hydrodynamic pressure $p^{(2)}$ is coupled to the compressible pressure.

Subsequently, the iterative procedure for the update of the flow variables from time t^n to t^{n+1} is described. The iteration is started by imposing a left pressure p_l^n and a right pressure p_r^n to the incompressible region (cf. Fig. 3.5). Based on this pressure gradient, a guess for the interface velocity v^* is determined. Afterwards, the solution of two half-Riemann problems gives the interface pressure $p_{l,r}^*$. The flow-chart for this iterative coupling procedure is illustrated in Fig. 3.6. In more detail, the coupling can be described as follows:

- At the beginning of the iterative procedure, a first order explicit predictor is applied to the momentum equation (2.40) in order to get a predictor of the interface velocity v^* at the new time level t^{n+1}. As a divergence-free velocity distribution is supposed, the momentum equation can be rewritten as

$$v^* = v^n - \Delta t \left(\frac{p_x^{(2)n}}{\rho^{(0)n}} \right), \tag{3.10}$$

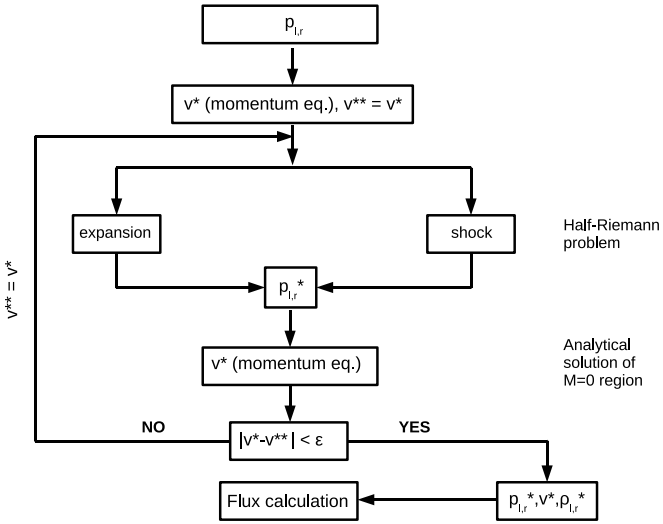

Figure 3.6.: Hydrodynamic coupling scheme: hydrodynamic pressure $p^{(2)}$ is coupled to the compressible pressure.

where Δt stands for the discrete time step. Due to the divergence-free constraint, the velocity v is spatially constant inside the incompressible, one-dimensional domain as it is also the case for the density $\rho^{(0)}$. Moreover, with $v_x = 0$ it is directly evident from the momentum equation (2.40) that the hydrodynamic pressure $p^{(2)}$ has a linear distribution inside the incompressible domain. Hence, the pressure gradient $p_x^{(2)n}$ is constant and is evaluated at the beginning of the iteration using the pressure in the adjacent compressible domains

$$p_x^{(2)n} = \frac{p_r^n - p_l^n}{|\Omega|}, \tag{3.11}$$

where p_r^n and p_l^n designate the compressible pressure at the left and the right boundary of the incompressible domain Ω, respectively (cf. Fig. 3.5). To control the iteration process, it is necessary to store the velocity v^* additionally as v^{**}.

- On the basis of the velocity predictor the inner loop of the iteration starts as follows:
  - Taking the predictor of the velocity v^* from equation (3.10) as an input, a half-Riemann problem is evaluated to determine the compressible state close to the domain boundaries. This is illustrated in Fig. 3.5 and to start the evaluation of the half-Riemann problem, the arithmetic mean value of the incompressible pressure $p^{(2)}$ and the pressures $p^n_{l,r}$ in the compressible region is computed, such that it can be determined whether the shock or expansion relations have to be applied to solve the half-Riemann problem in the compressible domain. The evaluation of the corresponding equation leads to the compressible pressure $p^*_{l,r}$ at the left and right boundary.
  - The new pressure $p^*_{l,r}$ can now be inserted directly into the pressure gradient of the momentum equation (3.10)

$$v^* = v^n - \frac{\Delta t}{\rho^{(0)n}} \left(\frac{p^*_r - p^*_l}{|\Omega|} \right). \tag{3.12}$$

    This leads to a better velocity estimation for v^*.
  - At each iteration, the new velocity estimate v^* is compared to the old velocity v^{**}. If the change in velocity falls below a certain threshold ϵ, the iteration is stopped. Otherwise, the newly computed velocity v^* is stored as v^{**} and the iteration is repeated by evaluating the shock or expansion relations using the new velocity predictor for v^*.
- At the end of the iteration, the compressible fluxes are evaluated. Having already determined the pressure $p^*_{l,r}$ and the velocity v^*, the only missing part is the density $\rho^*_{l,r}$. Once the corresponding relations are evaluated, the fluxes for the compressible region can directly be calculated on the basis of the star values.

While the hydrodynamic test problem in Fig. 3.1 can be solved in a straightforward way and the pressure difference between the two compressible regions drives the iteration procedure, the pure compression problem cannot be handled by the present approach. Here, the pressure gradient introduces a velocity boundary condition at the interface which is inconsistent with the incompressible equations where the velocity has to be divergence-free and therefore spatially constant in one space dimension. Such a pure compression can only be treated by taking into account the thermodynamic pressure in the incompressible flow region, which is described next.

3.3.2. Coupling procedure based on the thermodynamic background pressure

This algorithm establishes a coupling of the pressure of the compressible region p^* with the thermodynamic pressure $p^{(0)}$ of the zero Mach number region

$$p^* = p^{(0)}, \tag{3.13}$$

and the hydrodynamic pressure $p^{(2)}$ is neglected. Such a thermodynamic coupling allows to take into account compressible effects in the zero Mach number limit as they are described for the test setting of section 3.2.2. Assuming the compressible pressure to coincide with the thermodynamic background pressure $p^{(0)}$ of the zero Mach number region, the velocity divergence is allowed to be different from zero in the $M = 0$ flow domain. As is obvious from the equations (2.41) and (2.49), the velocity has a linear distribution if a compression from the boundaries and therefore a temporal change of the background pressure $p^{(0)}$ is allowed. From a physical point of view, the test setup of section 3.2.2 corresponds to the radially symmetric compression of a zero Mach number region. For this reason, a symmetry plane is introduced in the test setting. This is evident from Fig. 3.3, where the right boundary is displayed as a solid wall that is equivalent to a symmetry plane at the center of the zero Mach number domain (cf. Fig. 3.2 and Fig. 3.3), as the velocity has to be equal to zero there.

Again, the coupling algorithm returns the flux terms for the compressible flow solver and the iterative procedure is based on the exact relations for the zero Mach number region and the evaluation of a half-Riemann problem on the compressible side of the interface. The iterative procedure is controlled by the jump conditions for velocity and pressure given by the equations (3.1)-(3.2) and the iterations are stopped, once the termination criterion for the pressure has been satisfied.

In the following, the coupling algorithm for the computation of the compressible fluxes needed to update the flow variables from time t^n to t^{n+1} is described in detail and the setting is displayed in Fig. 3.7. The procedure starts with the evaluation of a half-Riemann problem in the compressible flow region that gives an interface velocity v^*. On the basis of this velocity, the new background pressure $p^{(0)}$ of the zero Mach number region is determined and, according to the coupling conditions, used as new interface pressure p^* for an evaluation of the half-Riemann problem resulting in a new interface velocity.

The procedure is illustrated in Fig. 3.8 and described in the following:

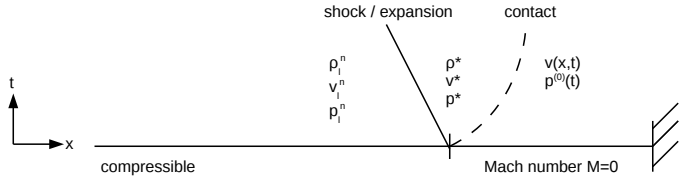

Figure 3.7.: Half-Riemann problem for the thermodynamic coupling. The thermodynamic pressure $p^{(0)}$ is coupled to the compressible pressure.

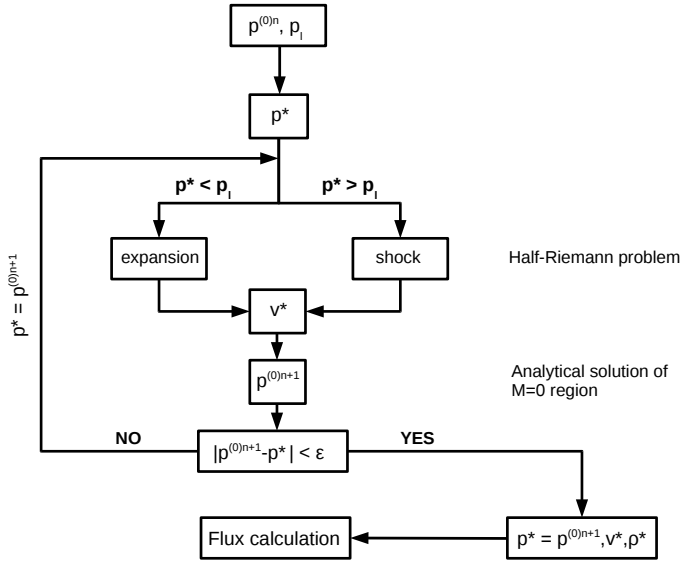

Figure 3.8.: Thermodynamic coupling scheme: background pressure $p^{(0)}$ is coupled to the compressible pressure.

- Start the iteration by a first pressure guess for p^*. A quite simple choice is to use the arithmetic mean value of the left pressure p_l^n and the incom-

pressible pressure $p^{(0)n}$ at the beginning of the time step (cf. Fig. 3.7).

- On the basis of the guessed interface pressure p^* the inner iteration is started:
  - A half-Riemann problem is evaluated to get the interface velocity v^*. Comparing p^* to the pressure p_l^n gives the information if both states are linked by an expansion ($p^* < p_l^n$) or a shock ($p^* > p_l^n$). This provides the relation for the computation of the velocity v^* at the interface.
  - The interface velocity v^* is used as input for the analytical solution of the incompressible pressure $p^{(0)}$ (cf. equation (2.42)). The obtained pressure $p^{(0)n+1}$ is compared to the pressure p^* from the previous iteration. In the end, $p^{(0)n+1}$ and p^* have to be equal. If the difference is smaller than a selected threshold ϵ, the iteration is stopped. Otherwise the determined pressure $p^{(0)n+1}$ is stored as p^* and the inner iteration is repeated with the evaluation of the half-Riemann problem.
- Once the interface pressure p^* satisfies the termination criterion, the iteration loops are stopped and the half Riemann problem is evaluated with the determined pressure p^* as input. This computation delivers the interface velocity v^* and density ρ^*.
- Finally, the compressible flux is evaluated on the basis of the star state ρ^*, v^*, p^*.

The scheme presented in this subsection couples the two regions by exchange of velocity and pressure in the compressible flow region and background pressure in the Mach number zero flow region, while the density stays uncoupled across the contact discontinuity. This is in accordance with the physics of the problem as the contact discontinuity represents the material interface. Concerning the Mach number zero region, only the velocity of the compressible phase is of importance, whereas the hydrodynamic pressure remains zero. In the case of the compressible fluid, both variables, pressure and velocity are needed in order to perform the coupling procedure.

3.3.3. Coupling procedure based on multiple pressure variables (MPV)

The objective of the present algorithm is to consider both, thermodynamic and hydrodynamic effects inside the zero Mach number domain. According to the multiple pressure variables (MPV) approach [10], the background pressure $p^{(0)}$ and the hydrodynamic pressure $p^{(2)}$ are used together allowing a compression of the $M = 0$ domain as well as momentum transfer via the effects of the hydrodynamic pressure. The pressure $p^{(2)'}$ in the $M = 0$ region is coupled to the compressible pressure p^* at the domain boundaries

$$p^* = p^{(2)'}. \tag{3.14}$$

With reference to equation (3.8) the hydrodynamic pressure $p^{(2)}$ is only determined up to a constant that includes thermodynamic effects. To finally couple the two different flow regions, this constant has to be evaluated on the basis of the thermodynamic background pressure $p^{(0)}$ that is equivalent to the integral average of the $p^{(2)'}$ distribution in the domain Ω:

$$p^{(0)} = \frac{1}{|\Omega|} \int_\Omega p^{(2)'} d\Omega = p^{(2)'} - p^{(2)}. \tag{3.15}$$

This relation between the two pressures enables to determine the hydrodynamic pressure distribution $p^{(2)}$ in the zero Mach number region. The velocity divergence is allowed to be non-zero. Therefore, a variation of the background pressure is possible with reference to the equation (2.33). Furthermore, the equations (2.41) and (2.49) show that the velocity distribution is linear in space. This is important for the hydrodynamic pressure $p^{(2)}$ that is obtained by spatial integration of equation (2.45) and is therefore described by the quadratic function of equation (2.46).

The focus is now on the setting of Fig. 3.1 that describes the acceleration of a zero Mach number region and that has already been used for the purely hydrodynamic coupling of section 3.3.1. The goal is to include compressible effects to the purely hydrodynamic acceleration by taking into account the thermodynamic background pressure $p^{(0)}$.

The building blocks of the present MPV coupling approach are again the solution of half-Riemann problems for the compressible fluid and the analytical solution of the zero Mach number region such that in the end the compressible fluxes can be calculated at the interface between the $M = 0$ region and the compressible flow domain. The jump conditions across the interface remain

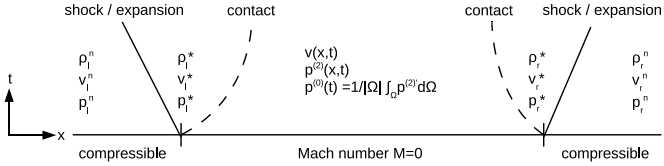

Figure 3.9.: Half-Riemann problems for the combined thermodynamic and hydrodynamic MPV coupling. Thermodynamic and hydrodynamic pressure are coupled to the compressible pressure.

unchanged (cf. equations (3.1)-(3.2)) and the iterative procedure is stopped once the interface pressure satisfies its termination criterion.
Subsequently, a description of the MPV coupling approach is given that determines the compressible fluxes for the temporal update of the flow variables from time t^n to t^{n+1}. At the beginning of the iterative process, the pressures p_l^n and p_r^n are prescribed, as it can be seen in Fig. 3.9. The background pressure $p^{(0)}$ is initialized at the beginning of the computation ($t = 0$) as the arithmetic mean of the surrounding compressible pressures

$$p^{(0)}(t=0) = \frac{1}{2}(p_l(t=0) + p_r(t=0)). \tag{3.16}$$

In contrast to the purely hydrodynamic coupling of section 3.3.1 the pressure gradient $p_x^{(2)}$ of the hydrodynamic pressure $p^{(2)}$ is now linear due to the quadratic distribution. For this reason, a guess of the interface velocities v_l^* and v_r^* is needed to determine the change of the thermodynamic background pressure inside the zero Mach number region. Once this pressure is known, it is possible to evaluate the distribution of the pressure $p^{(2)'}$. Afterwards, the pressure gradient $p_x^{(2)}$ is used to compute the interface velocities v_l^* and v_r^* that serve as input for the half-Riemann problems at the interfaces, such that finally new interface pressures p_l^* and p_r^* are obtained. Then the iteration is repeated, until the termination criterion has been satisfied and the compressible fluxes are computed. This coupling procedure is summarized in Fig. 3.10 and characterized as follows:

- Start with a first guess for the interface velocities $v_{l,r}^*$ and pressures $p_{l,r}^*$. An adequate guess might come from the solution of a two-phase Riemann

problem at the material interface. The guessed pressures and velocities are stored as $v_{l,r}^{**}$ and $p_{l,r}^{**}$ to control the iteration procedure.

- Based on the initial guess for the interface velocities and pressures, the inner loop is started:
  - In a first step, a predictor for the background pressure $p^{(0)n+1}$ is determined from equation (2.42), where the interface velocities $v_{l,r}^{*}$ are inserted.
  - The background density $\rho^{(0)n+1}$ is determined analogously: the interface velocities $v_{l,r}^{*}$ are inserted into equation (2.44).
  - Then, the quadratic pressure distribution $p^{(2)'}(x, t^{n+1})$ is evaluated. This is done, using the compressible pressures $p_{l,r}^{*}$ as boundary conditions. The last unknown of the quadratic function is eliminated by prescribing the computed background pressure $p^{(0)n+1}$ as the integral mean value of the $p^{(2)'}$ distribution

$$\frac{1}{|\Omega|}\int_{\Omega} p^{(2)'}(x, t^{n+1}) d\Omega \stackrel{!}{=} p^{(0)n+1}. \tag{3.17}$$

  - Once the pressure distribution $p^{(2)'n+1}$ is known, the hydrodynamic pressure is obtained as $p^{(2)n+1} = p^{(2)'n+1} - p^{(0)n+1}$ according to equation (3.8) and its spatial gradient can directly be inserted into the discretized momentum equation, delivering new interface velocities $v_{l,r}^{*}$

$$v_{l,r}^{*} = v_{l,r}^{n} - \Delta t \left(v_{l,r}^{n}(v_{l,r}^{n})_x + \frac{(p_{l,r}^{(2)n+1})_x}{\rho^{(0)n+1}} \right). \tag{3.18}$$

  - The new velocity estimates $v_{l,r}^{*}$ are used as input for the half-Riemann problem connecting the compressible states at the left and right to the corresponding interface velocity and pressure. Hence, by prescribing the velocity, a new star pressure $p_{l,r}^{*}$ is obtained at the interface.
  - At each iteration, the new estimates of $p_{l,r}^{*}$ are compared to the old star pressures $p_{l,r}^{**}$. If the pressure change falls below a certain threshold ϵ, the iteration is stopped. Otherwise, the old velocities $v_{l,r}^{*}$ are stored as $v_{l,r}^{**}$, while the same is done for the pressure resulting in $p_{l,r}^{**}$. Then the iteration cycle is repeated by evaluation of a new pressure estimate $p^{(0)n+1}$.

- Once the termination criterion is satisfied, the compressible fluxes are evaluated. Having already determined the pressures $p^*_{l,r}$ and the velocities $v^*_{l,r}$, the only missing part is the density $\rho^*_{l,r}$. On the basis of $p^*_{l,r}$ and $v^*_{l,r}$ the half-Riemann problem is evaluated to compute the interface densities $\rho^*_{l,r}$. Then, the fluxes for the compressible region can directly be calculated based on the star values.

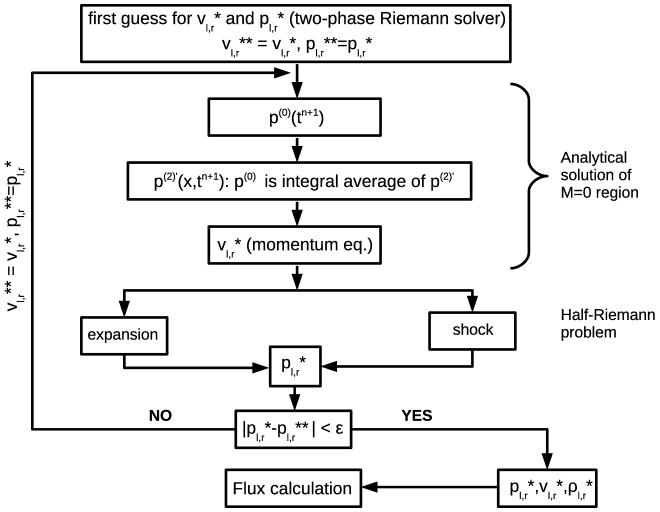

Figure 3.10.: Multiple pressure variables coupling scheme: Background pressure $p^{(0)}$ and hydrodynamic pressure $p^{(2)}$ are coupled to the compressible pressure.

4. Numerics

The focus of the present chapter is on the different numerical schemes that have been used and developed for this work. Based on the existing Free Surface 3D (FS3D) code for the simulation of incompressible two-phase flows, numerical methods are presented that aim at the extension of FS3D to the compressible flow regime.
Starting from the simulation of incompressible flows, the numerical basics of the incompressible FS3D code are briefly presented. Additionally, a detailed description of the surface tension modeling in the context of incompressible flows is given. Two surface tension models are described and the numerical discretization of the surface tension term is discussed including the phenomenon of spurious currents. The origin of the parasitic currents in the FS3D code is shown as well as the remedy for their elimination.
Afterwards, the focus is on the development of a numerical scheme to extend FS3D to compressible two-phase flows. A numerical method is needed that allows to stay as close as possible to the already existing numerical structures, this means the use of a pressure-based numerical solver and the spatial discretization of the flow equations on a staggered grid.
Such a scheme is the pressure-based Multiple Pressure Variables (MPV) method for the simulation of compressible and incompressible flows. The MPV scheme builds upon an asymptotic pressure expansion in order to avoid the singular incompressible limit of the compressible flow equations. The MPV approach for single-phase flows is introduced and extended to compressible two-phase flows on the basis of the inviscid Euler equations in conservative form.
In the multiphase context, special attention is paid on the developed interface treatment for which on the one hand, the thermodynamic transition is happening in a sharp manner without any mixing or blending of the equations of state. On the other hand, the initial density jump between the phases is smeared by the numerical method. It is proved that the first order two-phase MPV approach gives oscillation-free results in the vicinity of a material interface using this interface treatment. This is demonstrated via the detailed analysis of a transport of a two-phase contact discontinuity. Moreover, a semi-conservative MPV formulation is derived where the energy equation is replaced by a pressure

equation in non-conservative form. This gives the scheme additional flexibility as the only remaining link to the equation of state is the speed of sound. The range of applicability of this approach is discussed and shown.
Finally, a short overview is provided concerning two numerical schemes used for validation and verification purposes during the numerical development. This includes a one-dimensional multiphase DG scheme that has served as numerical framework for the validation of the coupling procedures derived in chapter 3. For the single-phase MPV approach, a variety of test cases has been performed to assess its shock-capturing properties and its capability to simulate the propagation of pressure waves. The corresponding numerical results have been compared to those of a standard Godunov-type finite volume solver whose main features are presented briefly.

4.1. The incompressible Free Surface 3D (FS3D) code

The Free Surface 3D (FS3D) code is a DNS VOF method for the simulation of isothermal, incompressible two-phase flows in three space dimensions [29, 38, 45, 46]. The code uses the so-called one-fluid formulation of the incompressible Navier-Stokes equations for two-phase flows, where jump conditions at the material interface are implicitly taken into account by the use of variable material properties [38]. Therefore, the single set of equations (2.51)-(2.52) can be used for the whole flow domain and there is no need to establish any additional jump conditions at the interface.
The coupling of the two fluids is provided by variable material properties ρ and μ and a source term that accounts for the effects of surface tension. It is important for the one-fluid approach that the change in material properties happens in a smooth and regularized way, in order to prevent numerically induced oscillations in the vicinity of the interface. The material properties are chosen according to the fluid occupying a grid cell, depending on the volume fraction variable f of the liquid phase

$$\rho(\vec{x},t) = \rho_g + (\rho_l - \rho_g)\cdot f(\vec{x},t), \tag{4.1}$$
$$\mu(\vec{x},t) = \mu_g + (\mu_l - \mu_g)\cdot f(\vec{x},t), \tag{4.2}$$

where the subscripts g and l denote the gaseous and the liquid phase. Moreover, the incompressible Navier-Stokes equations (2.52) contain an additional source term $\vec{f}_\gamma$ for the surface tension, which is directly linked to the interface location via a delta function δ_S.

The temporal evolution of the volume fraction f is computed with the VOF approach (cf. section 2.7.1) and the incompressible Navier-Stokes equations are solved applying a projection method according to [2] in order to update the velocity at each time step. This leads to a Poisson equation that couples pressure and velocity. A brief overview over this method for the simple first order Euler time discretization is given in the following. More details can be found in [38].
The projection method builds upon a predictor-corrector approach for the velocity. Based on the velocity at the old time level $\vec{v}^n$, at first a temporary velocity $\tilde{\vec{v}}$ is computed by evaluation of the momentum equation taking into account the influences of accelerations due to viscosity, convection, surface tension and other forces excluding the influence of pressure. The resulting predictor velocity field is not divergence-free and has to be corrected. This leads to the solution of a pressure Poisson equation that is derived by application of the zero divergence constraint for velocity to the momentum equation. The solution of the Poisson equation delivers the pressure gradient ∇p^{n+1} of the flow field that finally corrects the predictor velocity $\tilde{\vec{v}}$ according to the divergence constraint. The Poisson equation can be written as follows

$$\nabla \cdot \left[\frac{1}{\rho(f^{n+1})} \nabla p^{n+1} \right] = \frac{\nabla \cdot \tilde{\vec{v}}}{\Delta t}. \tag{4.3}$$

Combining temporary velocity $\tilde{\vec{v}}$ and pressure p^{n+1} from the solution of the Poisson equation, the divergence-free velocity field at the new time level is obtained

$$\vec{v}^{n+1} = \tilde{\vec{v}} - \frac{\Delta t}{\rho(f^{n+1})} \nabla p^{n+1}. \tag{4.4}$$

4.2. Surface tension modeling

In the following, it is shown how surface tension can be modeled and included into the incompressible Navier-Stokes equations. In principle, the description of the pressure jump by equation (2.53) could directly be used in order to derive the volume force $\vec{f_\gamma}$ for the momentum equation (2.52) of the incompressible Navier-Stokes equations as

$$\vec{f_\gamma} = \sigma \kappa \vec{n}, \tag{4.5}$$

where $\vec{n}$ is the interface unit normal vector. However, in the context of the incompressible one-fluid formulation, some numerical smoothing operations for the surface tension force are needed in order to properly take into account

capillary effects near the interface. Therefore, surface tension has to be calculated based on a numerical model. Two common surface tension models for incompressible two-phase flow simulations are briefly presented subsequently.

4.2.1. The continuum surface stress (CSS) model

A widespread model for surface tension is the continuum surface stress (CSS) model of Lafaurie *et al.* [26]. By writing the Navier-Stokes equations in a momentum conserving form, they introduce the capillary pressure tensor

$$\boldsymbol{T} = -\sigma(\boldsymbol{I} - \vec{n} \circ \vec{n})\delta_S, \tag{4.6}$$

where $\boldsymbol{I}$ is the unit tensor. Moreover, the capillary force $\vec{f_\gamma}$ can then be written as the divergence of $\boldsymbol{T}$

$$\vec{f_\gamma} = -\nabla \cdot \boldsymbol{T}. \tag{4.7}$$

Normal vectors and delta function δ_S are calculated based on the gradients of the smoothed volume fraction variable f.

4.2.2. The continuum surface force (CSF) model

The basic idea of the continuum surface force (CSF) model introduced by Brackbill *et al.* [25] can be described as follows. Instead of considering the fluidic interface as a sharp discontinuity, a smooth transition is supposed from one fluid to an other. It is assumed that the interface has a finite thickness that corresponds to the smallest length scale h resolvable by the computational mesh. Consequently, surface tension is also considered to be of continuous nature and it acts everywhere within the transition region. Brackbill *et al.* proposed to replace equation (4.5) by

$$\vec{f_\gamma} = \sigma\kappa\nabla f. \tag{4.8}$$

This corresponds to a weighted dispersion of the surface tension force across a transition region, using the gradient of the volume fraction variable f as weight.

4.3. Parasitic currents in the FS3D code

The following description of parasitic currents and the balanced-force discretization in the context of the incompressible FS3D code is taken from [47]. From a physical point of view, the surface tension force is balanced by the pressure jump across the interface. As the volume force is only different from

zero at the interface, no additional jump conditions with regard to momentum conservation have to be applied. As detailed above, surface tension is numerically approximated by a volume force using a continuum model. For many DNS codes the application of the CSF or CSS model creates unphysical parasitic currents in the vicinity of the surface. However, the presence of parasitic currents limits the range of phenomena accessible by the codes. Especially the simulation of droplets or bubbles with small radii at low speed is often not possible. In these cases, the numerically induced parasitic currents are dominant and therefore lead to unphysical simulation results.
In order to overcome this phenomenon, many efforts have been taken by various researchers. For two-dimensional computations Meier *et al.* [48] proposed a method to determine curvature more accurately using an estimator function, tuned with a least-squares-fit against precomputed reference data. An approximation of the surface tension based on spline interpolants was presented by Ginzburg *et al.* [49]. For three-dimensional calculations, Renardy *et al.* [50] developed the PROST algorithm (parabolic reconstruction of surface tension) and Jafari *et al.* [51] presented the PCIL method (pressure calculation based on the interface location) where the pressure forces at the interfacial cell faces are calculated according to the pressure imposed by each fluid on the portion of the cell face that is occupied by that fluid. This list is far from being complete as there are many other approaches aiming at the reduction of parasitic currents. All of these methods are based on the development of completely new surface tension models. In contrast to this, François *et al.* [27] introduced the notion of the balanced-force discretization of the classical CSF model. According to them, two main ingredients have to be taken into account to reduce spurious velocities:

1. Correct spatial discretization of equation (4.8).

2. Accurate estimation of curvature κ.

The following section details both aspects and shows the adaptation of FS3D to such a balanced-force formulation.

4.3.1. Balanced-force algorithm

The FS3D code uses a spatial discretization based on a Cartesian grid and the variables are stored on a staggered grid arrangement (cf. Fig. 4.4) according to [3]. In the context of the VOF method the volume fraction f is stored at the centers of the mass CVs. In order to guarantee an accurate, balanced-force

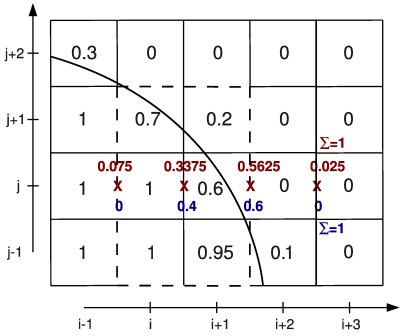

Figure 4.1.: Evaluation of the volume fraction gradient ∇f based on a stencil of 6 cells (red) and on the direct neighbors of the cell face (blue). The box surrounded by the dashed lines marks the 6 cell stencil for the cell face $(i + 1/2, j)$.

discretization, according to [27], the surface tension term $\vec{f}_\gamma$ (cf. equation (4.8)) has to be calculated at the center of the cell faces. Furthermore, it is of crucial importance that pressure and surface tension are discretized in the same way. Special care has to be taken in order to evaluate the gradient of the volume fraction ∇f. In the FS3D code, based on [25], the evaluation of the gradient is performed on a stencil of 18 cells for three-dimensional calculations. For explanation purposes Fig. 4.1 is illustrating a two-dimensional example. Here, the gradients at the cell face centers of row (j) are given by the corresponding values in red. Taking the face at $(i+1/2)$ as an example, the gradient $\nabla f_{x_{i+1/2,j}}$ is based on the gradients in the rows $(j-1), (j), (j+1)$ that are calculated on the basis of the cells adjacent to the face $(i+1/2)$ respectively, e.g. $\tilde{\nabla} f_{x_{i+1/2,j}} = \frac{f_{(i+1,j)} - f_{(i,j)}}{\Delta x}$ for row (j). Here, $\tilde{\nabla}$ designates the local gradient with respect to the cell face. Afterwards, the gradient at the position $x_{i+1/2,j}$ is obtained as

$$\nabla f_{x_{i+1/2,j}} = \frac{1}{4}\left(\tilde{\nabla} f_{x_{i+1/2,j-1}} + 2\tilde{\nabla} f_{x_{i+1/2,j}} + \tilde{\nabla} f_{x_{i+1/2,j+1}}\right). \tag{4.9}$$

This leads to a total stencil for the cell face $(i + 1/2, j)$ that is surrounded by the dashed lines in Fig. 4.1.

It is obvious that the above discretization implies a coupling of the rows $(j-1),(j),(j+1)$ via the evaluation of the gradients for the surface tension calculation. Having a closer look at the discretization of the pressure terms in the Poisson equation (4.3) in x-direction for the cell (i,j), it is found that all pressure values are taken from row (j) and that the rows $(j-1)$ and $(j+1)$ are not included

$$\frac{1}{\Delta x}\left(\frac{p_{(i+1,j)}-p_{(i,j)}}{\rho_{(i+1/2,j)}}-\frac{p_{(i,j)}-p_{(i-1,j)}}{\rho_{(i-1/2,j)}}\right)=\frac{\tilde{\vec{v}}_{(i+1/2,j)}-\tilde{\vec{v}}_{(i-1/2,j)}}{\Delta t}. \tag{4.10}$$

However, the rows $(j-1)$ and $(j+1)$ play a role for the velocity $\tilde{\vec{v}}$ that is directly dependent on the discretization of surface tension where these rows are included as detailed above. It is found that this coupling is one of the causes for the parasitic currents in the FS3D code. Therefore, the gradient evaluation is changed to a more local formulation only taking into account direct neighbors of the cell faces. This leads for the cell face $(i+1/2,j)$ to the following new gradient

$$\nabla f_{x_{i+1/2,j}}=\tilde{\nabla} f_{x_{i+1/2,j}}=\frac{f_{(i+1,j)}-f_{(i,j)}}{\Delta x}, \tag{4.11}$$

instead of the old gradient given by equation (4.9). Returning to Fig. 4.1, the two approaches can be compared directly. According to the two methods, the gradients are given for the previous method (red) and the local approach (blue) in row (j). While the transition from one fluid to the other is spread over four cell faces with the previous approach, the local approach only uses two cell faces to disperse the jump in pressure.
In the three-dimensional case, the gradients for the different space directions are evaluated in an analogous way, only taking into account direct neighbors of the respective cell face.
Besides the discretization of the surface tension force (equation (4.8)), the correct estimation of surface curvature is very important and shall be discussed in the following section.

4.3.2. Curvature Estimation

Topology information like normal vectors and curvature are needed for the surface tension models and have to be determined on the basis of the interface tracking scheme. For level set methods, the calculation of surface normals and curvature is possible by differentiation of the level set variable. As the level set

function is smooth, the derivatives can be evaluated numerically without any problems.
For VOF methods the situation is different as the VOF field is not smooth a priori. The discrete character of the VOF variable complicates the curvature evaluation. If the curvature is directly computed as the second derivative of the volume fraction field, aliasing errors are encountered [52] that do not vanish with grid refinement. To prevent such errors, most VOF approaches smooth the volume fraction field prior to the curvature calculation and this is also the case for the FS3D code.
The curvature evaluation method that is presented here is based on a height function approach, coupled to a local paraboloid fitting if the grid resolution is not sufficient. The procedure is inspired by the work of Popinet [28]. A geometrical height function approach is used whose stencil is variable and adapts itself to capture the local topology in an optimal way as it can be seen in Fig. 4.2(a). The heights are determined in each cell column containing an interface cell by summing up the volume fractions. It is obvious from Fig. 4.2(a) that the summation ends once the cells are completely filled with gas or liquid. In the figure, the resulting height is marked by an arrow and the horizontal, dashed line.
To evaluate the curvature in an interface cell, the height function is determined in the cell column of the interface cell and in the columns of its neighbors. The orientation of the columns is directly depending on the surface normal. The local interface height is calculated following the direction of the largest absolute component of the normal vector. Figure 4.3 illustrates the stencil for the three-dimensional evaluation of the curvature in the central cell column (dashed). To determine the curvature, the heights H in z-direction are computed in all nine cell columns. Then the curvature can be evaluated from the following relation

$$\kappa = \frac{H''}{(1+H')^{3/2}}, \tag{4.12}$$

where the superscript $'$ marks the spatial derivatives of the height function H and a discrete form of equation (4.12) is obtained using finite differences according to [27]

$$\kappa = \frac{H_{xx} + H_{yy} + H_{xx}H_y^2 + H_{yy}H_x^2 - 2H_{xy}H_xH_y}{(1+H_x^2+H_y^2)^{3/2}}. \tag{4.13}$$

The derivatives of the height function H with respect to x and y can simply be evaluated by finite difference approximations. For the x-direction they can

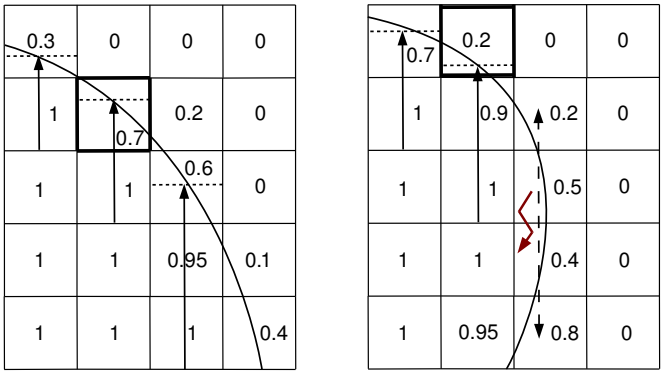

(a) Height function approach with variable stencil.

(b) Insufficient grid resolution inhibits curvature calculation by height functions.

Figure 4.2.: Evaluation of local interface heights based on the liquid volume fraction.

be written as

$$H_x = \frac{H_{i+1,j,k} - H_{i-1,j,k}}{2\Delta x}, \tag{4.14}$$

$$H_{xx} = \frac{H_{i+1,j,k} - 2H_{i,j,k} + H_{i-1,j,k}}{\Delta x^2}. \tag{4.15}$$

The derivatives in the y-direction are calculated in an analogous way and the cross derivative H_{xy} is given as

$$H_{xy} = \frac{H_{i+1,j+1,k} - H_{i+1,j-1,k} - H_{i-1-j+1,k} + H_{i-1,j-1,k}}{2\Delta x \cdot 2\Delta y}. \tag{4.16}$$

As already mentioned, grid resolution is not always sufficient to determine the curvature via the height function approach. This is the case for highly curved topology, for example during breakup, or in case of inappropriate mesh resolution. Such a case is illustrated in Fig. 4.2(b). While the heights can be computed for the two columns at the left, the grid is to coarse to determine a height in the third column. To estimate the local curvature in such cases, a

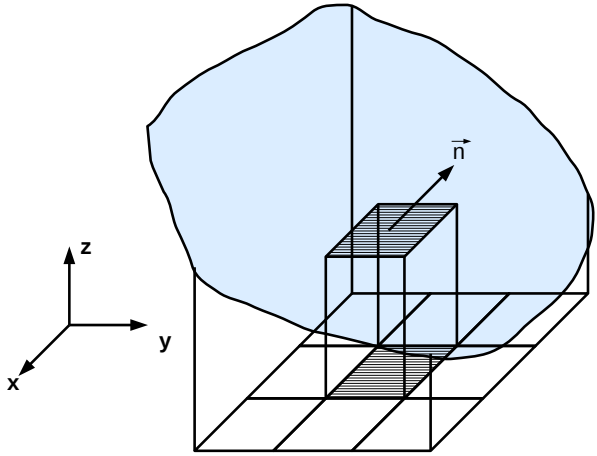

Figure 4.3.: Stencil for the curvature estimation in three space dimensions in the central cell column (dashed) with the largest component of the surface normal in direction of the z-coordinate.

paraboloid is fitted to known points on the surface. For this purpose, first the already available local heights are used and where the local height cannot be computed, the interface reconstruction of the PLIC routine is employed. The PLIC algorithm approaches the surface in each interface cell by a plane whose barycenter is calculated and used for the paraboloid fitting. The fitting is done via a least squares fit of the above determined heights and barycenters. In three space dimensions the paraboloid is given by

$$z = f(a_i, \vec{x}) = a_0 x^2 + a_1 y^2 + a_2 xy + a_3 x + a_4 y + a_5, \tag{4.17}$$

and the curvature can easily be calculated as the second derivative

$$\kappa = 2\frac{a_0(1+a_4^2) + a_1(1+a_3^2) - a_2 a_3 a_4}{(1+a_3^2+a_4^2)^{3/2}}. \tag{4.18}$$

All the above shown procedures apply to an orientation of the surface normal in z-direction. The x- and y-direction are treated in an analogous way.

4.4. The Multiple Pressure Variables (MPV) method

Leaving the incompressible flow regime, the focus is now on the MPV method. This numerical approach extends an incompressible pressure-based flow solver to the compressible regime and in the following, a detailed description of the numerical scheme is given including the temporal and spatial discretization of the MPV method. Moreover, its extension to compressible two-phase flows is presented and open questions and limitations are discussed.

4.4.1. Spatial and temporal discretization of the Euler equations

Starting from the Euler equations (2.25)-(2.27) that include the pressure decomposition (2.23), the discrete set of equations with pressure as primary variable is given as follows for the MPV scheme

$$\begin{pmatrix} \rho \\ \rho\vec{v} \\ p + \gamma p_\infty + (\gamma-1)M^2 e_{kin} \end{pmatrix}_t + \nabla \cdot \begin{pmatrix} \rho\vec{v} \\ (\rho\vec{v}) \circ \vec{v} \\ (\gamma-1)M^2 e_{kin}\vec{v} \end{pmatrix}^{ex} + \nabla \cdot \begin{pmatrix} 0 \\ p^{(2)}\boldsymbol{I} \\ \gamma(p+p_\infty)\vec{v} \end{pmatrix}^{im} = \begin{pmatrix} 0 \\ 0 \\ 0 \end{pmatrix}. \quad (4.19)$$

The superscripts ex and im designate the explicit and implicit time discretization of the respective terms and $\boldsymbol{I}$ stands for the unity matrix. It is evident that the conservation equation for mass is independent from the other equations and is treated in a fully explicit manner while momentum and energy equation contain explicit as well as implicit parts.
Combining compressible and incompressible flows, the MPV approach builds upon a semi-implicit time discretization. This includes an explicit discretization of the convection terms while all terms linked to the speed of sound are discretized implicitly. This procedure takes care of the physical and mathematical background: While the compressible Euler equations build a system of hyperbolic equations where pressure has to obey an equation of state, their incompressible limit is described by a hyperbolic-elliptic system. In the latter case pressure waves are traveling at infinite speed and the incompressible pressure has to guarantee that the divergence constraint for the velocity is satisfied. Therefore, the role of pressure changes and requires an implicit treatment of the pressure terms.

From a numerical point of view, this singular limit is important for the computational time step. For compressible flows, the time step of an explicit numerical scheme has to obey the CFL condition in order to guarantee stability [53]

$$\Delta t \leq C \cdot \min_i \left(\frac{\Delta x}{|u| + (c/M)} \right)_i , \tag{4.20}$$

where C is the Courant number ($C < 1$), Δx designates the length of the cell edge, u stands for the convective velocity, c denotes the speed of sound and i is the cell index. The consideration is limited to the one-dimensional case for the sake of simplicity . It is obvious that for increasing speed of sound, the time step goes to zero. To avoid this singular behavior, the above discussed semi-implicit time discretization is used where all terms that are linked to pressure and therefore the speed of sound, are treated in an implicit manner to guarantee their stability. The stability of the remaining explicit terms only depends on the convective velocity u.
This is obvious from the Jacobian matrix of the explicit flux terms of equation (4.19) in one space dimension. The corresponding eigenvalues are all equal to the flow velocity u and in principle it is possible to choose the time step of the semi-implicit MPV method exclusively on the basis of the convective velocity u

$$\Delta t \leq C \cdot \min_i \left(\frac{\Delta x}{|u|} \right)_i . \tag{4.21}$$

The discretization of space and time is presented subsequently for the MPV scheme according to the method of lines approach that is characterized by a separation of spatial and temporal discretization [1, 54].

4.4.1.1. Temporal discretization

In the following, the focus is on the temporal discretization of the flow equations. As the MPV scheme is based on the method of lines approach, temporal and spatial discretization are done in two separate steps and the equations are now only discretized in time such that a semi-discrete formulation is obtained (still continuous in space but discrete in time).
From a mathematical point of view, the system of partial differential equations (PDE) is transformed into a system of ordinary differential equations (ODE) by the choice of a spatial discretization. In general, the ODE system that results from the semi-implicit MPV approach can be written as follows

$$\frac{d\vec{U}}{dt} = \boldsymbol{f}(\vec{U}^n) + \boldsymbol{g}(\vec{U}^{n+1}), \tag{4.22}$$

where $\vec{U}$ designates the vector of the discretized conservative variables of the Euler equations and n stands for the time level. The operator $\boldsymbol{f}(\vec{U}^n)$ represents the explicitly discretized, non-stiff convective terms while the stiff terms are discretized implicitly and grouped together in the operator $\boldsymbol{g}(\vec{U}^{n+1})$. As is obvious from equation (4.19), the density can be treated in a purely explicit manner as there aren't any pressure terms in the corresponding equation. Yet, momentum and energy equation contain pressure terms and therefore both equations have to be discretized semi-implicitly.

Three different time discretizations are used that are of first and second order accuracy. The first order scheme uses the simple explicit and implicit Euler method that can be expressed as follows

$$\vec{U}^{n+1} = \vec{U}^n + \Delta t \left[\boldsymbol{f}(\vec{U}^n) + \boldsymbol{g}(\vec{U}^{n+1}) \right]. \tag{4.23}$$

To achieve a second order temporal discretization approach two different time integration methods are presented subsequently. The first one is a combination of Runge-Kutta for the explicit part and Crank-Nicolson for the implicit terms of the MPV approach (RK2CN). This approach necessitates the introduction of an intermediate time level at the instant $t^{n+1/2}$

$$\vec{U}^{n+1/2} = \vec{U}^n + \frac{\Delta t}{2} \left[\boldsymbol{f}(\vec{U}^n) + \boldsymbol{g}(\vec{U}^{n+1/2}) \right], \tag{4.24}$$

$$\vec{U}^{n+1} = \vec{U}^n + \Delta t \boldsymbol{f}(\vec{U}^{n+1/2}) + \frac{\Delta t}{2} \left[\boldsymbol{g}(\vec{U}^n) + \boldsymbol{g}(\vec{U}^{n+1}) \right]. \tag{4.25}$$

The second time discretization that is of second order in time is the semi-implicit backward differentiation formula (SBDF) method [11] that is described in appendix A.

A more detailed insight into the temporal discretization of the MPV scheme is given in the following based on [11]. For this purpose, the solution procedure of the first order Euler explicit and implicit time discretization method is

described. The time-discrete Euler equations are given by

$$\frac{\rho^{n+1}-\rho^n}{\Delta t}+\nabla\cdot(\rho\vec{v})^n = 0, \tag{4.26}$$

$$\frac{(\rho\vec{v})^{n+1}-(\rho\vec{v})^n}{\Delta t}+\nabla\cdot(\rho\vec{v}\circ\vec{v})^n+\nabla p^{(2)n+1} = 0, \tag{4.27}$$

$$\begin{aligned}&\frac{\left(p^{(0)}+M^2p^{(2)}+(\gamma-1)M^2e_{kin}\right)^{n+1}}{\Delta t}-\\&\frac{\left(p^{(0)}+M^2p^{(2)}+(\gamma-1)M^2e_{kin}\right)^{n}}{\Delta t}+\\&\nabla\cdot\left[\vec{v}\left((\gamma-1)M^2e_{kin}+\gamma(p^{(0)}+M^2p^{(2)}+p_\infty)\right)\right] = 0.\end{aligned} \tag{4.28}$$

As a first step, the conservation equation of mass is solved

$$\rho^{n+1}=\rho^n-\Delta t\nabla\cdot(\rho\vec{v})^n. \tag{4.29}$$

Once the density ρ^{n+1} at the new time level is known, velocity and pressure are updated on the basis of the momentum equation and the energy equation. To achieve this, the MPV scheme uses a projection method and as it is common for incompressible schemes a Poisson equation for pressure has to be solved. To derive this equation, the following predictor-corrector relations are introduced for pressure and velocity:

$$p^{(2)n+1}=p^{(2)*}+\delta p^{(2)}, \tag{4.30}$$

$$\vec{v}^{n+1}=\vec{v}^{*}+\delta\vec{v}. \tag{4.31}$$

The variables $\delta p^{(2)}$ and $\delta\vec{v}$ designate the corrector values for the corresponding predictors that are marked by the superscript $*$ and the superscript $n+1$ stands for the new time level. As a next step, this ansatz has to be inserted into the momentum equation (4.27) to get a relation between the two correctors $\delta\vec{v}$ and $\delta p^{(2)}$

$$\delta\vec{v}=-\Delta t\frac{\nabla\delta p^{(2)}}{\rho^{n+1}}. \tag{4.32}$$

To update pressure and velocity, the predictors $p^{(2)*}$ and $\vec{v}^*$ have to be determined first. For the pressure, $p^{(2)*}=p^{(2)n}$ is a simple choice and the velocity $\vec{v}^*$ is then easily calculated from the momentum equation

$$\vec{v}^{*}=\frac{1}{\rho^{n+1}}\left((\rho\vec{v})^n-\Delta t\left[(\rho\vec{v}\circ\vec{v})^n+\nabla p^{*}\right]\right). \tag{4.33}$$

The predictor-corrector relations for the pressure $p^{(2)n+1}$ (equation (4.30)) and the velocity $\vec{v}^{n+1}$ (equation (4.31)) are introduced into the energy equation (4.28) together with the relation between the two correctors $\delta p^{(2)}$ and $\delta\vec{v}$ given by equation (4.32). This then results in a Poisson equation for the pressure corrector $\delta p^{(2)}$

$$M^2\delta p^{(2)} - \Delta t^2\nabla\cdot\left[\frac{\gamma(p^e+p_\infty)}{\rho^{n+1}}\nabla\delta p^{(2)}\right] =$$
$$M^2[p^{(2)n} - p^{(2)*}] - dp^{(0)n} - \Delta t\nabla\cdot(\gamma(p^e+p_\infty)\vec{v}^*) - (\gamma-1)M^2\delta k^*, \quad (4.34)$$

where p^e is a tentative value for the pressure at the new time level and $dp^{(0)n}$ describes the effects of outer compression originating from the domain boundaries (cf. equation(2.35))

$$dp^{(0)} = -\frac{\Delta t\cdot\gamma(p^{(0)}+p_\infty)}{|\Omega|}\int_\Omega \vec{v}^n\cdot\vec{n}dA. \quad (4.35)$$

The term δk^* represents the contribution of the kinetic energy e_{kin}

$$\delta k^* = e^*_{kin} - e^n_{kin} + \Delta t\nabla\cdot(e_{kin}\vec{v})^n. \quad (4.36)$$

The kinetic energy e^*_{kin} is an approximation to the energy at the new time level, evaluated on the basis of the explicitly determined density ρ^{n+1} and the predictor velocity $\vec{v}^*$. Due to the use of p^e and e^*_{kin} the Poisson equation is linearized and solved in an iterative way until convergence of $\delta p^{(2)}$ is reached. Then, pressure and velocity can be updated in the whole flow domain using the equations (4.30) and (4.31).

As a final step, the pressure decomposition has to be corrected. At the beginning of the calculation, the compressible pressure is decomposed into the background pressure $p^{(0)}$ and the hydrodynamic pressure $p^{(2)}$. As equation (4.35) is used as a guess for the temporal evolution of $p^{(0)}$, the background pressure $p^{(0)n+1}$ at the new time level is no longer necessarily equivalent to the average of the pressure p^{n+1} and therefore the average of the hydrodynamic pressure $\overline{p^{(2)n+1}}$ does not disappear. For this reason, the average hydrodynamic pressure $\overline{p^{(2)n+1}}$ at the new time level is determined and subtracted from the hydrodynamic pressure $p^{(2)n+1}$ while it is added to the background pressure $p^{(0)n+1}$, such that the consistency of the pressure decomposition is always guaranteed.

4.4.1.2. Spatial discretization

The spatial discretization of the MPV method is carried out on an equidistant, Cartesian, staggered grid in three space dimensions, according to [3]. For the purpose of explanation, such a mesh is depicted in Fig. 4.4 for the two-dimensional case. It is obvious that there are different control volumes (CV) for mass and momentum. While all scalar values like density ρ, pressure p and the level set function Φ are located at the cell center of the mass CV, the velocity components are stored at the center of the momentum CV that coincides with the center of a mass CV cell face. There is a different momentum CV for each space direction as is evident from Fig. 4.4. The same principle applies to three dimensions.

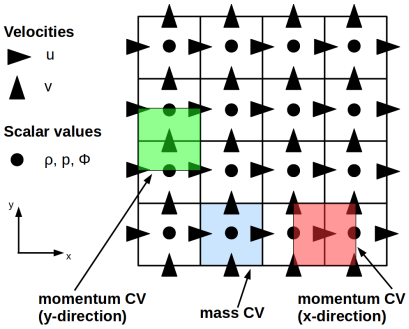

Figure 4.4.: Staggered grid arrangement: different variables and control volumes (CV).

While the MPV scheme uses the conservative Euler equations, the flow variables are stored on the staggered grid as primitive variables. This implies interpolation steps for density and velocity. For example, the momentum $(\rho u)_{i+1/2}$ at the center of the momentum CV $(i + 1/2)$ is calculated as follows

$$(\rho u)_{i+1/2} = \frac{1}{2}(\rho_i + \rho_{i+1})u_{i+1/2}. \tag{4.37}$$

The convective fluxes for the first order spatial discretization are evaluated in a simple upwind manner. To further illustrate this, several examples are given for the flux evaluation in the MPV context. For the sake of simplicity, the

calculations are limited to the fluxes in x-direction.
The density flux in x-direction in cell i is calculated as

$$\frac{\partial}{\partial x}(\rho u)_i = \frac{1}{\Delta x}\left[(\rho u)_{i+1/2} - (\rho u)_{i-1/2}\right], \tag{4.38}$$

and

$$(\rho u)_{i+1/2} = u_{i+1/2}\begin{cases}\rho_i & \text{for} \quad u_{i+1/2} > 0,\\ \rho_{i+1} & \text{for} \quad u_{i+1/2} \leq 0.\end{cases} \tag{4.39}$$

The same applies to $(\rho u)_{i-1/2}$ and all the other density fluxes. For the momentum, the fluxes are determined in an analogous way, taking into account the shifted momentum CV on the staggered grid. The momentum flux in x-direction is obtained as

$$\frac{\partial}{\partial x}((\rho u)u)_{i+1/2} = \frac{1}{\Delta x}\left[((\rho u)u)_{i+1} - ((\rho u)u)_i\right], \tag{4.40}$$

and

$$((\rho u)u)_{i+1} = u_{i+1}\begin{cases}(\rho u)_{i+1/2} & \text{for} \quad u_{i+1} > 0,\\ (\rho u)_{i+3/2} & \text{for} \quad u_{i+1} \leq 0,\end{cases} \tag{4.41}$$

with

$$u_{i+1} = \frac{1}{2}(u_{i+1/2} + u_{i+3/2}). \tag{4.42}$$

The momenta $(\rho u)_{i+1/2}$ and $(\rho u)_{i+3/2}$ are evaluated according to equation (4.37). For the second order MPV scheme, a linear reconstruction is performed based on the MUSCL approach [55]. In every cell the flow variables are reconstructed in a piecewise linear way in each space direction using slope limiters as it is illustrated by the following example for the density reconstruction in x-direction. First, a slope inside each cell has to be determined such that no new maxima are created by the reconstruction process. A quite simple slope limiter is the minmod limiter

$$\text{minmod}(a,b) = \begin{cases}a & \text{for} \quad |a| \leq |b|\,, ab > 0,\\ b & \text{for} \quad |a| > |b|\,, ab > 0,\\ 0 & \text{for} \quad ab < 0.\end{cases} \tag{4.43}$$

Here a and b are the left and right differential quotients of the density

$$a = \frac{\rho_i - \rho_{i-1}}{x_i - x_{i-1}}, \tag{4.44}$$

$$b = \frac{\rho_{i+1} - \rho_i}{x_{i+1} - x_i}. \tag{4.45}$$

The slope $s_{\rho,i}$ in cell (i) is then determined as

$$s_{\rho,i} = \text{minmod}(a, b), \tag{4.46}$$

such that the reconstructed density at the cell boundary $(i + 1/2)$ is obtained as

$$\rho_{i+1/2,-} = \rho_i + \frac{\Delta x}{2} s_{\rho,i}, \tag{4.47}$$

$$\rho_{i+1/2,+} = \rho_{i+1} - \frac{\Delta x}{2} s_{\rho,i+1}. \tag{4.48}$$

The $+$ and $-$ sign designate the reconstructed variable at the location $(i+1/2)$ in the right cell $(i + 1)$ and in the left cell (i), respectively.
Finally, the density flux calculation (4.39) can be simply adapted to the reconstructed density values

$$(\rho u)_{i+1/2} = u_{i+1/2} \begin{cases} \rho_{i+1/2,-} & \text{for} \quad u_{i+1/2} > 0, \\ \rho_{i+1/2,+} & \text{for} \quad u_{i+1/2} \leq 0. \end{cases} \tag{4.49}$$

The same principle applies to the other space directions and flow variables.
Special attention has to be paid on the discretization of the Poisson equation for pressure. While the left-hand side of equation (4.34) is discretized with finite differences, an upwind flux formulation is used on the right-hand side for the pressure term.
The pressure derivatives on the left-hand side are evaluated by central difference approximations, similar to classical incompressible schemes. On a staggered grid, the decoupling of pressure and velocity is automatically avoided, however special care has to be taken with respect to the discretized divergence operator on the left-hand side and the discretization is illustrated by the following one-dimensional example for the x-direction

$$\begin{aligned} \nabla \cdot \left[\frac{\gamma(p^e + p_\infty)}{\rho^{n+1}} \nabla \delta p^{(2)} \right] &= \frac{1}{\Delta x^2} \left[\left(\frac{\gamma(p^e+p_\infty)}{\rho^{n+1}} \right)_{i+1/2} \cdot (\delta p_{i+1}^{(2)} - \delta p_i^{(2)}) \right] - \\ &\quad \frac{1}{\Delta x^2} \left[\left(\frac{\gamma(p^e+p_\infty)}{\rho^{n+1}} \right)_{i-1/2} \cdot (\delta p_i^{(2)} - \delta p_{i-1}^{(2)}) \right]. \end{aligned} \tag{4.50}$$

Interpolation operations for density and pressure have to be performed in order to get the corresponding values at the faces of the mass CV $(i \pm 1/2)$.
On the right-hand side of the Poisson equation (4.34), there is the term

$$\nabla \cdot (\gamma p^e \vec{v}^*), \tag{4.51}$$

involving the spatial derivatives of pressure and velocity. Contrary to the above central discretization this term has to be handled in an upwind manner. This upwind treatment guarantees accurate simulation results as a central finite difference approximation leads to oscillations at the location of shocks. For the sake of explanation, only the flux calculation for the x-direction is shown and fluxes in the other spatial directions are calculated in an analogous way

$$\nabla \cdot (\gamma p^e u^*) = \frac{\gamma}{\Delta x} \left[(p^e u^*)_{i+1/2} - (p^e u^*)_{i-1/2} \right], \tag{4.52}$$

and for the first order case, the flux is determined as

$$(p^e u^*)_{i+1/2} = u^*_{i+1/2} \begin{cases} p^e_i & \text{for} \quad u^*_{i+1/2} > 0, \\ p^e_{i+1} & \text{for} \quad u^*_{i+1/2} \leq 0. \end{cases} \tag{4.53}$$

4.5. A semi-conservative MPV approach

The previous sections have shown a direct dependence of the discretized MPV scheme on the equation of state. This dependency comes from the introduction of pressure as primary variable and the reformulation of the energy equation (2.21) in terms of the pressure variables $p^{(0)}$ and $p^{(2)}$. In order to replace the internal energy by the corresponding pressure terms, an equation of state has to be given in analytical form. If the equation of state is not explicitly given in an analytical formulation, the above described reformulation of the energy equation is not easily possible and an alternative approach is needed. For a general equation of state, Fedkiw *et al.* [56] proposed to reformulate the convective derivative of the pressure in order to get a nonconservative pressure equation

$$\frac{Dp}{Dt} = p_\rho \frac{D\rho}{Dt} + p_e \frac{De}{Dt}. \tag{4.54}$$

Here, p_ρ and p_e denote the partial derivatives of pressure with respect to density and total energy, respectively. Finally, by using mass and momentum equations the following equation is obtained according to [56]

$$\frac{\partial p}{\partial t} + \vec{v} \cdot \nabla p = -\rho c^2 \nabla \cdot \vec{v}. \tag{4.55}$$

To use this pressure equation in the MPV context, the pressure decomposition of equation (2.23) has to be introduced

$$\frac{\partial}{\partial t}(p^{(0)} + M^2 p^{(2)}) + \vec{v} \cdot \nabla p^{(2)} = -\rho c^2 \nabla \cdot \vec{v}. \tag{4.56}$$

The only remaining link of equation (4.56) to the equation of state is established by the speed of sound c. Hence, this formulation allows to directly apply the MPV scheme to an arbitrary equation of state when the energy equation is replaced by equation (4.56).
The resulting MPV method for the Euler equations can be considered to be semi-conservative as the conservative pressure equation (2.27) is replaced by the nonconservative equation (4.56) while the mass and momentum equations are kept in conservative form (cf. equations (2.25)-(2.26)). Equation (4.56) is now discretized in an implicit manner

$$\frac{\partial p}{\partial t} + (\vec{v} \cdot \nabla p)^{n+1} = -(\rho c^2 \nabla \cdot \vec{v})^{n+1}. \tag{4.57}$$

The pressure equation is linearized by the use of the estimates p^e and c^e for the pressure and the speed of sound at the new time level

$$\frac{\partial p}{\partial t} + \vec{v}^{n+1} \cdot \nabla p^e = -\rho^{n+1} (c^e)^2 \nabla \cdot \vec{v}^{n+1}. \tag{4.58}$$

With respect to the conservative MPV approach, only the energy equation is modified while the conservation equations for mass and momentum stay the same. Therefore, a new Poisson equation for the pressure corrector $\delta p^{(2)}$ has to be derived from equation (4.58) by introducing the predictor-corrector ansatz given by the equations (4.30)-(4.32). The resulting Poisson equation can be written for the first order Euler time discretization as

$$\begin{aligned} M^2 \delta p^{(2)} - \Delta t^2 \left[\frac{\nabla p^e}{\rho^{n+1}} \cdot \nabla \delta p^{(2)} + \rho^{n+1} (c^e)^2 \nabla \cdot \left(\frac{1}{\rho^{n+1}} \nabla \delta p^{(2)} \right) \right] = \\ M^2 (p^{(2)n} - p^{(2)*}) - dp^{(0)} - \Delta t (\vec{v^*} \nabla p^e + \rho^{n+1} (c^e)^2 \nabla \cdot \vec{v^*}), \end{aligned} \tag{4.59}$$

and is finally solved iteratively.
The use of non-conservative formulations and primitive variables leads generally to a decoupling of internal and kinetic energy. It will be shown by numerical computations in sections 5.1.2.2 and 5.1.2.3 that the present approach is still capable to accurately capture weak shocks, while it has problems to correctly predict stronger shocks.
For the following investigations, the conservative MPV method described in section 4.4 is used, unless otherwise stated.

4.6. Extension of the MPV scheme to compressible two-phase flows

This section describes the extension of the MPV method to two-phase flows, as it has been presented in [57, 58]. At first, it is explained how the MPV approach tracks the interface and how the thermodynamic transition from one fluid to an other is handled. Afterwards, the investigation of the transport of a two-phase contact discontinuity proves that the MPV method does not suffer from unphysical velocity and pressure oscillations at the material interface.

The DNS of compressible two-phase flows is a rather challenging task as the two fluids often differ significantly in their material properties as well as in their thermodynamic behavior expressed by the equation of state. For this reason, it is crucial to accurately know and track the interface location at each time step. Additionally, the thermodynamic transition between the two fluids has to be handled numerically.

Introducing the level set function Φ and its transport equation (2.58) to the MPV solver, it is possible to describe and evolve the material interface in the course of the computation. The level set Φ is initialized as a signed distance function with respect to the interface, such that its zero level set coincides with the interface location.
Numerically, the level set variable is transported using the pseudo-conservative formulation of equation (2.59). This allows to easily implement the level set method in a standard conservation scheme like a finite volume solver. The level set equation can then be treated analogously to the mass conservation as the same upwind flux calculation can be used taking into account the additional term on the right-hand side of equation (2.59).

The two-phase MPV approach builds upon a sharp thermodynamic transition without any mixing of the different equations of state. Each grid cell is exclusively assigned to one fluid and therefore to a specific equation of state. In general, the different fluids can be easily identified depending on the sign of the level set. While Φ has a positive sign in the gaseous phase, it is negative in the liquid phase. Due to the use of the general stiffened gas equation of state (2.24) the MPV method offers the possibility to treat two different fluids by the same equation of state without any difficulty. The fluids differ in the constants γ and p_∞ that are allowed to vary from one grid cell to an other such that each cell (i, j, k) is assigned to a specific value $\gamma_{(i,j,k)}$ and $p_{\infty,(i,j,k)}$. At every time step, a loop over all grid cells is performed and based on the level set variable the corresponding values $\gamma_{(i,j,k)}$ and $p_{\infty,(i,j,k)}$ are set. This treatment shifts

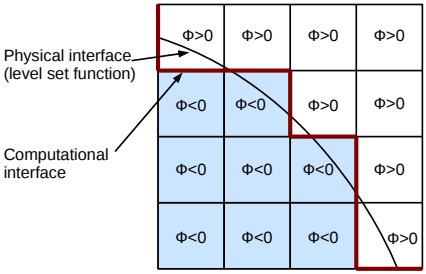

Figure 4.5.: Physical and computational interface.

the physical interface to the cell faces, creating a computational interface that is of staircase shape, as it can be seen in Fig. 4.5. Once $\gamma_{(i,j,k)}$ and $p_{\infty,(i,j,k)}$ are assigned, the usual MPV solution procedure of the Poisson equation can be applied. For the first order Euler time discretization the Poisson equation is written as follows

$$M^2\delta p^{(2)} - \Delta t^2 \nabla \cdot \left[\frac{\gamma_{(i,j,k)}(p^e + p_{\infty,(i,j,k)})}{\rho^{n+1}} \nabla \delta p^{(2)}\right] = M^2[p^{(2)n} - p^{(2)*}] - dp^{(0)n} - \Delta t \nabla \cdot (\gamma_{(i,j,k)}(p^e + p_{\infty,(i,j,k)})\vec{v^*}) - (\gamma_{(i,j,k)} - 1)M^2\delta k^*. \quad (4.60)$$

Similar to the conservative single-phase flow case, the term $\nabla \cdot (\gamma_{(i,j,k)} p^e \vec{v^*})$ is treated as a pressure flux in order to avoid numerical inaccuracies for shock waves. Yet, in the specific case of a multiphase shock tube that corresponds to an air bubble collapse in water, the treatment of the pressure term has to be modified in order to properly capture the shock wave.
The test case is described in more detail in section 5.1.5.4 and it is characterized by strong density and pressure jumps. Considering the fact that the pressure term $\nabla \cdot (\gamma_{(i,j,k)} p^e \vec{v^*})$ has been created applying an equation of state to replace energy by pressure it also represents a part of the internal energy of the corresponding fluids. In the present simulation of the air bubble collapse, the two fluids differ significantly in the internal energy across the multi-material interface. To take this into account, the standard upwind pressure flux at the interface is replaced by two flux terms where each of them is suited to the corresponding fluid. As the test case is one-dimensional, the following example

of the modified flux is limited to the x-direction, while the same principle can be applied to the other directions:

$$\begin{cases} \frac{\partial}{\partial x}(\gamma p^e u^*)_i = \gamma_i \frac{p_i^e (u^*_{i+1/2} - u^*_{i-1/2})}{\Delta x} & u^*_{i+1/2} < 0, \\ \frac{\partial}{\partial x}(\gamma p^e u^*)_{i+1} = \gamma_{i+1} \frac{p_{i+1}^e (u^*_{i+3/2} - u^*_{i+1/2})}{\Delta x} & u^*_{i+1/2} > 0. \end{cases} \tag{4.61}$$

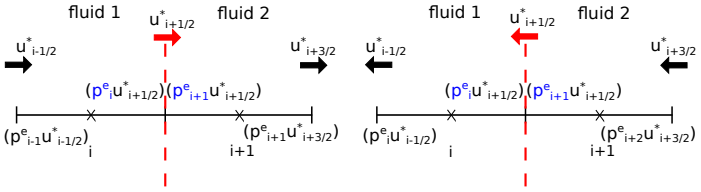

(a) Right moving interface. (b) Left moving interface.

Figure 4.6.: Interface treatment for the $(p^e u^*)$ flux term. At the interface, the $(p^e u^*)$ flux term is evaluated separately for each fluid as the upwind procedure cannot be applied.

Figure. 4.6 illustrates the flux calculation. It shows the case of a left and a right moving interface and it is evident that there are now two flux terms that are evaluated at the interface location $(i+1/2)$ instead of a single upwind flux. Independently of the flow direction, the pressure p^e for the flux evaluation is always equal to p_i^e in cell (i) and to p_{i+1}^e in cell $(i+1)$ for an interface located at $(i+1/2)$.
This corresponds to a nonconservative flux evaluation at the material interface. While this treatment improves the simulation results for the air bubble collapse problem, there are other test cases where the nonconservative fluxes corrupt the shock-capturing capabilities of the MPV scheme.
Unless otherwise stated, the fluxes are determined in a conservative manner for the calculations presented in chapter 5.

4.6.1. Transport of a two-phase contact discontinuity

The material interface represents a discontinuity in the equation of state that may lead to spurious pressure and velocity oscillations at this location, es-

pecially when density-based flow solvers in conservative formulation are used without any special interface treatment [43].
A simple but crucial test case is the transport of a two-phase contact discontinuity in one space dimension. Once the discontinuity is transported, it is smeared numerically by standard flow solvers. The smearing of the density may cause problems for density-based solvers and possibly introduce spurious pressure oscillations as a stiff equation of state is very sensitive to the density smearing. The oscillations are amplified by the numerical scheme and if a numerical method suffers from such oscillations, a special interface treatment is needed [43].
The MPV scheme does not suffer from these unphysical oscillations. The pressure is used as primary variable, this means it is directly calculated by the numerical scheme solving the corresponding Poisson equation. For a conservative density-based method, the situation is slightly different. The pressure is treated as secondary variable and is computed from the equation of state and the internal energy. This makes the scheme prone to the smearing of density and energy as the resulting unphysical values introduced into the equation of state lead to an incorrect pressure. In this context, the advantage of the MPV scheme lies in the fact that it is based on the conservative Euler equations, which are subsequently reformulated in primitive variables such that pressure and velocity are used as primary variables.
The following considerations are done on the basis of the conservative MPV scheme that is presented in section 4.4 and that is extended to two-phase flows according to the current section. A closer look at the transport of a one-dimensional two-phase contact discontinuity with the first order spatial discretization shows the oscillation-free behavior of the first order MPV method. For this simple case, velocity and pressure are constant in the whole flow domain and only density is jumping across the contact discontinuity, as well as the material coefficients γ and p_∞.
For the test, two fluids with densities ρ_L, ρ_R and material coefficients γ_L, γ_R and $p_{\infty,L}$, $p_{\infty,R}$ are considered, where the subscripts L and R mark the left and right fluid. Pressure p and velocity $u > 0$ are constant in the whole domain. Let the initial discontinuity be located at the cell face $(i + 1/2)$. The setup is illustrated in Fig. 4.7.
In the following, a detailed investigation of the discretized equations shows the oscillation-free transport. At first, the mass equation is solved and there is only cell $(i + 1)$ that has to be updated

$$\rho_{i+1}^{n+1} = \rho_R - \frac{\Delta t}{\Delta x} u(\rho_R - \rho_L). \tag{4.62}$$

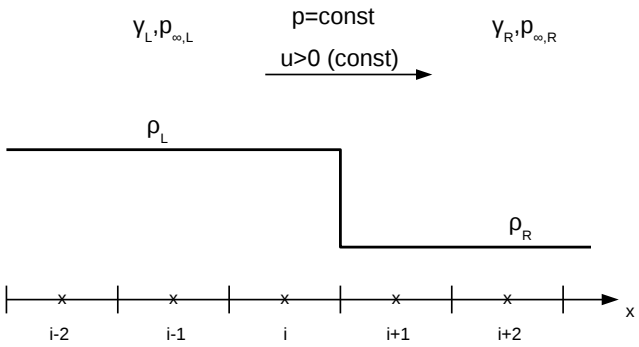

Figure 4.7.: Transport of a two-phase contact discontinuity. Initialization with jump in density and the material coefficients γ and p_∞.

Then, the momentum equation is evaluated in order to get the predictor velocity u^*. Again, there is only one value that has to be updated, this time it is the velocity at the location $(i + 1/2)$

$$u^*_{i+1/2} = \frac{1}{\rho_i^{n+1} + \rho_{i+1}^{n+1}} \cdot \left(\rho_L + \rho_R - \frac{\Delta t}{\Delta x} u(\rho_R - \rho_L) \right) \cdot u. \tag{4.63}$$

As the density $\rho_i^{n+1} = \rho_L$ stays unchanged, the sum $\rho_i^{n+1} + \rho_{i+1}^{n+1}$ can directly be evaluated as

$$\rho_i^{n+1} + \rho_{i+1}^{n+1} = \rho_L + \rho_R - \frac{\Delta t}{\Delta x} u(\rho_R - \rho_L). \tag{4.64}$$

Inserting the sum of the densities $\rho_i^{n+1} + \rho_{i+1}^{n+1}$ calculated in equation (4.64) into equation (4.63) for the velocity predictor $u^*_{i+1/2}$ it is obvious that the predictor is always equal to the constant transport velocity

$$u^*_{i+1/2} = u. \tag{4.65}$$

The last step of the MPV scheme is the solution of the Poisson equation (4.60). A look at the right-hand side shows that for constant pressure and velocity,

there is only the term δk^* that is different from zero

$$\overbrace{M^2[p^{(2)n} - p^{(2)*}]}^{=0 \text{ for } p=const} - \overbrace{dp^{(0)n}}^{=0 \text{ for } u=const}$$
$$\underbrace{-\Delta t \nabla \cdot (\gamma_{(i,j,k)}(p^e + p_{\infty,(i,j,k)})u^*}_{=0 \text{ for } p=const \text{ and } u=const} - (\gamma_{(i,j,k)} - 1)M^2 \delta k^*. \tag{4.66}$$

As for the density, the investigation can be focused on cell $(i+1)$ since all other terms δk^* are equal to zero a priori

$$\begin{aligned} \delta k^*_{i+1} &= (e^*_{kin})_{i+1} - (e^n_{kin})_{i+1} + \Delta t \nabla \cdot (e_{kin} u)^n_{i+1}, \\ &= \frac{1}{2}\left(\rho_R - \frac{\Delta t}{\Delta x} u(\rho_R - \rho_L)\right) \cdot u^2 - \frac{1}{2}\rho_R u^2 + \frac{1}{2}\frac{\Delta t}{\Delta x}(\rho_R - \rho_L)u^3, \\ &= 0. \end{aligned} \tag{4.67}$$

Hence, the right-hand side of equation (4.60) is always equal to zero for constant pressure and velocity independent of the material coefficients γ and p_∞. Therefore, the pressure corrector is also equal to zero everywhere $\delta p^{(2)} = 0$ such that pressure and velocity remain unchanged and the first order scheme is oscillation-free in the vicinity of the interface.

4.7. Limitations of the MPV method and open questions

In the following section, some open questions are presented that have to be dealt with for the future development of the MPV method. The discussed issues have been noticed during the validation and verification process of the numerical approach and a closer investigation of the phenomena showed that fundamental questions seem to arise concerning the numerical method, its discretization in space and time and the treatment of the boundary conditions.

4.7.1. Second order MPV approach in space and time with high density ratios across contact discontinuities

With the extension of the MPV method to second order in space and time, the oscillation-free behavior of the numerical scheme close to density discontinuities can no longer be guaranteed. It is shown that this behavior is basically linked to the interplay of spatial and temporal discretization on the one hand and the interpolation steps on the staggered grid on the other hand.

Analogously to the transport of the contact discontinuity for the first order scheme in section 4.6.1, the focus is now on the same one-dimensional setting displayed in Fig. 4.7. This time, the second order RK2CN time discretization in combination with the spatial reconstruction of the flow variables is used (cf. sections 4.4.1.1 and 4.4.1.2). The test can be limited to a gaseous single-phase flow ($\gamma_L = \gamma_R$ and $p_{\infty,L} = p_{\infty,R} = 0$) with contact discontinuity and jump in density (ρ_L, ρ_R), where the subscripts L and R mark the regions left and right of the discontinuity. Pressure p and velocity $u > 0$ are constant and the initial discontinuity in density is located at the cell face $(i + 1/2)$.
A first look at the one-dimensional momentum equation in semi-discrete formulation (discrete in time) already reveals a difference compared to the first order scheme as there appears the intermediate time level $n + 1/2$

$$\frac{(\rho u)^{n+1} - (\rho u)^n}{\Delta t} + \left[\frac{\partial (\rho u^2)^{n+1/2}}{\partial x} + \frac{1}{2} \left(\frac{\partial p^{(2)n}}{\partial x} + \frac{\partial p^{(2)n+1}}{\partial x} \right) \right]. \tag{4.68}$$

From the discrete formulation of this equation the velocity predictor $u^*_{i+1/2}$ at the location of the contact discontinuity can easily be determined as pressure and velocity initially are constant everywhere

$$u^*_{i+1/2} = \frac{2}{\rho_i^{n+1} + \rho_{i+1}^{n+1}} \cdot \left[(\rho u)^n_{i+1/2} - \frac{\Delta t}{\Delta x} \left((\rho u^2)_{i+1}^{n+1/2} - (\rho u^2)_i^{n+1/2} \right) \right]. \tag{4.69}$$

However, the difficulty lies now in the computation of the momentum flux term at the instant $t^{n+1/2}$

$$\frac{1}{\Delta x} \left((\rho u^2)_{i+1}^{n+1/2} - (\rho u^2)_i^{n+1/2} \right). \tag{4.70}$$

For the flux term evaluation, the density $\rho^{n+1/2}$ and the velocity $u^{n+1/2}$ have to be known and they are computed with the first order Euler scheme. While the velocity stays constant during this step due to the properties of the first order scheme (cf. section 4.6.1) the density has to be updated to the time level $n + 1/2$, but changes only in cell $(i + 1)$ and the corresponding density is obtained as

$$\rho_{i+1}^{n+1/2} = \rho_R - \frac{1}{2} \frac{\Delta t}{\Delta x} u (\rho_R - \rho_L). \tag{4.71}$$

In a next step, the momentum at time level $n + 1/2$ is determined. Based on the density $\rho^{(n+1/2)}$ this is done by simply averaging the surrounding density

values to the cell center of the momentum control volumes where the velocity u is already available

$$(\rho u)_{i+1/2}^{n+1/2} = \left(\frac{\rho_i + \rho_{i+1}}{2} u_{i+1/2}\right)^{n+1/2}. \tag{4.72}$$

This interpolation applies to all momentum control volumes. Afterwards, the momentum is linearly reconstructed using the MUSCL approach. Finally, the momentum flux term reads as follows

$$\frac{1}{\Delta x}\left((\rho u^2)_{i+1}^{n+1/2} - (\rho u^2)_{i}^{n+1/2}\right) = \frac{1}{\Delta x}\frac{3}{4}(\rho_R - \rho_L)u^2\left[1 - \frac{1}{2}\frac{\Delta t}{\Delta x}u\right]. \tag{4.73}$$

In order to evaluate equation (4.69), the density update to time level $n+1$ has to be done additionally. Following the RK2CN procedure this also includes the intermediate time level $n + 1/2$ and a spatial reconstruction step for the calculation of the density fluxes. For the sake of brevity, these steps are omitted and the focus is directly on the discrete form of equation (4.69)

$$u_{i+1/2}^{*} = \frac{\frac{1}{2}\left[\rho_L + \rho_R - \frac{3}{2}\frac{\Delta t}{\Delta x}(\rho_R - \rho_L)(1 - \frac{1}{2}\frac{\Delta t}{\Delta x}u)u\right]}{\frac{1}{2}\left[\rho_L + \rho_R - \frac{\Delta t}{\Delta x}(\rho_R - \rho_L)(1 - \frac{1}{4}\frac{\Delta t}{\Delta x}u)u\right]} \cdot u. \tag{4.74}$$

It is obvious that in contrast to the first order case (cf. equations (4.63)-(4.64)) the numerator and the denominator of the fraction in equation (4.74) do not cancel, therefore the predictor velocity $u_{i+1/2}^{*}$ is different from u.
Moreover, the right-hand side of the pressure Poisson equation (4.60) is also different from zero in the present case and the remaining term there is

$$(\rho_R - \rho_L)\frac{\Delta t}{\Delta x}u^3\left(\frac{1}{8}u\frac{\Delta t}{\Delta x} - \frac{1}{2}\right). \tag{4.75}$$

This directly leads to velocity and pressure oscillations. It can be seen from equation (4.74) that the differences between numerator and denominator get more important the more the two densities ρ_L and ρ_R differ from each other. Additionally, the more the velocity u is different from zero the more the oscillations are pronounced. This is also the case for the remaining term (4.75) of the Poisson equation and it directly explains why the problem is of minor importance for small density ratios and low flow velocities but leads to spurious oscillations once the densities differ by several orders of magnitude. This behavior is illustrated by two numerical examples in section 5.1.3.1.

4.7.2. Outlet boundary conditions

The outlet boundary conditions of the conservative MPV scheme on a staggered grid in one space dimension are discussed in the following.
For the MPV method, the outlet boundary condition is realized using ghost cells at the domain boundaries as it is common for finite volume schemes. In order to realize non-reflecting boundary conditions, the values of the first and last grid cell of the domain are copied to the corresponding ghost cell in each space direction, such that the gradient of the flow variables vanishes. For standard finite volume Godunov-type methods this procedure allows one-dimensional shock and expansion waves to leave the domain without any reflection at the domain boundary. Yet, this is not the case for the pressure-based MPV method, as it is shown in section 5.1.3.2 where a numerical analysis of the outlet boundary conditions is presented.

4.8. Numerical codes for validation and verification processes

In this section, two codes are briefly presented that have been used to validate the coupling procedures of chapter 3 and to assess the capabilities of the MPV method regarding the simulation of pressure waves.

4.8.1. One-dimensional sharp interface coupling approach

The compressible-incompressible coupling procedures of section 3 are numerically investigated using a one-dimensional sharp interface approach for the simulation of compressible two-phase flows. This code has originally been designed to simulate two fluids of different compressibility, characterized by dissimilar equations of state. The numerical scheme is based on the Euler equations and allows to track the movement of a material interface and the developed coupling schemes can be used at the interface location to prescribe the conservative flow variables for the numerical flux calculation.
In the following, it is shown how the coupling algorithms are implemented into the one-dimensional framework. The compressible two-phase solver (cf. appendix B) is able to handle the coupling of compressible and weakly compressible flow regions with the ghost fluid method. For this purpose, the whole flow domain is discretized and a numerical solution is computed as is depicted in Fig. 4.8. It can be seen that a weakly compressible region is approaching the zero Mach number limit. However, as the speed of sound is very high

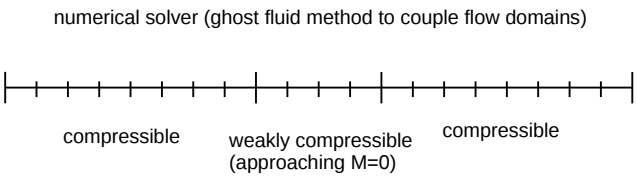

Figure 4.8.: The whole computational domain is discretized and solved numerically by the ghost fluid approach of the one-dimensional framework. The zero Mach number limit is approached by a weakly compressible fluid. This setting is used to compute the reference solution for the compressible flow domains.

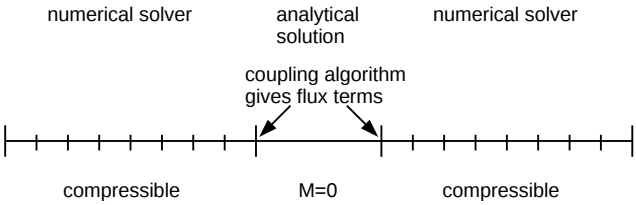

Figure 4.9.: The zero Mach number region is solved analytically and is therefore not discretized. The iterative coupling algorithm delivers the flux terms needed as boundary condition for the compressible solver of the one-dimensional framework.

in this region, its numerical discretization introduces small time steps and is slowing down the computation. In order to prevent this, the presented coupling algorithms can be used that do not discretize the $M = 0$ region but treat it analytically and provide the compressible fluxes at the domain boundaries. This is practical if the pressure waves inside the zero Mach number region can be neglected and it is not necessary to resolve them. With the use of such a coupling scheme, the configuration with respect to the numerical discretization and solution procedure changes to the setting illustrated in Fig. 4.9.

A more extensive description of the sharp interface scheme can be found in appendix B and even more details are presented in [59] by Jaegle *et al.*

4.8.2. Godunov-type finite volume solver

To assess the shock-capturing properties of the MPV scheme and its capabilities for the simulation of pressure waves, an extensive numerical investigation is performed that includes several test cases. The numerical results are compared to those of a standard finite volume solver that serves as a reference.
In contrast to the pressure-based MPV approach, the employed finite volume code is a density-based method that discretizes the flow equations on a collocated spatial grid. Moreover, an explicit time discretization is used. With regard to the numerical fluxes, they are computed on the basis of Riemann solvers such that the finite volume approach is of Godunov-type.
In appendix C the basic ideas of a Godunov-type finite volume approach are briefly described.

5. Computational results

The focus of this chapter is on the assessment and validation of the numerical approaches that have been presented in the chapters 3 and 4. This includes the fundamental investigation of the one-dimensional coupling procedures for compressible and incompressible flow regions as well as the application of the MPV approach to several single-phase and multi-material shock tube test cases in one space dimension. In the three-dimensional space, incompressible and compressible two-phase flows are investigated. In the incompressible flow regime the simulation of surface tension is addressed and compressible flows with pressure waves are simulated using the MPV method.

5.1. One-dimensional calculations

The developed numerical schemes are now applied to one-dimensional test cases for validation and verification purposes. First, the coupling schemes for compressible and incompressible flow regions are validated by the computation of the two test cases presented in section 3.2. Afterwards, the pressure-based MPV method is assessed with respect to its shock-capturing properties for single-phase flows and compared to a density-based Godunov-type scheme. Moreover, the MPV approach for the simulation of compressible multiphase flows is validated. This validation process ranges from the transport of a simple contact discontinuity between two gases to the simulation of numerically demanding two-phase shock tube problems.

5.1.1. Coupling of compressible and incompressible flow regions

In this section, the coupling schemes of section 3.3 are applied to the two test configurations of section 3.2. At first, the results of the classical hydrodynamic coupling approach (cf. section 3.3.1) are shown, then the thermodynamic coupling scheme for the pure compression (cf. section 3.3.2) is applied to the corresponding test case. Finally, the first test case configuration is calculated

using the MPV coupling approach that accounts for thermodynamic and hydrodynamic effects (cf. section 3.3.3).
For the computations, the numerical framework described in section 4.8.1 is employed. This framework is applied to the test cases in two different versions. At first, the original fully compressible two-phase flow solver is used to simulate the test cases and to create a reference solution for the compressible flow domains (cf. Fig. 4.8). Then, a second computation is performed using the coupling algorithms to simulate the zero Mach number region (cf. Fig. 4.9). As it has already been detailed in section 3, the exact solution of the one-dimensional zero Mach number Euler equations is used to describe the $M = 0$ regions and the coupling to the adjacent compressible flow region is established by an iterative procedure requiring the equality of pressure and velocity across the interface. Finally, the coupling algorithms provide the numerical flux terms for the compressible flow solver at the interface.
A comparison of the different coupling schemes and the ghost fluid method with respect to the computational effort is strongly problem dependent. For example, the simple purely thermodynamic coupling scheme that is based on the analytical solution performed about 10% faster than the ghost fluid method for the considered test cases. But, this situation changes according to the size of the zero Mach number domain. The present work is focused on the coupling in the simple one-dimensional context. For practical applications in two and three space dimensions, the analytical solution in the incompressible domain has to be replaced by a standard incompressible solver. In this case a considerable reduction of the computational effort would be expected using the coupling schemes for problems characterized by a great difference of the sound speeds and a large incompressible domain.
The numerical studies for the following test cases have originally been performed in the context of [42].

5.1.1.1. Hydrodynamic coupling

In this section, the computational results of the hydrodynamic coupling approach presented in section 3.3.1 are discussed. The algorithm couples the pressure of the compressible region to the hydrodynamic pressure $p^{(2)}$ of the incompressible domain. In order to assess the pure hydrodynamic coupling, the test case of section 3.2.1 is used. The whole flow region is initially at rest and a pressure difference is prescribed that accelerates the incompressible region. The initial conditions for the different flow regions are given in Fig. 5.1. The incompressible domain ($0.4 < x < 0.6$) is treated analytically by the cou-

pling scheme following the procedure of section 3.3.1. The parameters for the numerical scheme are chosen as follows.

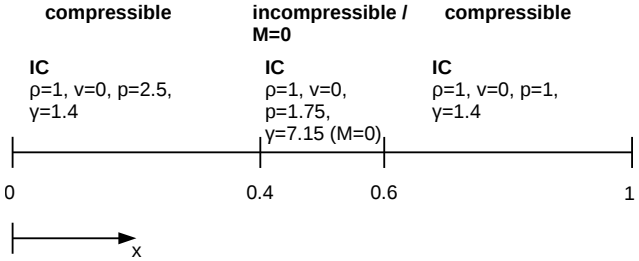

Figure 5.1.: Setup for the hydrodynamic acceleration of an incompressible region: initial conditions (IC).

	L_∞ norm	L_2 norm
Density ρ	$2.39 \cdot 10^{-2}$	$1.54 \cdot 10^{-3}$
Velocity v	$4.39 \cdot 10^{-2}$	$2.91 \cdot 10^{-3}$
Pressure p	$7.45 \cdot 10^{-2}$	$4.99 \cdot 10^{-3}$

Table 5.1.: Hydrodynamic test case: L_∞ and L_2 norm comparison of the results of the hydrodynamic coupling and the ghost fluid type scheme.

A second order DG approach in combination with a grid size of $\Delta x = 0.025$ is used. The time step is equal to $\Delta t = 5 \cdot 10^{-5}$ and the calculation is stopped at the time $t_{end} = 0.065$. With the help of the compressible ghost fluid method, a reference solution is created using the Tait equation of state for the incompressible region. This means that without applying the coupling algorithms, the whole domain $0 \leq x \leq 1$ depicted in Fig. 5.1 is discretized and solved numerically by the compressible two-phase flow solver as described in section 4.8.1 and displayed in Fig. 4.8. The incompressible flow region $0.4 \leq x \leq 0.6$ has also to be discretized and simulated. It is treated as weakly compressible and the Tait equation of state is applied in this region. The parameters of the

Tait equation of state are chosen as $p_0 = 1.75$, $\rho_0 = 1.0$ and $k_0 = 3310$. The coupling of the different flow domains is handled by the two-phase approach of the numerical framework.

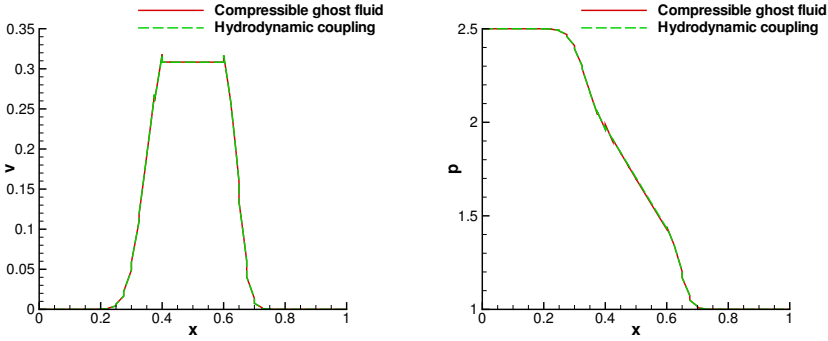

Figure 5.2.: Velocity and pressure plot for the hydrodynamic coupling of a compressible (perfect gas) and an incompressible (weakly compressible Tait fluid for reference solution) region at $t = 0.065$. Comparison of the hydrodynamic coupling procedure and the ghost fluid type method.

The higher pressure at the left causes an acceleration of the incompressible region. As a consequence, the compressible fluid at the right is compressed, while there is an expansion traveling through the left compressible region. This is evident from the velocity and pressure plots in Fig. 5.2, where the compression and expansion wave can be seen. The results of the hydrodynamic coupling method and the ghost fluid approach are matching excellently, as can be seen in Fig. 5.2. A closer look at the plots shows discontinuities in the solution that are due to the direct visualization of the DG polynomials that are discontinuous across cell borders. Only minor deviations are visible from the comparison of the reference solution to the results of the coupling scheme for the flow variables in the compressible region in terms of the L_∞ and L_2 norms. The corresponding norms are summarized in Tab. 5.1.
Using the hydrodynamic coupling approach, the behavior of the compressible flow can therefore be modeled in accordance with the ghost fluid method with-

out being forced to resolve the pressure waves inside the incompressible region. Therefore, the time step restrictions are less severe which leads to a faster computation.

5.1.1.2. Thermodynamic coupling

In the following, the results of the thermodynamic coupling algorithm of section 3.3.2 are presented. The compressible pressure is coupled to the spatially constant background pressure $p^{(0)}$ of the zero Mach number region. Two different configurations of the test case of section 3.2.2 are investigated with different equations of state for the $M = 0$ fluid. In both cases, a sound wave is traveling through a compressible gas. It finally hits the boundary between the compressible region and a zero Mach number domain consisting of a gas in the first and of a liquid in the second case. The interface between the two fluids is supposed to be steady, as the acoustic wave is weak and therefore only causes low interface velocities.

Coupling a compressible perfect gas to an incompressible ($M \to 0$) perfect gas region

In order to demonstrate the explicit coupling mechanism, an acoustic wave traveling through a compressible perfect gas and impinging on a zero Mach number perfect gas region is investigated. The setup of the test case has been introduced in section 3.2.2 and is depicted in Fig. 5.3 including its initial and boundary conditions.

At the left boundary $x = 0$ the acoustic wave is generated by a time dependent sinusoidal velocity boundary condition

$$v(x = 0, t) = 0.01 \sin(18t). \tag{5.1}$$

At the right boundary $x = 1.1$ the domain is supposed to be bounded by a reflecting wall, according to the assumption of a symmetric compression. This enforces the velocity to be zero $v(x = 1.1, t) = 0$ at all times. The initial conditions in the compressible region are chosen to equal

$$(\rho, v, p) = \quad (1, 0, 1)\,, \quad 0 < x \leq 1. \tag{5.2}$$

Applying the solution of the iterative coupling procedure as a boundary condition at the interface $x = 1$, the domain $1 < x \leq 1.1$ is not discretized for numerical simulation.

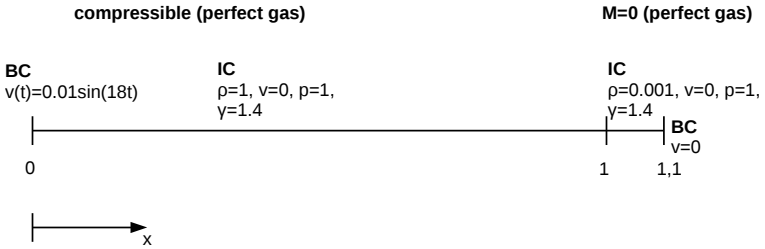

Figure 5.3.: Setup for the radially symmetric compression: Initial conditions (IC) and boundary conditions (BC) for the coupling of a compressible perfect gas and a zero Mach number perfect gas region.

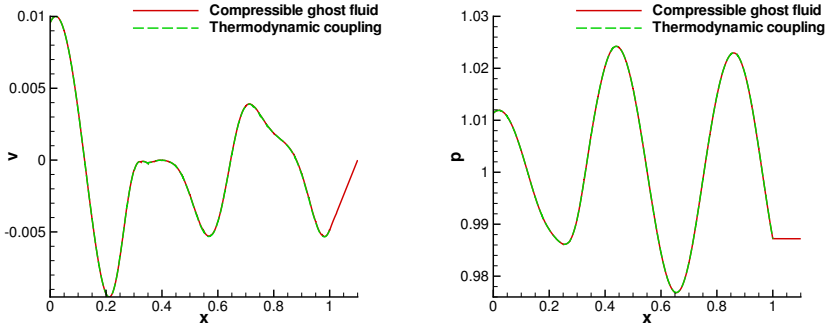

Figure 5.4.: Velocity and pressure plot for the thermodynamic coupling of a compressible and a zero Mach number region (perfect gas respectively) at $t = 1.5$. Comparison of the thermodynamic coupling procedure and the ghost fluid type method.

In order to compare the results obtained with the coupling mechanism, a second computation is provided that is based on the ghost fluid type scheme. In this case, the complete domain $0 \leq x \leq 1.1$ is discretized and the incompressible regime is approached by a weakly compressible fluid (cf. Fig. 4.8). This is the

reason why the density in the region $1 < x \leq 1.1$ is chosen to $\rho = 10^{-3}$ in order to augment the speed of sound in this domain, approximating a $M = 0$ behavior.
For the simulations, the grid resolution has been chosen to $\Delta x = 0.025$, the time step size has been fixed to $\Delta t = 10^{-4}$ and the computation ends at $t_{end} = 1.5$. Furthermore, a third order DG scheme has been used.
Figure 5.4 illustrates the results for velocity and pressure that are obtained by the iterative coupling procedure and the ghost fluid type method. As is obvious from the two plots, there are only minor differences as the curves are nearly identical. Concerning the $M = 0$ region, only the computed solution of the ghost fluid type scheme is shown indicating the expected linear velocity distribution as well as a constant pressure. For the compressible flow region, a

	L_∞ norm	L_2 norm
Density ρ	$1.54 \cdot 10^{-2}$	$6.49 \cdot 10^{-4}$
Velocity v	$1.83 \cdot 10^{-2}$	$7.76 \cdot 10^{-4}$
Pressure p	$2.15 \cdot 10^{-3}$	$9.09 \cdot 10^{-4}$

Table 5.2.: Pure compression (two perfect gases): L_∞ and L_2 norm comparison of the results of the thermodynamic coupling and the ghost fluid type scheme.

direct comparison of the coupling scheme and the ghost fluid method has been performed by the calculation of the L_∞ and L_2 norm for density, velocity and pressure. The corresponding norms are listed in Tab. 5.2. It is evident that the differences between the two schemes are small.

Coupling a compressible perfect gas to an incompressible ($M \to 0$) Tait fluid region

As a second configuration, a compressible perfect gas region and a $M = 0$ region being occupied by a fluid obeying the Tait equation of state (e.g. water) are considered. For the setting of the test case the same domain decomposition as in the previous case is used, yet with different initial conditions that are given in Fig. 5.5.
At the left boundary $x = 0$, the velocity boundary condition of equation (5.1) is applied. According to the previous simulations a grid spacing of $\Delta x = 0.025$ is

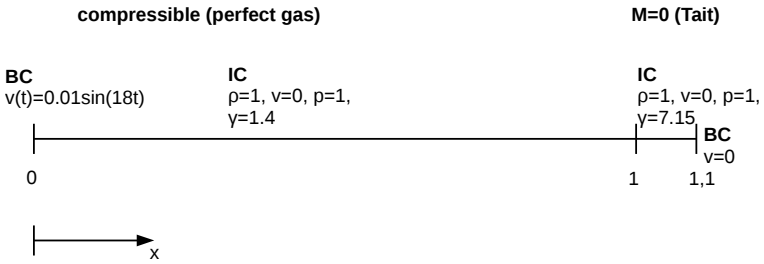

Figure 5.5.: Setup for the radially symmetric compression: Initial conditions (IC) and boundary conditions (BC) for the coupling of a compressible perfect gas and an incompressible Tait fluid region.

used, the time step is $\Delta t = 10^{-4}$ and the computation is stopped at $t_{end} = 1.5$. The third order DG scheme is applied and the parameters k_0 and p_0 of the Tait equation of state are chosen as $k_0 = 300$ and $p_0 = 1$.
The results of this coupling are presented in Fig. 5.6. As in the previous case,

	L_∞ norm	L_2 norm
Density ρ	$3.2 \cdot 10^{-3}$	$1.46 \cdot 10^{-4}$
Velocity v	$3.8 \cdot 10^{-3}$	$1.73 \cdot 10^{-4}$
Pressure p	$4.5 \cdot 10^{-3}$	$2.04 \cdot 10^{-4}$

Table 5.3.: Pure compression (perfect gas and Tait fluid): L_∞ and L_2 norm comparison of the results of the thermodynamic coupling and the ghost fluid type scheme.

the velocity and pressure plots for the compressible flow region resemble each other quite well. This is confirmed by the comparison of the curves by L_∞ and L_2 norm in Tab. 5.3.
Having a look at the velocity plot in Fig. 5.6, it is evident that the slope of the velocity in the $M = 0$ region is less steep in comparison to the perfect gas case of Fig. 5.4, whereas the velocity is still not constant but varies linearly from $v(x = 1.0) \neq 0$ to $v(x = 1.1) = 0$.

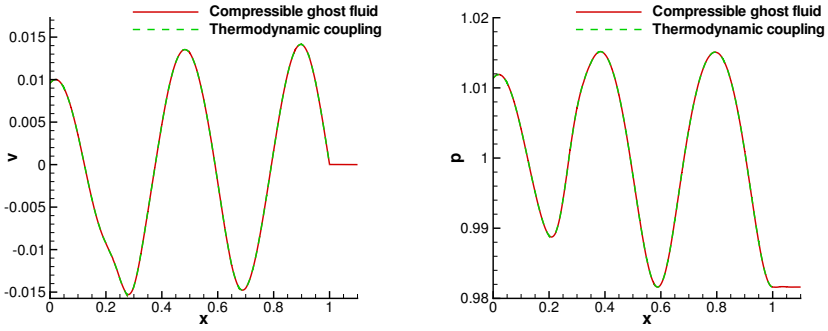

Figure 5.6.: Velocity and pressure plot for the thermodynamic coupling of a compressible (perfect gas) and a zero Mach number (Tait fluid) region at $t = 1.5$. Comparison of the thermodynamic coupling procedure and the ghost fluid type method.

5.1.1.3. Multiple pressure variables (MPV) coupling

The last coupling method deals with the coupling of the compressible pressure to a combination of the spatially constant background pressure $p^{(0)}$ and the hydrodynamic pressure $p^{(2)}$ of the zero Mach number region. This combines thermodynamic and hydrodynamic effects.
The MPV coupling of section 3.3.3 is applied to the test case introduced in section 3.2.1, whose setup is depicted in Fig. 5.1. Again, an initial pressure difference accelerates the $M \to 0$ region. Yet, this time a compression of the domain is possible due to the fact that thermodynamic effects are taken into account and that the velocity has no longer to be divergence-free.
By adding compressibility effects to the coupling scheme, an appropriate initial value for the background pressure $p^{(0)}$ has to be chosen. As already mentioned in section 3.3.3, our initial choice for the background pressure $p^{(0)}$ is the arithmetic mean of the surrounding pressures (cf. equation (3.16)). This leads to an initial pressure $p^{(0)} = 1.75$ in the present case.
The numerical setup is identical to the one of the previous calculations for the hydrodynamic coupling method in section 5.1.1.1. Again the second order DG scheme together with a grid spacing of $\Delta x = 0.025$ is used. The time

step is equal to $\Delta t = 5 \cdot 10^{-5}$ and the calculation is also stopped at the time $t_{end} = 0.065$. The same reference solution of the ghost fluid method is employed as for the comparison with the pure hydrodynamic coupling in the previous section (cf. Fig. 5.2) where the Tait equation of state is applied to the weakly compressible region of the ghost fluid approach with the following parameters: $p_0 = 1.75$, $\rho_0 = 1.0$ and $k_0 = 3310$. With respect to the computation with the coupling scheme, the present MPV approach takes into account compressible effects for the previously incompressible domain ($0.4 < x < 0.6$). Therefore, an equation of state is needed and the Tait equation of state with the above parameters is also employed for the zero Mach number region by the MPV coupling scheme.
The comparison between the ghost fluid method and the MPV coupling is displayed in Fig. 5.7. A first look at the plots reveals that both approaches

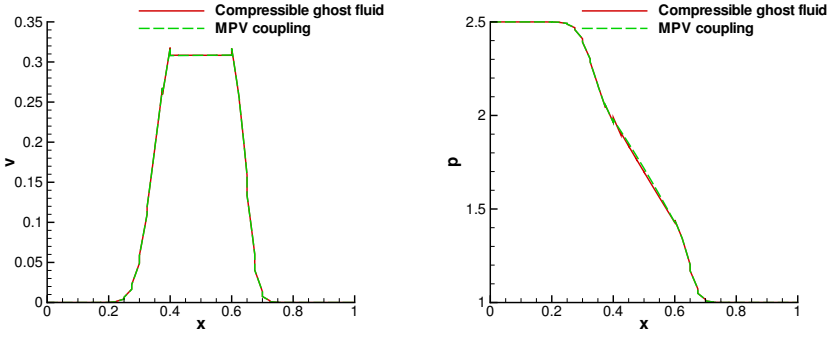

Figure 5.7.: Velocity and pressure plot for the combined thermodynamic and hydrodynamic coupling of a compressible (perfect gas) and a $M = 0$ (Tait fluid) region at $t = 0.065$. Comparison of the MPV coupling procedure and the ghost fluid type method.

are in a good agreement to each other in the compressible flow regions. This is confirmed in a quantitative way by comparing the results of the coupling scheme to the ones of the ghost fluid method in terms of the L_∞ and L_2 norms for the flow variables in the compressible flow region. The norms can be found in Tab. 5.4.

	L_∞ norm	L_2 norm
Density ρ	$2.26 \cdot 10^{-2}$	$1.44 \cdot 10^{-3}$
Velocity v	$4.23 \cdot 10^{-2}$	$2.80 \cdot 10^{-3}$
Pressure p	$7.19 \cdot 10^{-2}$	$4.83 \cdot 10^{-3}$

Table 5.4.: Hydrodynamic acceleration: L_∞ and L_2 norm comparison of the results of the MPV coupling and the ghost fluid type scheme.

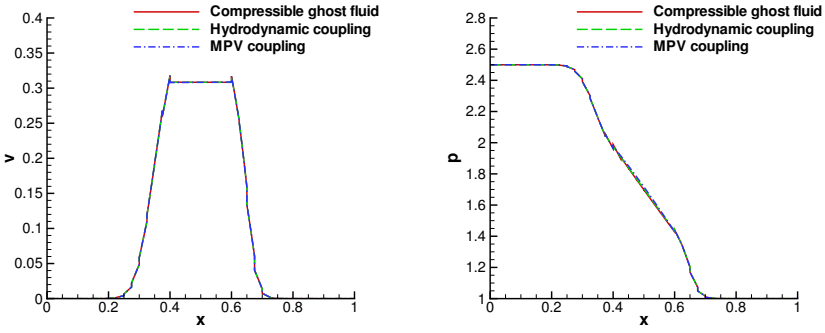

Figure 5.8.: Velocity and pressure plot for the coupling of a compressible (perfect gas) and a $M = 0$ (Tait fluid) region at $t = 0.065$. Comparison of the pure hydrodynamic coupling, the MPV coupling approach and the ghost fluid method.

The results of the pure hydrodynamic coupling and the MPV coupling approach can now directly be compared to each other and to the reference solution. A first qualitative impression is provided by the velocity and pressure plots of Fig. 5.8. It is barely possible to distinguish the three curves in the compressible flow domains. The only visible differences concern the zero Mach number region, where small deviations are present. Yet, as the main interest is in the solution of the compressible flow region, both coupling approaches are directly compared in a more quantitative way in this region.

A brief look at Tab. 5.1 and Tab. 5.4 shows that the MPV coupling approach is always closer to the reference solution that is the same for both coupling approaches. In a second step, the norms of both coupling schemes can be compared and the deviation of the pure hydrodynamic coupling from the norms of the MPV coupling is determined. This is done in Tab. 5.5, where the relative deviation is given. It is obvious that the MPV coupling approach is about 3% to 6% closer to the reference solution for the compressible flow region than the pure hydrodynamic coupling approach. This indicates that the fully compressible solution is clearly approached with the MPV coupling and that even for this test case, dominated by hydrodynamics, it is favorable to include the thermodynamic background pressure.

	L_∞ norm	L_2 norm
Density ρ	+5.6%	+6.6%
Velocity v	+3.9%	+4.0%
Pressure p	+3.6%	+3.4%

Table 5.5.: Hydrodynamic acceleration: Deviation of the L_∞ and L_2 norm of the pure hydrodynamic coupling from the corresponding norms of the MPV coupling.

5.1.1.4. Conclusions

Three different coupling schemes have been applied to the test cases of section 3.2. The methods differ in the way they couple the pressure of the compressible flow region to the incompressible region where the pressure is split into a hydrodynamic and a thermodynamic pressure. While the pressure of the compressible region is coupled to either the hydrodynamic or the thermodynamic pressure for the first two approaches, a third coupling scheme is based on the coupling of the hydrodynamic and the thermodynamic pressure of the zero Mach number region to the pressure of the surrounding compressible flow (MPV approach). Jump conditions across the interface are used to finally control the iteration process that is based on the solution of a half-Riemann problem on the compressible side and the exact solution of the Euler equations in the zero Mach number domain. At the compressible-incompressible interface, each of the coupling algorithms provides the numerical fluxes as a

boundary condition for the compressible flow solver.

The purely thermodynamic coupling is validated with a test case characterized by compressible effects originating from the compression of the zero Mach number region boundaries. A second test case describes the acceleration of an incompressible domain due to a pressure gradient and it is used to assess the hydrodynamic coupling as well as the combined hydrodynamic and thermodynamic coupling approach. For all test cases, the results of the compressible flow domain have been compared to those of a compressible two-phase flow sharp interface method and an excellent agreement can be observed. Moreover, the direct comparison of the hydrodynamic approach and the MPV coupling, that combines hydrodynamic and thermodynamic effects, shows that the results of the MPV coupling are slightly closer to the fully compressible solver than those of the purely hydrodynamic approach that neglects compressible effects.

5.1.2. Validation of the MPV scheme for single-phase problems

The focus is now on the pressure-based MPV scheme. It is assessed to one-dimensional compressible single-phase flows and proves to accurately handle standard shock tube problems. Moreover, a comparison between the conservative and the semi-conservative MPV method is performed.

5.1.2.1. Sod test case

The classical test cases for the assessment of compressible flow solvers in one space dimension are shock tube problems, where a Riemann problem is solved. For these examples, analytical solutions exist and the numerical scheme can directly be assessed with respect to its capability to properly resolve expansion fans, contact discontinuities and shock waves. A variety of well established test cases exists described in the literature and a good overview is given by Toro [60].
One of them is the following example that is known as Sod's shock tube [61] whose initial conditions are given by

$$\begin{pmatrix} \rho_L \\ v_L \\ p_L \\ \gamma_L \end{pmatrix} = \begin{pmatrix} 1.0 \\ 0 \\ 1 \\ 1.4 \end{pmatrix}; x < 0.5 \qquad \begin{pmatrix} \rho_R \\ v_R \\ p_R \\ \gamma_R \end{pmatrix} = \begin{pmatrix} 0.125 \\ 0 \\ 0.1 \\ 1.4 \end{pmatrix}; x > 0.5. \tag{5.3}$$

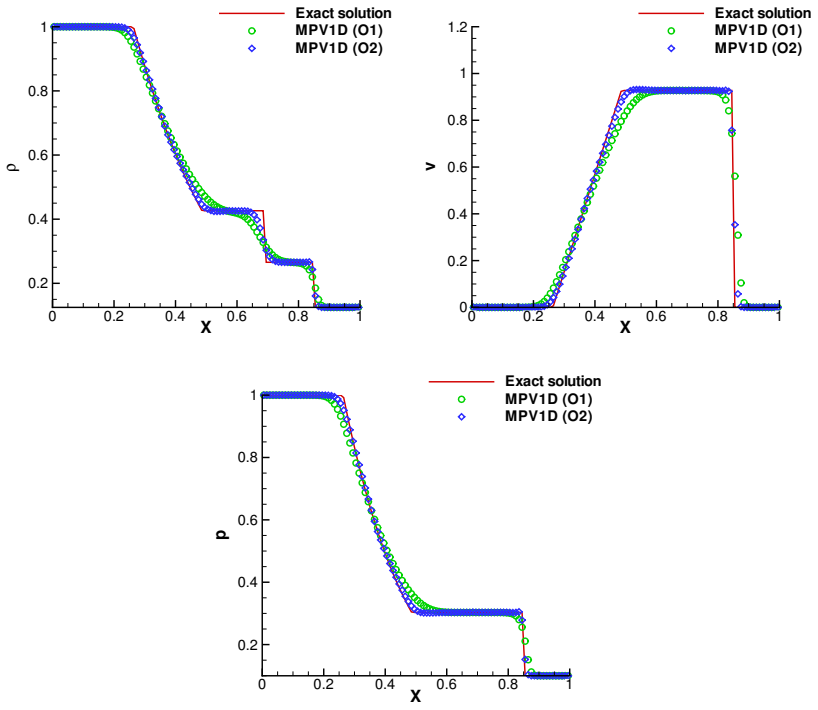

Figure 5.9.: Sod test case: density, velocity and pressure plot of the MPV simulation (first (O1) and second (O2) order, 100 grid cells) and the exact solution at $t = 0.2$.

The test case has been computed with the first and the second order MPV method on a grid of 100 cells. It can be seen from Fig. 5.9 that the MPV approach is able to resolve the wave structure of the problem that consists of a left running expansion fan, a contact discontinuity and a shock that moves to the right. The numerical solution is in good agreement with the exact solution. Moreover, the differences between the first and the second order scheme are

evident. The second order approach generates an improved numerical solution as it approaches the exact solution more precisely and shows a better shock resolution. It resolves the shock wave within three grid cells while the first order approach needs five cells for the approximation. Additionally, the contact discontinuity is less smeared and resolved more accurately. For the second order calculation, the RK2CN time discretization has been used and the spatial reconstruction has been carried out with the minmod slope limiter.

5.1.2.2. Sod test case with the semi-conservative MPV approach

In the following, the semi-conservative MPV approach (cf. Sec. 4.5) is applied to the shock tube test case of Sod [61]

$$\begin{pmatrix} \rho_L \\ v_L \\ p_L \\ \gamma_L \end{pmatrix} = \begin{pmatrix} 1.0 \\ 0 \\ 1 \\ 1.4 \end{pmatrix}; x < 0.5 \qquad \begin{pmatrix} \rho_R \\ v_R \\ p_R \\ \gamma_R \end{pmatrix} = \begin{pmatrix} 0.125 \\ 0 \\ 0.1 \\ 1.4 \end{pmatrix}; x > 0.5. \tag{5.4}$$

The standard single-phase test case is calculated with the MPV method in semi-conservative formulation and compared to the results of the conservative scheme in Fig. 5.10. For both numerical approaches a first order spatial and temporal discretization is applied and the computation has been carried out on a mesh with 100 grid cells. The results of the two schemes are close to the exact solution. However, differences are visible with respect to the resolution of the contact discontinuity and the shock wave. The density plot reveals that the two approaches predict slightly different shock locations and also strengths. Due to the use of the non-conservative pressure equation, the semi-conservative approach has difficulties to capture the shock accurately.
This is even more evident from Fig. 5.11 that shows the results of both schemes on a finer grid using 1000 grid cells for the spatial discretization. It can be seen that while the conservative MPV method converges to the exact solution, the semi-conservative method is deviating from the analytical solution. The shock position and strength are slightly mispredicted as is obvious from the close-up view in Fig. 5.11.

5.1.2.3. Sod test case for a covolume gas using the semi-conservative MPV approach

The advantage of the semi-conservative approach is that it can easily be applied to arbitrary equations of state as long as the speed of sound can be evaluated.

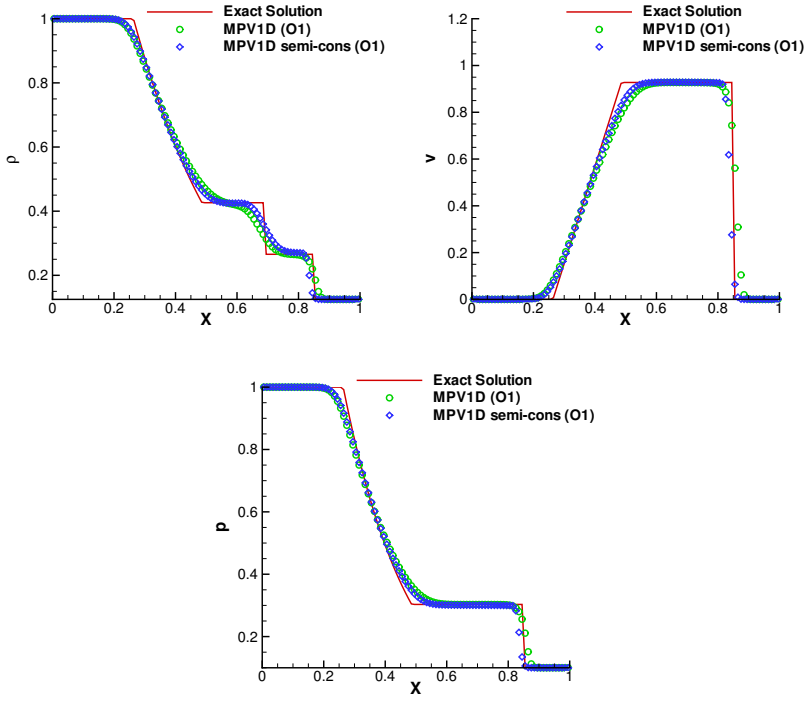

Figure 5.10.: Sod test case: density, velocity and pressure plot of the MPV simulation in semi-conservative and conservative formulation (first order (O1), 100 grid cells) and the exact solution at $t = 0.2$.

To demonstrate this property, the shock tube test case of Sod is modified, replacing the perfect gas by a covolume gas.

The covolume equation of state is a simple generalization of the perfect gas

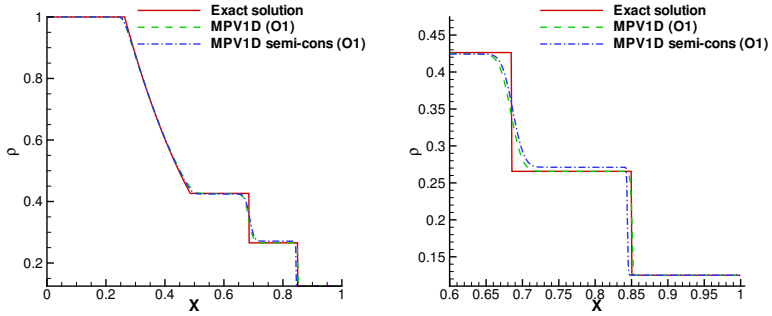

Figure 5.11.: Sod test case: density plot of the MPV simulation in conservative and semi-conservative formulation (first order (O1), 1000 grid cells) and the exact solution at $t = 0.2$. At the right: close-up view at the location of shock and contact discontinuity.

equation of state (2.5)

$$p = \frac{\gamma - 1}{1 - b\rho}(e - \frac{\rho}{2}|\vec{v}|^2). \tag{5.5}$$

According to [60], the parameter b takes into account the covolume of the gas that is occupied by the molecules themselves and for $b \to 0$ the perfect gas equation of state (2.5) is obtained. For the following computation the covolume b is chosen as a constant.
The pressure Poisson equation (4.59) for the semi-conservative scheme has the speed of sound as the only link to the fluid equation of state. Therefore, equation (5.5) is not needed directly but only to derive the relation for the speed of sound that can be easily computed from the following equation (cf. [60])

$$c = \sqrt{\frac{\gamma p}{(1 - b\rho)\rho}}. \tag{5.6}$$

The numerical test case for the covolume gas is performed with the initial setup of the Sod shock tube given by equation (5.3) and additionally the covolume b is chosen to be constant and equal to $b = 0.8$. The results of the computation are displayed in Fig. 5.12. The numerical simulation has been performed with the first order scheme and 100 grid cells. A first look reveals that the exact solution

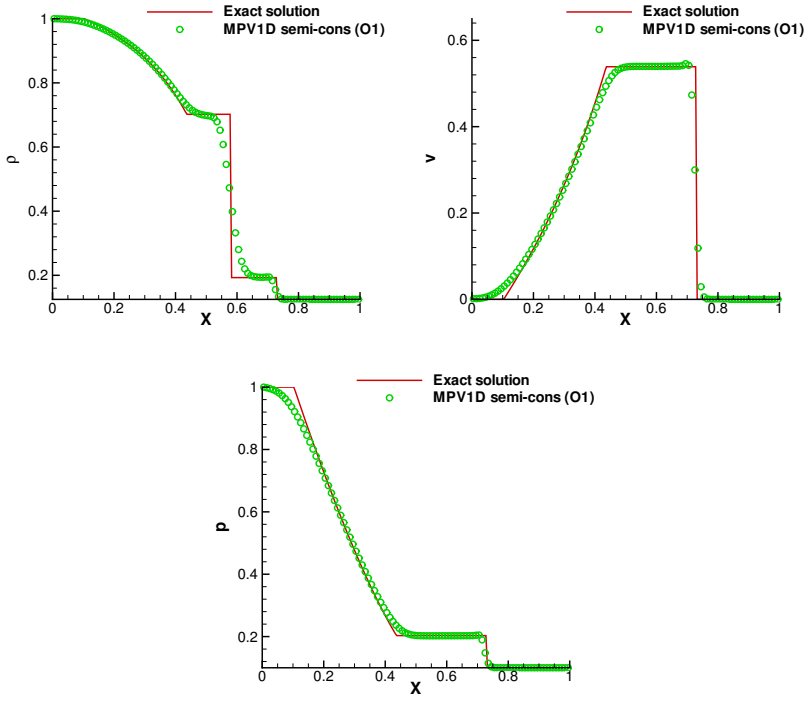

Figure 5.12.: Sod test case for a covolume gas ($b = 0.8$): density, velocity and pressure plot of the MPV simulation in semi-conservative formulation (first order (O1), 100 grid cells) and the exact solution at $t = 0.15$.

of the problem has changed considerably using the covolume gas in comparison to the original shock tube case of Sod (cf. Fig. 5.9). The semi-conservative scheme is able to nicely approach the exact solution of the Riemann problem and has less problems to accurately capture the shock than for the original Sod case. Because of the weaker shock strength and the lower shock speed, the

conservation errors are less pronounced.

5.1.3. Limitations of the MPV method

Subsequently, some numerical examples are shown that confirm the theoretical reasoning of section 4.7 concerning the second order extension of the MPV method and the outlet boundary conditions of the pressure-based scheme on a staggered grid. It is shown that the second order scheme is prone to velocity and pressure oscillations in the presence of large density jumps and that for the outlet boundary conditions the standard finite volume treatment leads to reflections at the domain boundaries.

5.1.3.1. Second order MPV approach in space and time with high density ratios across contact discontinuities

The extension of the MPV method to second order in space and time comes along with the loss of the oscillation-free behavior of the numerical scheme close to density discontinuities, even for single-phase flows. This is illustrated by the following two examples. At first, the transport of a moderate contact discontinuity in density is considered according to Park [62]

$$\begin{pmatrix} \rho_L \\ v_L \\ p_L \\ \gamma_L \end{pmatrix} = \begin{pmatrix} 1.0 \\ 1 \\ 1 \\ 1.4 \end{pmatrix}; x < 0.2 \qquad \begin{pmatrix} \rho_R \\ v_R \\ p_R \\ \gamma_R \end{pmatrix} = \begin{pmatrix} 0.7 \\ 1 \\ 1 \\ 1.4 \end{pmatrix}; x > 0.2. \tag{5.7}$$

The corresponding velocity and pressure plots of the second order MPV scheme are displayed in Fig. 5.13 together with the exact, constant solution. The results clearly show pressure and velocity oscillations. However, a closer look at their scale reveals that the amplitudes are very small. This changes dramatically for larger density ratios, as it is demonstrated subsequently.

Compressible two-phase flows are characterized by dissimilar equations of state that govern the different fluids and that may lead to coupling problems at the interface location, as it has already been discussed in detail. Aside from this effect, there are also the material properties that are jumping considerably. A realistic density ratio is in the order of 1000, as it is the case for water and air for example. Unfortunately, the above presented second order MPV scheme is unable to properly transport such a density jump even for a single-phase flow.

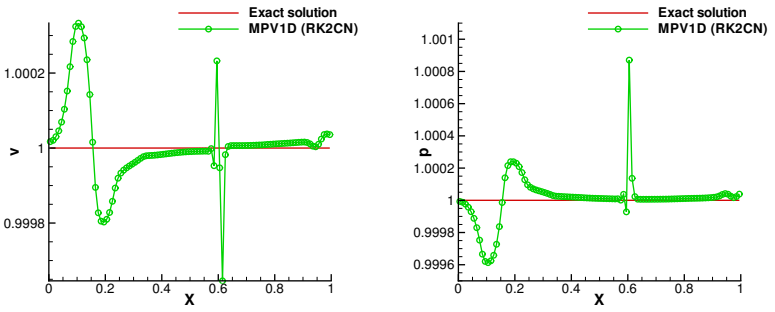

Figure 5.13.: Transport of contact discontinuity in density ($\rho_L = 1$, $\rho_R = 0.7$): velocity and pressure plot of the MPV simulation and the exact solution at $t = 0.4$. The simulation uses 100 grid cells and the second order MPV scheme (RK2CN).

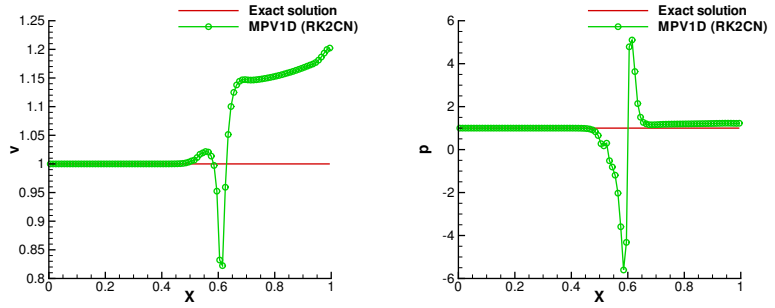

Figure 5.14.: Transport of contact discontinuity in density ($\rho_L = 1000$, $\rho_R = 1$): velocity and pressure plot of the MPV simulation and the exact solution at $t = 0.4$. The simulation uses 100 grid cells and the second order MPV scheme (RK2CN).

This is illustrated by the following setup

$$\begin{pmatrix}\rho_L\\ v_L\\ p_L\\ \gamma_L\end{pmatrix} = \begin{pmatrix}1000\\ 1\\ 1\\ 1.4\end{pmatrix}; x < 0.2 \qquad \begin{pmatrix}\rho_R\\ v_R\\ p_R\\ \gamma_R\end{pmatrix} = \begin{pmatrix}1\\ 1\\ 1\\ 1.4\end{pmatrix}; x > 0.2. \tag{5.8}$$

The scheme now has to deal with a considerable jump in density (three orders of magnitude) and the results are displayed in Fig. 5.14. This time, the oscillations are clearly more pronounced and the pressure has even unphysical negative values. Therefore, the current second order version of the scheme is not able to properly transport such a contact discontinuity with a pressure ratio of 1000.
To remedy this problem, one possibility might be to locally switch to the first order MPV approach at the location of large density gradients, as they are often present in two-phase flows. The first order MPV approach is free of oscillations even in the presence of high density ratios (cf. section 4.6.1). The loss of accuracy may be compensated by locally refining the grid. In the case of two-phase flows, the level set function can act as an indicator to identify cells close to multi-material interfaces with large density gradients.

5.1.3.2. Outlet boundary conditions

For the pressure-based MPV method, the standard finite volume outlet boundary conditions cannot be applied. This has already been discussed in section 4.7.2 and is now proven numerically.
In order to investigate the boundary conditions, the classical Sod test case [61] is used whose initial conditions are given by equation (5.3) and the computation is stopped at $t = 0.5$ when shock and expansion have already reached the domain boundaries. The shock wave travels at supersonic speed while the waves of the expansion fan are subsonic.
Figure 5.15 shows the exact solution and the results of the first order MPV scheme using 200 grid cells. The standard outlet boundary condition using ghost cells (cf. section 4.7.2) is denoted outlet BC and it is evident from all three plots, that there are considerable reflections at the boundaries. In order to further investigate this, a second boundary condition is employed. For this condition, the exact solution of the Riemann problem is written in the ghost cells at each time step and the boundary condition is therefore called exact BC. The plots show a considerable reduction of the reflections by this kind of boundary condition. A closer look at the results reveals that there are still

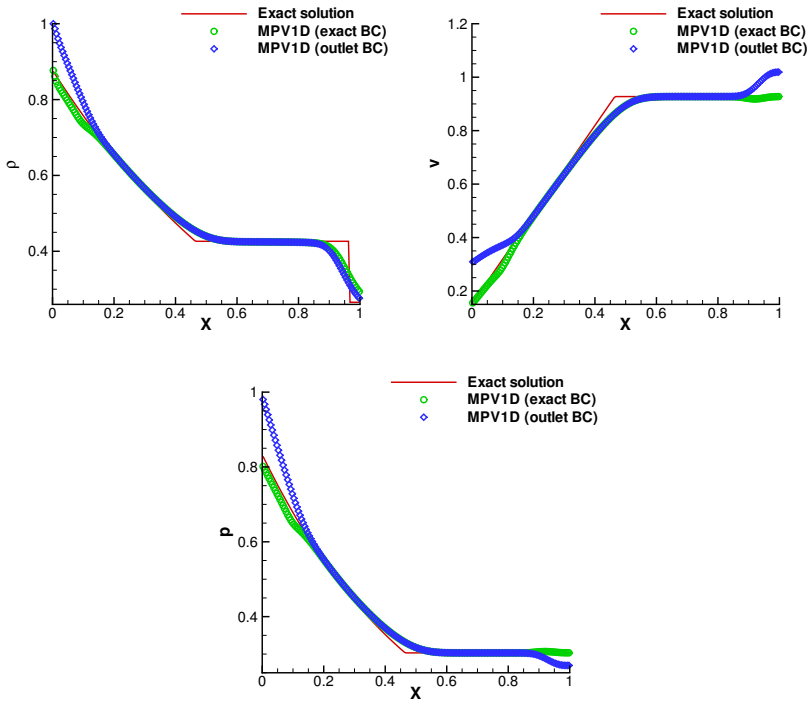

Figure 5.15.: Sod test case: density, velocity and pressure plot of the first order MPV simulation (200 grid cells) with the standard outlet boundary condition (outlet BC) and the exact boundary condition for the Sod test case (exact BC) and the exact solution at $t = 0.5$.

reflected waves, but their magnitude is far smaller than in the case of the standard outlet conditions.

As the exact solution at the boundaries is not available for every numerical simulation, this kind of boundary condition cannot always be applied and an

alternative has to be found in order to attenuate the oscillations on the staggered grid. From the above investigations it is known that the focus has to be on the treatment of the velocity. It is sufficient to use the exact solution of the Riemann problem for the velocity and to simply copy pressure and density to the ghost cells. With these mixed boundary conditions, the same results are obtained as for the exact boundary condition treatment whose results are displayed in Fig. 5.15.

5.1.3.3. Conclusions

These two examples show that there are still open questions to be dealt with. Especially the extension of the numerical approach to second order is of vital interest for the future application of the solver to more realistic and therefore computationally more challenging problems that cannot be treated with the first order scheme.
Because of the above discussed pressure and velocity oscillations, the following one-dimensional investigations of the single-phase MPV scheme are limited to the first order method as the numerical examples include strong density gradients.

5.1.4. Characterization of the MPV scheme regarding the simulation of pressure waves and its shock-capturing properties

In the following, the capability of the conservative MPV method, presented in section 4.4, to correctly simulate the propagation of pressure waves is assessed, as well as its shock-capturing properties. For this purpose, different one-dimensional shock tube test cases from the literature are considered.
In the context of this work, several defects related to the numerical solution of Riemann problems are investigated for the pressure-based MPV approach and a density-based Godunov-type method. The corresponding test cases are well-known and there exist overviews in the literature [63–65]. At first, shock tube problems with large density jumps are examined that pose problems to many numerical schemes [63, 64]. Then, the focus is on the slowly moving shock of Quirk [65] as a second test problem. A very detailed analysis of this phenomenon can be found in [66]. Another well-known test case that causes trouble to many numerical approaches is the 123 problem [67] where strong rarefactions lead to near vacuum conditions. As a last example the wall heating phenomenon [68] is investigated.

For all test cases, the computational results of the pressure-based MPV scheme are compared to those of a density-based finite volume Godunov-type solver (cf. appendix C) and a detailed discussion is presented.

5.1.4.1. Strong rarefactions

In a first step, the shock-capturing properties of the MPV scheme are analyzed. The investigations are mainly based on the work of Kudriakov *et al.* [64] that identified strong rarefaction waves to be the origin of bad shock-capturing behavior.
According to their definition, a strong rarefaction is identified by a large difference in speed of the head and the tail wave of the rarefaction fan that can be measured by the relation r of the wave slopes m

$$r = \left| \frac{m_{Head}}{m_{Tail}} \right|. \tag{5.9}$$

Following the reasoning of [64], the ratio r can be considered to be critical for $r > 10$ and the shock-capturing errors can be explained as follows.
At every time step, an averaging error is introduced at the vicinity of the contact discontinuity. As the boundaries of the rarefaction fan are traveling at very different speeds, the slow tail wave is supposed to stay close to the contact discontinuity for many time steps. Therefore, from the beginning of the computation, the averaging errors accumulate in this region which finally leads to the mispredicted shock wave.
In order to characterize the pressure-based MPV approach, it is applied to a series of shock tube problems with increasing initial density jumps, thus the rarefaction strength is successively raised. The strength is measured by the above proposed wave speed ratio r and additionally the numerical results are compared to those of a standard density-based finite volume solver. Both numerical schemes use a discretization of first order in time and space and the number of grid cells is equal, too. The finite volume solver CFDFV is of Godunov-type (cf. appendix C) and several Riemann solvers are available for the intercell flux calculation. In the following, an exact Riemann solver is employed unless otherwise stated.
The basis for the test series is the standard Sod test case, according to [61] (cf. equation (5.3) for the initial conditions). The corresponding results of the schemes, obtained with 100 grid cells, are displayed in Fig. 5.16. In general, both solvers approximate the exact solution quite well as the strength and the position of all waves are correctly predicted. Yet, a closer look at the velocity

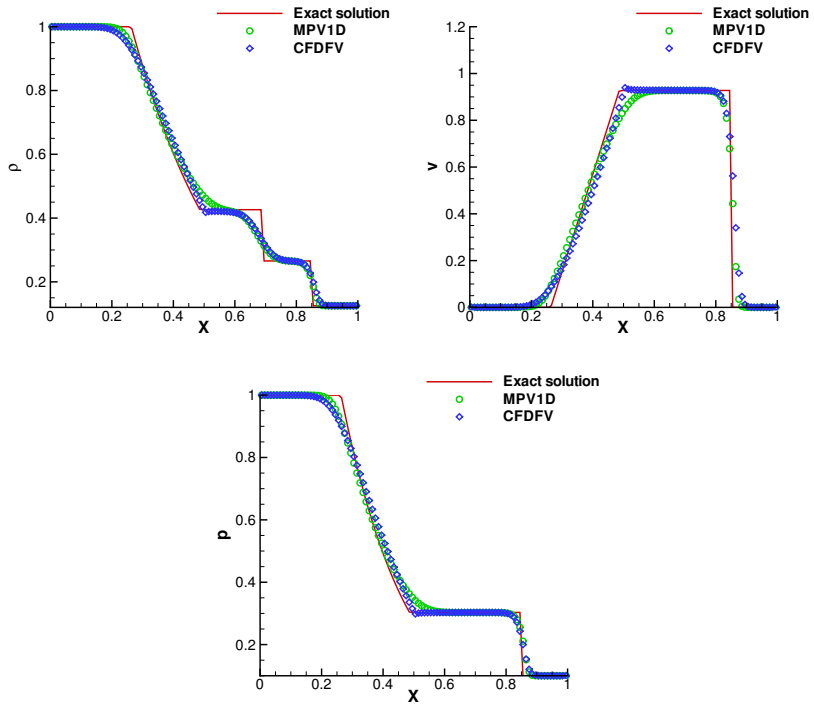

Figure 5.16.: Sod test case: density, velocity and pressure plot of the MPV and the finite volume CFDFV simulation (first order, 100 grid cells) and the exact solution at $t = 0.2$.

plot reveals that the results of the MPV method differ a bit stronger from the exact solution of the rarefaction than those of the finite volume solver. For the Sod test case, the indicator r shows a moderate wave speed ratio

$$r = \left| \frac{m_{Head}}{m_{Tail}} \right| = 2.78. \tag{5.10}$$

In a second step, the initial discontinuity in density is now increased by a factor of 10, augmenting the density ρ_L

$$\begin{pmatrix} \rho_L \\ v_L \\ p_L \\ \gamma_L \end{pmatrix} = \begin{pmatrix} 10.0 \\ 0 \\ 1 \\ 1.4 \end{pmatrix}; x < 0.5 \qquad \begin{pmatrix} \rho_R \\ v_R \\ p_R \\ \gamma_R \end{pmatrix} = \begin{pmatrix} 0.125 \\ 0 \\ 0.1 \\ 1.4 \end{pmatrix}; x > 0.5. \tag{5.11}$$

Due to the raise in the density ratio, the rarefaction wave speed ratio is increased to

$$r = \left| \frac{m_{Head}}{m_{Tail}} \right| = 4.57. \tag{5.12}$$

Since this problem is already more severe compared to the previous one, the spatial resolution has been increased using 300 grid cells to discretize the domain. Both solvers are applied to the modified test case of equation (5.11) and the results can be found in Fig. 5.17. The numerical solution of both schemes is close to the exact one. Again, the MPV approach is inferior to the finite volume approach with respect to the resolution of the expansion fan. Furthermore, the pressure-based method produces a small overshoot at the shock position that is visible in the velocity plot. Being faced with a sonic rarefaction, the solution of the finite volume method contains a jump within the rarefaction fan. This defect is known as entropy glitch [60].
Finally, an even more demanding test is performed by further increasing the density to $\rho_L = 100$, resulting in a density ratio of $\rho_L/\rho_R = 800$

$$\begin{pmatrix} \rho_L \\ v_L \\ p_L \\ \gamma_L \end{pmatrix} = \begin{pmatrix} 100.0 \\ 0 \\ 1 \\ 1.4 \end{pmatrix}; x < 0.5 \qquad \begin{pmatrix} \rho_R \\ v_R \\ p_R \\ \gamma_R \end{pmatrix} = \begin{pmatrix} 0.125 \\ 0 \\ 0.1 \\ 1.4 \end{pmatrix}; x > 0.5. \tag{5.13}$$

Hereby, the indicator r further raises to

$$r = \left| \frac{m_{Head}}{m_{Tail}} \right| = 6.06. \tag{5.14}$$

The outcome of the computations is shown in Fig. 5.18 and as the rarefaction is stronger than the previous one, the plots show that the entropy glitch of the Godunov-type method is more pronounced. This time, the MPV method clearly has trouble to capture the shock since neither its position nor its strength are predicted accurately, as it is obvious from the close-up view of the density in

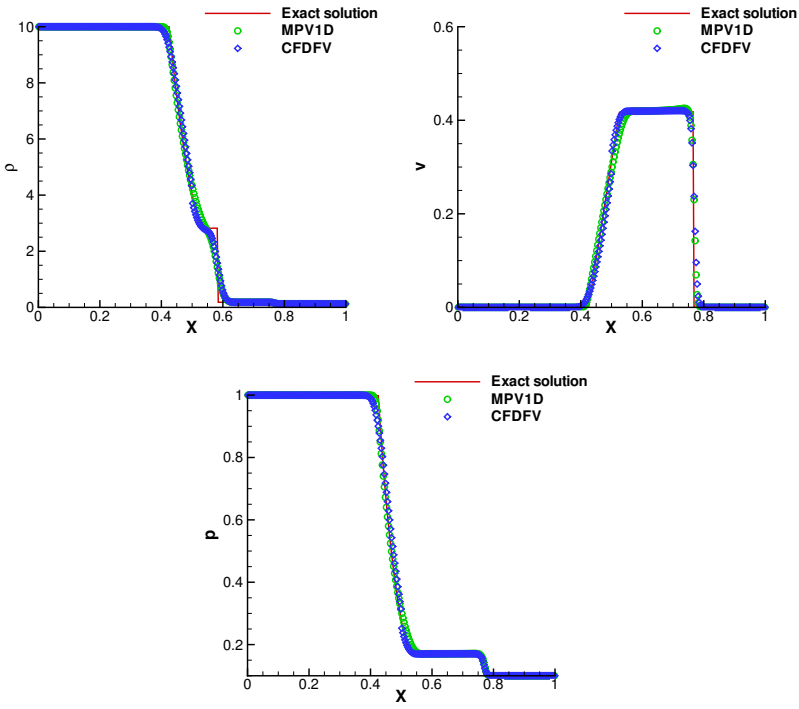

Figure 5.17.: Modified Sod test case (density ratio $\rho_L/\rho_R = 80$): density, velocity and pressure plot of the MPV and the finite volume CFDFV simulation (first order, 300 grid cells) and the exact solution at $t = 0.2$.

Fig. 5.19. While the finite volume scheme still is able to approximate position and strength of the shock, the shock is not accurately captured by the MPV scheme. This is also evident from the velocity plot in Fig. 5.18 and displays the inferiority in shock-capturing of the pressure-based MPV method in comparison to a standard finite volume scheme in the presence of large density ratios.

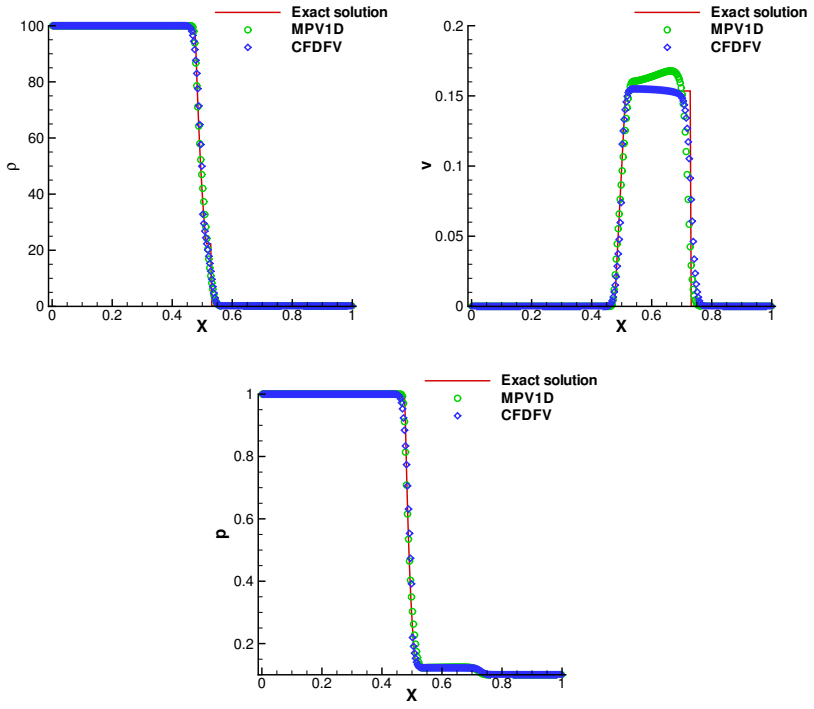

Figure 5.18.: Modified Sod test case (density ratio $\rho_L/\rho_R = 800$): density, velocity and pressure plot of the MPV and the finite volume CFDFV simulation (first order, 300 grid cells) and the exact solution at $t = 0.2$.

To further investigate and confirm this observation, the difference in wave speeds in the rarefaction is drastically increased by not only imposing a high

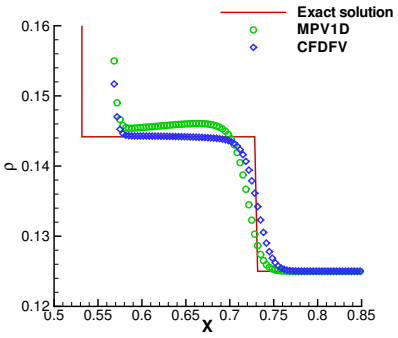

Figure 5.19.: Modified Sod test case (density ratio $\rho_L/\rho_R = 800$):close-up of the density plot of the MPV and the finite volume CFDFV simulation (first order, 300 grid cells) and the exact solution at $t = 0.2$.

initial density ratio but also having a considerable jump in pressure

$$\begin{pmatrix} \rho_L \\ v_L \\ p_L \\ \gamma_L \end{pmatrix} = \begin{pmatrix} 1.0376 \\ 6.0151 \\ 1000 \\ 1.4 \end{pmatrix}; x < 0.7 \qquad \begin{pmatrix} \rho_R \\ v_R \\ p_R \\ \gamma_R \end{pmatrix} = \begin{pmatrix} 0.001 \\ 0 \\ 1 \\ 1.4 \end{pmatrix}; x > 0.7. \tag{5.15}$$

In this case, pressure and density have an initial ratio of about 1000 and 800 grid cells have been used for the first order simulations. The simulation results of the MPV scheme and the finite volume solver are displayed in Fig. 5.20. The velocity distribution already shows that the MPV scheme is considerably deviating from the exact solution. The finite volume code is run with two different flux calculation approaches, an exact Riemann solver and the Lax-Friedrichs method. While the exact Riemann solver is the most accurate way of flux evaluation, the Lax-Friedrichs flux represents a quite simple approximation to the solution of the exact Riemann problem. Thus, the quality of flux evaluation is considerably varied by the use of the two methods.
For this severe test, even the finite volume scheme is unable to accurately capture the shock. This is illustrated by two close-up views on the shock

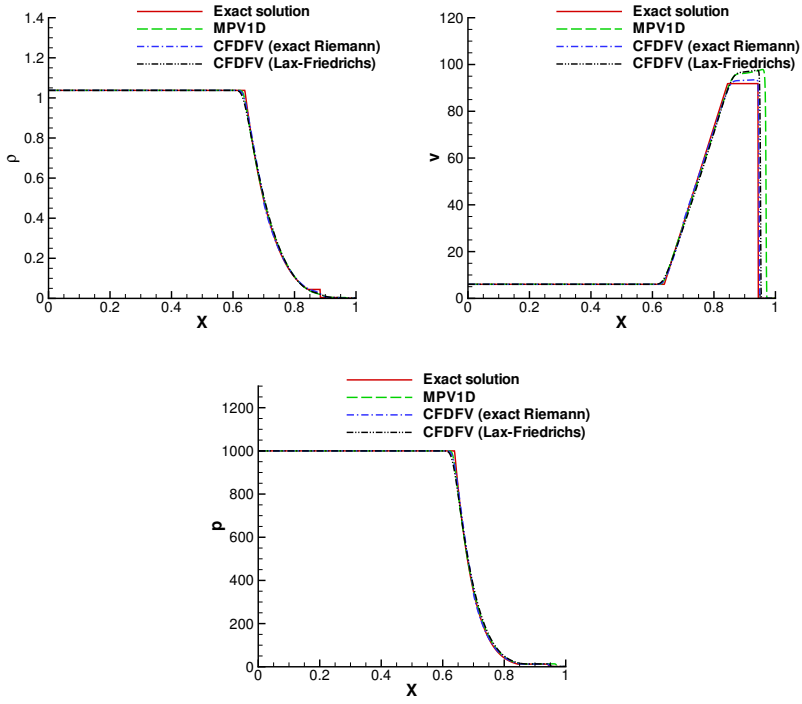

Figure 5.20.: Severe shock tube case (density ratio $\rho_L/\rho_R = 1037.6$, pressure ratio $p_L/p_R = 1000$): density, velocity and pressure plot of the MPV and the finite volume CFDFV simulation (first order, 800 grid cells) and the exact solution at $t = 0.002$.

location for density and velocity, given in Fig. 5.21. The finite volume solver still catches position and strength of the shock quite acceptably using the exact Riemann solver for the numerical flux evaluation, whereas the shock position is mispredicted by the MPV method as is obvious from the density plot. The velocity close-up shows that both solvers differ from the exact solution. When

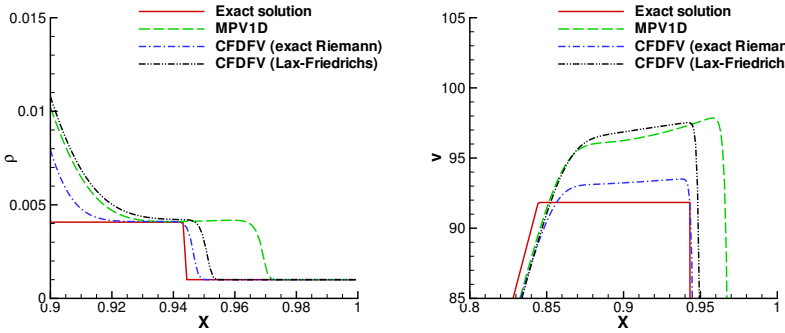

Figure 5.21.: Severe shock tube case (density ratio $\rho_L/\rho_R = 1037.6$, pressure ratio $p_L/p_R = 1000$): close-up views of density (left) and velocity (right) of the MPV and the finite volume CFDFV simulation (first order, 800 grid cells) and the exact solution at $t = 0.002$.

the flux calculation method of the finite volume scheme is changed to the less accurate Lax-Friedrichs flux, the results are tending towards those of the MPV code. This indicates a strong dependency on the quality of the flux calculation. According to [64], the main difficulty for numerical schemes in dealing with strong rarefactions is to minimize the averaging errors over the rarefaction fan at the beginning of the computation. If the numerical scheme has problems to correctly build up the wave pattern, the solution inevitably stays disturbed for the rest of the calculation. This effect can be demonstrated by a test, where the initial solution is not a discontinuity, but the exact solution of the severe shock tube problem with the initial conditions of equation (5.15) at the instant $t = 5 \cdot 10^{-4}$. For this setup, density and velocity plot of the MPV scheme are displayed in Fig. 5.22.
Starting from the developed wave structure, the MPV method is able to further evolve the waves correctly as strength and position of the shock coincide with the exact solution. This illustrates the problems of the pressure-based method to capture the right waves from an initial discontinuity due to the lack of an accurate Riemann solver. Being faced with an initial discontinuity, the waves develop over several time steps during which the problem is not fully resolved

on the computational mesh and physical behavior has to be ensured via the numerical flux calculation.

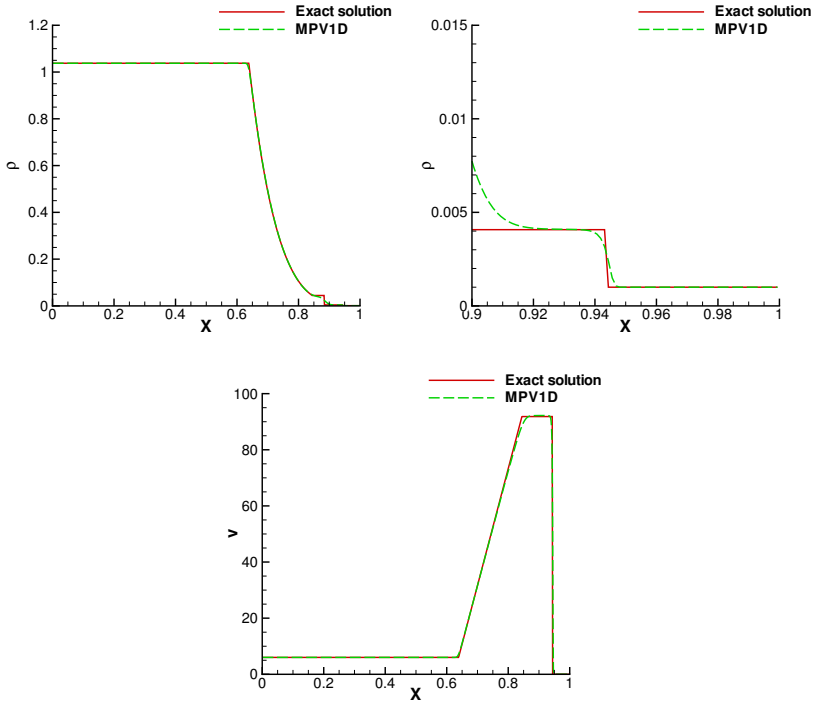

Figure 5.22.: Severe shock tube case (density ratio $\rho_L/\rho_R = 1037.6$, pressure ratio $p_L/p_R = 1000$). The computation is initialized using the exact solution at $t = 5 \cdot 10^{-4}$ that already contains the fully developed wave pattern: density plot (top, left) and close-up on shock location (top, right), velocity plot (bottom). MPV simulation (first order, 800 grid cells) and the exact solution at $t = 0.002$.

In this context, a strong dependency on the quality of the numerical flux can be deduced. While the finite volume scheme with the exact Riemann solver performs soundly, the results are remarkably deteriorating when the flux evaluation is changed to the less accurate Lax-Friedrichs flux (cf. Fig. 5.20). The MPV method uses an upwind method in combination with a central difference discretization for the implicit part. Obviously, this discretization approach further degrades the numerical results in direct comparison to the finite volume approach with the already quite inaccurate Lax-Friedrichs flux. Moreover, the results of Fig. 5.22 indicate that the numerical flux is most important in the beginning of the computation to set up the wave pattern, as the MPV scheme is capable of correctly evolving the shock in time starting from the already existing waves.

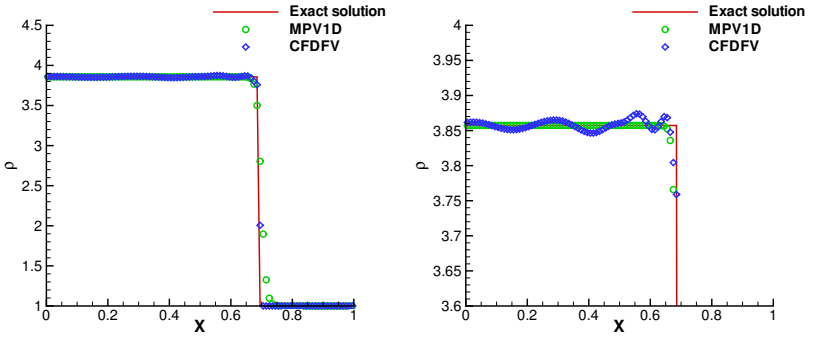

Figure 5.23.: Slowly moving shock: density plot of MPV and finite volume CFDFV simulation at $t = 1.75$ (first order, 100 grid cells, finite volume code with exact Riemann solver); close-up view at the right.

5.1.4.2. Slowly moving shock

As a second example, the movement of a slow shock is investigated with the two numerical schemes. Following Quirk [65] a shock wave is simulated that is slowly moving from left to right. The pre- and post-shock states are given by

the following initial conditions

$$\begin{pmatrix} \rho_L \\ v_L \\ p_L \\ \gamma_L \end{pmatrix} = \begin{pmatrix} 3.86 \\ -0.81 \\ 10.33 \\ 1.4 \end{pmatrix}; x < 0.5 \qquad \begin{pmatrix} \rho_R \\ v_R \\ p_R \\ \gamma_R \end{pmatrix} = \begin{pmatrix} 1.0 \\ -3.44 \\ 1.0 \\ 1.4 \end{pmatrix}; x > 0.5. \tag{5.16}$$

The MPV approach and the density-based finite volume solver CFDFV have been applied to the above initial conditions and the corresponding results are displayed in Fig. 5.23-5.25. For the test, the first order version of both solvers is used on a grid consisting of 100 cells and the simulation is stopped at $t = 1.75$.

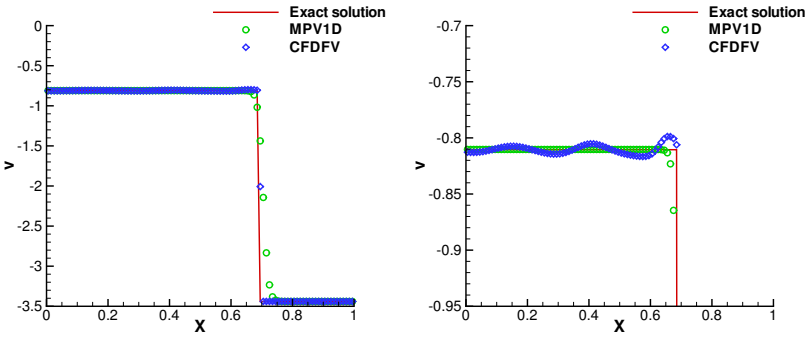

Figure 5.24.: Slowly moving shock: velocity plot of MPV and finite volume CFDFV simulation at $t = 1.75$ (first order, 100 grid cells, finite volume code with exact Riemann solver); close-up view at the right.

A first look at the density plot of Fig. 5.23 already reveals the presence of oscillations behind the right moving shock for the finite volume solver. The plot on the right is a close-up view at the post-shock area. Here, the oscillations of the density-based scheme are clearly visible while the solution of the pressure-based method is free of oscillations. The same is true for the velocity and pressure distributions in Fig. 5.24 and Fig. 5.25. In all cases, the post-shock solution of the finite volume solver is characterized by pronounced oscillations.

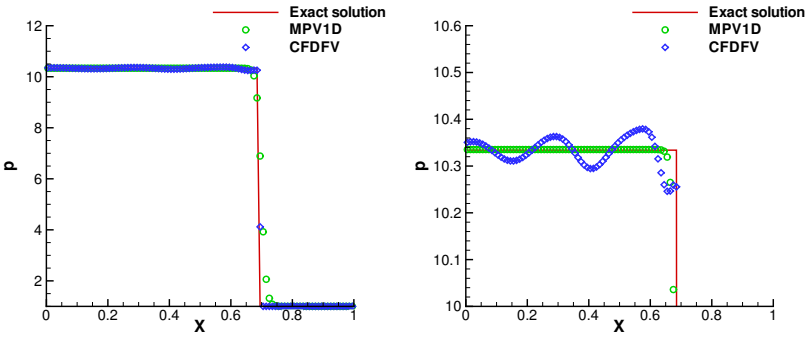

Figure 5.25.: Slowly moving shock: pressure plot of MPV and finite volume CFDFV simulation at $t = 1.75$ (first order, 100 grid cells, finite volume code with exact Riemann solver); close-up view at the right.

With reference to [65] the resolution of a slowly moving shock is a well-known defect of all Godunov-type schemes that can be explained by the fact that they build on the recognition of wave patterns. Hence, spurious waves are introduced that connect the pre- with the post-shock state and that are not present in the physical problem consisting of a single shock wave.
Yet, the pressure-based scheme is not trying to identify certain waves, as it is based on upwind formulae and a central difference discretization. Therefore, the corresponding results are free of oscillations and superior to those of the density-based Godunov-type schemes.
Apart from the Godunov-type methods, there are density-based approaches based on the AUSM (Advection Upstream Splitting Method) flux, introduced by Liou and Steffen [69], that are also able to handle slowly moving shocks without oscillations. The AUSM scheme can be considered to be a combination of Godunov and flux vector splitting approaches. The numerical flux is split in a convective component treated in an upwind manner and a pressure component, using a central difference discretization for the pressure term of the momentum equation. The scheme has continuously been enhanced [70] and its capability to treat slowly moving shocks is proven [71].

5.1.4.3. 123 problem

A third test case is the so-called 123 problem taken from Einfeldt *et al.* [67]. This Riemann problem consists of two strong rarefaction waves, a left and a right moving wave, and a stationary contact discontinuity located between the rarefactions. In the vicinity of the contact discontinuity a very low pressure close to vacuum is created. The density is also low in this flow region, an additional aspect that has to be dealt with numerically. The initial data is given by

$$\begin{pmatrix} \rho_L \\ v_L \\ p_L \\ \gamma_L \end{pmatrix} = \begin{pmatrix} 1.0 \\ -2.0 \\ 0.4 \\ 1.4 \end{pmatrix}; x < 0.5 \qquad \begin{pmatrix} \rho_R \\ v_R \\ p_R \\ \gamma_R \end{pmatrix} = \begin{pmatrix} 1.0 \\ 2.0 \\ 0.4 \\ 1.4 \end{pmatrix}; x > 0.5. \tag{5.17}$$

According to Einfeldt *et al.* [67] this Riemann problem is not linearizable, this means that approximate Riemann solvers may break down when they are applied to this test case.
The 123 problem is solved by the MPV method and the density-based finite volume approach CFDFV using the corresponding first order implementation with 100 grid cells for both solvers. For the finite volume code, the test case is run with an exact Riemann solver and the Lax-Friedrichs method for the flux calculation. The density distribution is displayed in Fig. 5.26. At the first look, the computational results resemble each other and approximate the exact solution. Minor differences can be seen regarding the resolution of the expansion wave fronts. Here, the MPV scheme gives slightly inferior results in comparison to the finite volume solver. Moreover, at the location of the contact discontinuity the differences between the schemes become more obvious and this is shown by the close-up view of Fig. 5.26. In comparison to the exact solution of the density, the finite volume code in combination with the exact Riemann solver predicts density values that are too low. In contrast, the MPV approach is overpredicting the density at the location of the contact discontinuity, but is slightly closer to the density minimum of the exact solution than the finite volume solver. Once the finite volume code is run with the Lax-Friedrichs flux calculation, its behavior in the low density region is similar to that of the MPV approach.
The velocity distribution is shown in Fig. 5.27. Again, the differences between the numerical schemes are small and can only be seen in detail in the close-up view at the location of the contact discontinuity. While the rarefaction waves are traveling to the left and to the right, the velocity is equal to zero

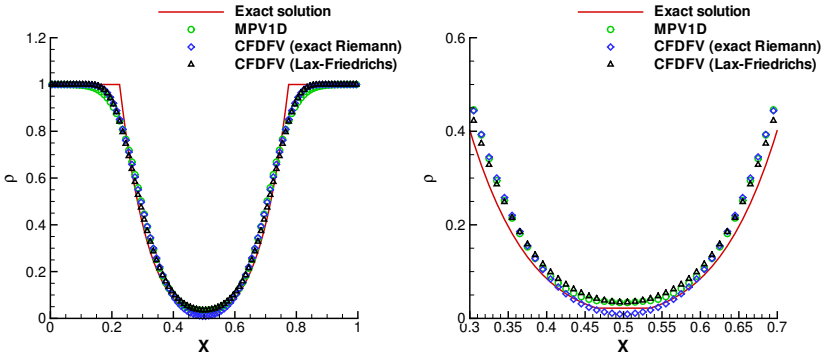

Figure 5.26.: 123 test case: density plot of the MPV and the finite volume simulation at the time $t = 0.1$, including close-up view at the right (first order, 100 grid cells). The finite volume CFDFV code is run with an exact Riemann solver and the Lax-Friedrichs flux.

in the center of the domain as is evident from the exact solution. None of the numerical schemes is able to really reproduce the zero velocity. The finite volume method with the exact Riemann solver is closest to the exact solution, but it also shows slight overshoots in its approximation. The results of the MPV method reveal to be inferior to those of the finite volume approach using the exact Riemann solver. But, in direct comparison to the finite volume method with the Lax-Friedrichs flux, the MPV results prove to be of superior quality.
Figure 5.28 illustrates the numerical results of the pressure distribution. As for the density, it is obvious that the MPV method has problems to correctly capture the front of the expansion waves. Moreover, it is clearly visible that the finite volume method with the exact Riemann solver is quite well approaching the pressure minimum of the exact solution. This is confirmed by the close-up plot, also showing that the MPV method and the finite volume approach in combination with the Lax-Friedrichs flux give comparable results in the low pressure region close to the contact discontinuity. Both methods are not able to correctly capture the minimum of the exact solution.
In general, the MPV method proves to be able to handle low density and low

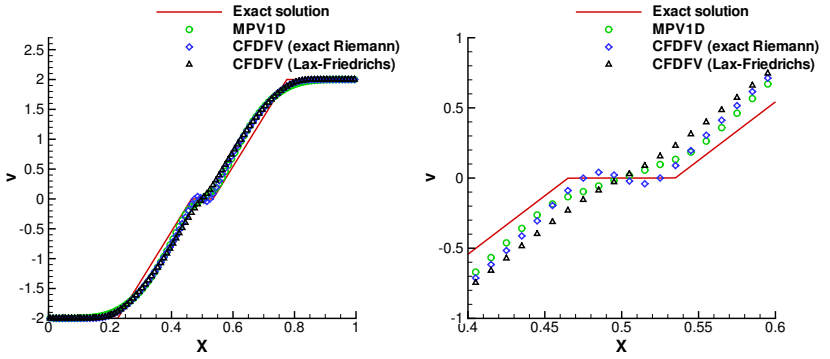

Figure 5.27.: 123 test case: velocity plot of the MPV and the finite volume CFDFV simulation at the time $t = 0.1$, including close-up view at the right (first order, 100 grid cells). The finite volume CFDFV solver is run with an exact Riemann solver and the Lax-Friedrichs flux.

pressure flows as they occur in this test case. This is not necessarily true for any flux calculation method in the finite volume context. The very popular approximate Riemann solver of Roe [72] is not able to compute this test case and a detailed analysis concerning this defect can be found in [67].
As for the strong rarefaction case, it can be seen that the use of an exact Riemann solver in the context of a finite volume approach improves the numerical results. Starting a computation from a discontinuity, the exact Riemann solver is able to introduce the wave patterns even if they cannot yet be resolved by the computational mesh in the beginning. Once the less accurate Lax-Friedrichs flux is used for the finite volume approach, the results tend towards those of the MPV method and show once again the dependency of the computational results on the flux calculation.

5.1.4.4. Noh test case (wall heating)

The next test case is based on Noh [68]. Similar to the above 123 problem, constant density and pressure are prescribed on either side of the shock tube.

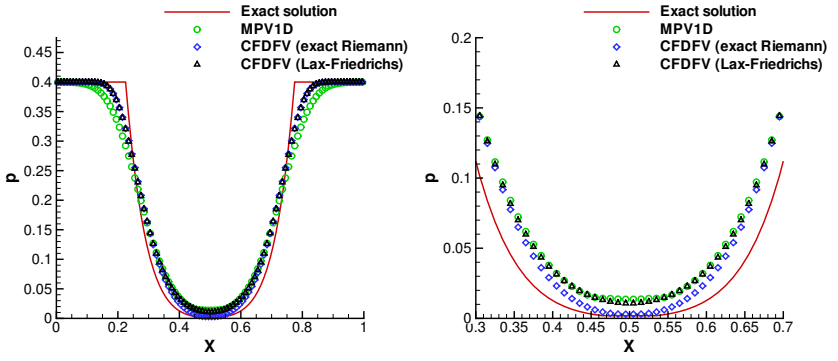

Figure 5.28.: 123 test case: pressure plot of the MPV and the finite volume CFDFV simulation at the time $t = 0.1$, including close-up view at the right (first order, 100 grid cells). The CFDFV code is run with an exact Riemann solver and the Lax-Friedrichs flux.

However, this time, there are two colliding shocks, caused by the opposite sign of the velocities in the left and right half of the shock tube. In the original test case setup [68], Noh uses an initial pressure that is equal to zero and that may cause numerical problems. In order to avoid these problems, a very low pressure of 10^{-6} is chosen according to Liska *et al.* [73] such that the following initial conditions are obtained

$$\begin{pmatrix} \rho_L \\ v_L \\ p_L \\ \gamma_L \end{pmatrix} = \begin{pmatrix} 1.0 \\ 1.0 \\ 10^{-6} \\ 5/3 \end{pmatrix}; x < 0.5 \qquad \begin{pmatrix} \rho_R \\ v_R \\ p_R \\ \gamma_R \end{pmatrix} = \begin{pmatrix} 1.0 \\ -1.0 \\ 10^{-6} \\ 5/3 \end{pmatrix}; x > 0.5. \tag{5.18}$$

The solution of this test is characterized by two shocks whose strength tends to infinity. They move in opposite directions from the domain center to the boundaries and they create a constant density and pressure in the center of the computational domain.
The results of the MPV method and the finite volume solver CFDFV are displayed in Fig. 5.29. It is obvious that both solvers are very well approaching the exact velocity and pressure distribution. The constant velocity and pressure

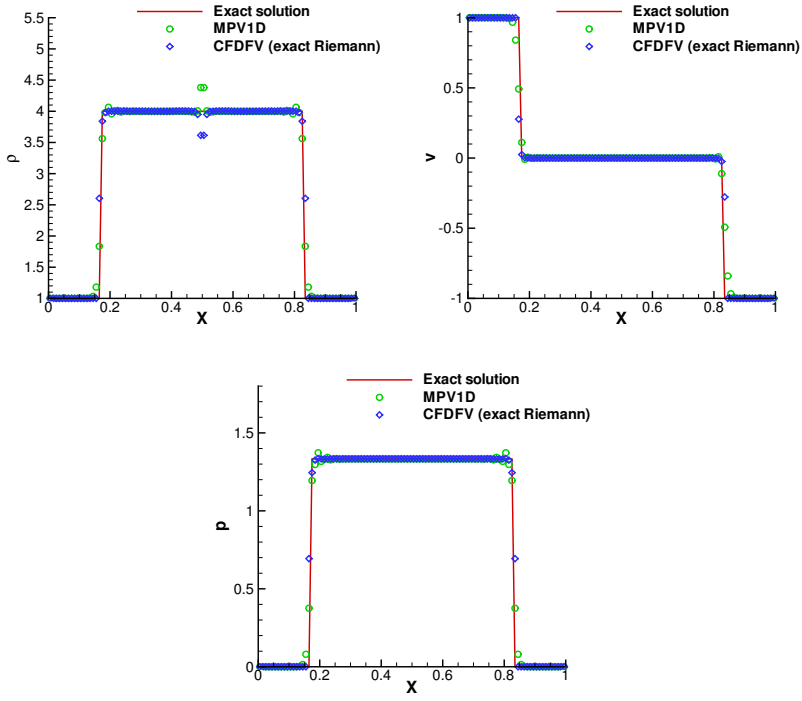

Figure 5.29.: Noh test case: density, velocity and pressure plot of the MPV and the finite volume CFDFV simulation (first order, 100 grid cells) and the exact solution at $t = 1.0$.

in the domain center are predicted correctly. Only the MPV method shows small oscillations at the shock location.

However, the situation is slightly different for the density. The density plot of Fig. 5.29 shows an overshoot for the MPV method and an undershoot for the finite volume scheme. This phenomenon is well-known as wall heating and described in detail by Noh [68], Menikoff [74], Rider [75] and many other

authors. This defect of shock-capturing schemes is typical for the reflection of a shock wave at a solid wall. The collision of the above initialized shock waves of equal strength is equivalent to such a reflection.
When the two shock waves are interacting, a numerical entropy production occurs. This entropy error causes the density to locally be lower than the exact solution in the case of the finite volume solver. As the pressure is correctly predicted, it is obvious from the equation of state that the fluid is heated locally and therefore the term wall heating has been introduced.

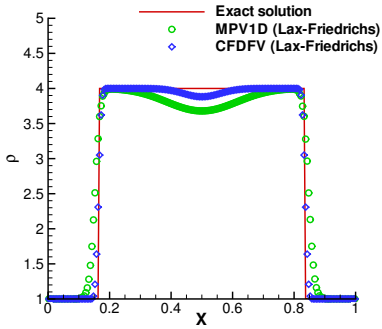

Figure 5.30.: Noh test case: density plot of the MPV and the finite volume CFDFV simulation with the Lax-Friedrichs flux (first order, 200 grid cells) and the exact solution at $t = 1.0$.

For the pressure-based MPV method, the effect is different. Here, we have a raise in density and therefore the fluid is cooled. Each numerical approach introduces an entropy error at the domain center and according to Noh [68], in the absence of physical viscosity, this error can only be dissipated by an artificial numerical viscosity. The nature of the defect is strongly dependent on the numerical method and especially its phase error and numerical diffusivity seem to play an important role, according to the literature [68, 74, 75]. This finding is confirmed by the numerical results of Fig. 5.29. While the MPV approach overpredicts the density and artificially cools the fluid, the finite volume approach heats the fluid. The direct comparison of the two schemes shows that the error amplitudes are of the same order of magnitude.

Moreover, it can be proven that the numerical scheme can change its properties once the numerical discretization is altered. This is evident from Fig. 5.30 where the results of the test case are displayed using the Lax-Friedrichs flux for both methods. While the finite volume solver still shows the above detected undershoot in density, the MPV method is now also underpredicting the density and therefore heating the fluid. This emphasizes the sensitivity of the wall heating defect to changes in the numerical discretization.
In addition, it is visible from Fig. 5.30 that the shocks are resolved differently, although both approaches use the same flux calculation method. The finite volume method captures the shock within six grid cells, while the semi-implicit MPV scheme needs approximately ten grid cells.

5.1.4.5. Conclusions

The pressure-based MPV scheme has been used for the computation of divers Riemann problems. For the standard Sod test case, it proves its capability to accurately predict the propagation of pressure waves. Furthermore, its shock-capturing properties have been assessed by applying it to test cases that are known to be critical for standard finite volume Godunov-type flow solvers. The corresponding findings are the following.
With regard to the simulation of strong rarefaction waves, several shock tube tests have been performed and compared to the results of a standard Godunov-type finite volume solver. According to the findings of Kudriakov *et al.* [64], both methods run into trouble when they have to deal with large initial density ratios, but the shock-capturing properties of the pressure-based method reveal to be inferior to those of the finite volume scheme. The issue appears to be related to the accuracy of the numerical flux evaluation that plays a crucial role for these kind of Riemann problems. Changing the numerical flux calculation of the finite volume scheme directly leads to a change in the predicted shock position and strength. Since the flux calculation for the semi-implicit pressure-based method cannot be changed as easily as for the explicit finite volume scheme, the accurate resolution of strong rarefactions seems to be a problem for the pressure-based MPV approach.
However, the absence of an explicit Riemann solver has also proven to be an advantage in the case of the slowly moving shock wave of Quirk [65]. There, the fact that the wave structures are not explicitly resolved by the numerical scheme prevents the results from being oscillatory.
Moreover, the MPV scheme has shown to be able to handle low density and low pressure flows as is obvious from the 123 problem. The numerical scheme

gives an accurate solution that is close to the exact one and again the fact that the MPV approach does not use a Riemann solver is of advantage as especially linearized Riemann solvers have problems to deal with such kind of flows [67]. The test case of Noh reveals that the MPV method also suffers from the well-known wall heating phenomenon. Its density error is comparable in amplitude to that of the standard finite volume solver. However, it is also shown that the error is dependent on the numerical discretization such that the MPV method causes either cooling or heating of the fluid.

5.1.5. Application of the MPV scheme to two-phase problems

The MPV approach is applied to compressible two-phase flows and validated by several test cases subsequently. The computations are carried out using the compressible multiphase extension for the MPV scheme that is presented in section 4.6 and most of the results are taken from [57]. Due to the large density ratios, the computations are limited to the first order approach with reference to the findings of section 4.7.1 and the corresponding results of section 5.1.3.1. The oscillation-free behavior at the material interface is demonstrated for the first order method by the transport of a contact discontinuity between two perfect gases. Afterwards, two-phase shock tube test cases show that the MPV method is able to accurately simulate the propagation of pressure waves in the multiphase case. Additionally, the semi-conservative approach is applied to a multiphase shock tube test case and compared to the MPV method in conservative formulation.

5.1.5.1. Transport of a material discontinuity between two perfect gases

This test case illustrates that the first order MPV method for the simulation of compressible multiphase flows is free of oscillations in the vicinity of material interfaces. An isolated material front between two perfect gases of different density and adiabatic exponent is considered in this test case introduced by Abgrall *et al.* [43]. The initial values are set as follows

$$\begin{pmatrix} \rho_L \\ v_L \\ p_L \\ \gamma_L \end{pmatrix} = \begin{pmatrix} 1 \\ 1 \\ 1 \\ 1.4 \end{pmatrix}; x < 0.5 \qquad \begin{pmatrix} \rho_R \\ v_R \\ p_R \\ \gamma_R \end{pmatrix} = \begin{pmatrix} 0.1 \\ 1 \\ 1 \\ 1.6 \end{pmatrix}; x > 0.5. \tag{5.19}$$

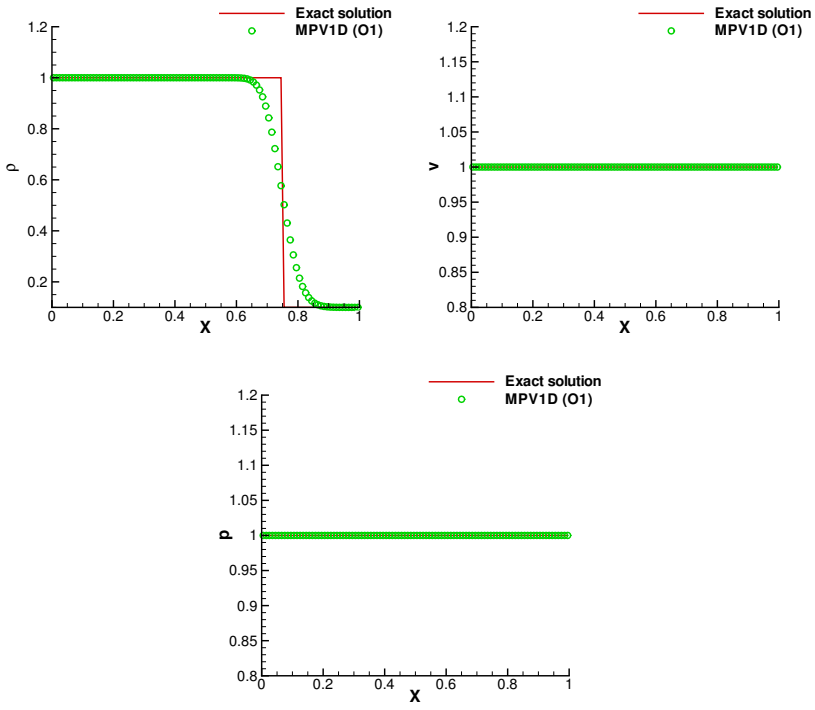

Figure 5.31.: Transport of a material discontinuity between two perfect gases: density, velocity and pressure plot of the MPV simulation and the exact solution at $t = 0.25$. The simulation is done with the first order (O1) MPV scheme using 100 grid cells.

In general, the numerical scheme is expected to transport the discontinuity with the given constant velocity. However, Abgrall *et al.* [43] showed that conservative density-based methods may suffer from oscillations in the vicinity of the material interface. These oscillations are prevented by the MPV method using the pressure as primary variable (cf. section 4.6.1). The results of the

MPV scheme are plotted in Fig. 5.31 and the pressure and velocity plots are obviously free of oscillations.

5.1.5.2. Sod test case with two different gases

The MPV approach in conservative and semi-conservative formulation is now applied to a two-phase shock tube that includes two perfect gases with different adiabatic exponents γ. The Sod test case initialization is used, but this time different values of γ are assigned to the fluids in the left and right half of the shock tube

$$\begin{pmatrix} \rho_L \\ v_L \\ p_L \\ \gamma_L \end{pmatrix} = \begin{pmatrix} 1.0 \\ 0 \\ 1 \\ 1.4 \end{pmatrix}; x < 0.5 \qquad \begin{pmatrix} \rho_R \\ v_R \\ p_R \\ \gamma_R \end{pmatrix} = \begin{pmatrix} 0.125 \\ 0 \\ 0.1 \\ 2.0 \end{pmatrix}; x > 0.5. \tag{5.20}$$

The semi-conservative approach can handle this without any difficulties as the change in the adiabatic exponent is easily taken into account locally calculating the speed of sound in each grid cell. The MPV approach in conservative formulation is also able to simulate this test case on the basis of the multiphase treatment described in section 4.6.
The computation has been carried out on a grid with 200 cells and the first order numerical scheme has been used in both cases. The corresponding results are shown in Fig. 5.32. The direct comparison of conservative and semi-conservative scheme reveals differences between both approaches. The conservative method is nicely approximating the different waves and it accurately predicts the shock. As for the standard Sod test case, the semi-conservative scheme approaches the analytical solution but has problems to exactly capture shock position and strength (cf. Fig 5.10). In direct comparison to the conservative scheme, the semi-conservative approach has inferior shock-capturing properties. This behavior gets more and more important with increasing shock strength, as it can be seen from the results of the single-phase test cases of the previous section. The use of a non-conservative pressure equation limits the range of applicability of the semi-conservative scheme to rather weak shocks but it gives the scheme a lot of flexibility as it can switch easily between different fluids being only dependent on the local speed of sound. For both approaches the results are free of oscillations in the vicinity of the material interface.

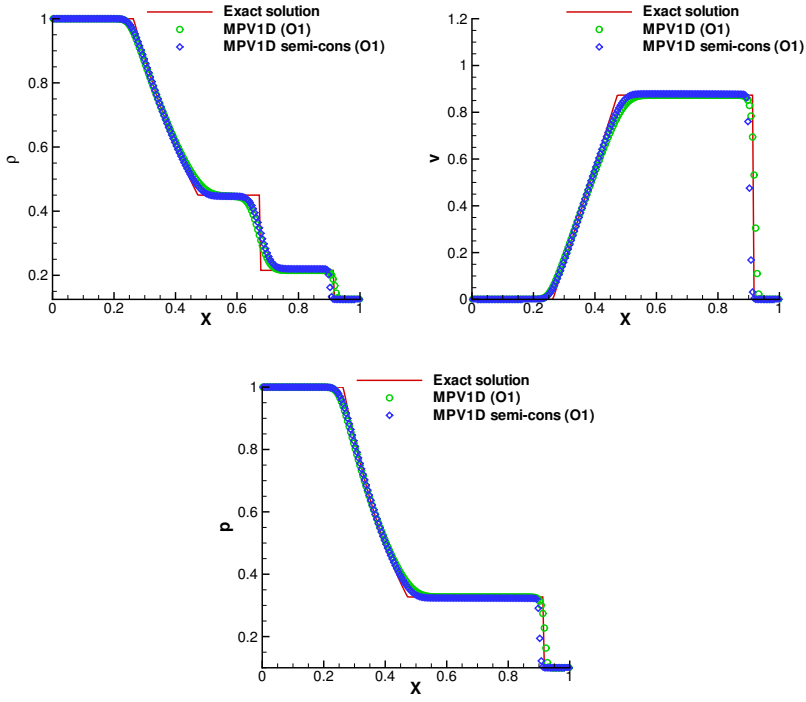

Figure 5.32.: Sod test case for two perfect gases ($\gamma_L = 1.4$, $\gamma_R = 2.0$): density, velocity and pressure plot of the MPV simulation in conservative and semi-conservative formulation (first order (O1), 200 grid cells) and the exact solution at $t = 0.2$.

5.1.5.3. Gas-water shock tube

The multiphase MPV approach in conservative formulation is now applied to a more severe test case taken from Hu *et al.* [76]. This two-phase shock tube includes a perfect gas and a water region modeled by the perfect gas equation of state and the Tait equation of state respectively. The initial discontinuity is

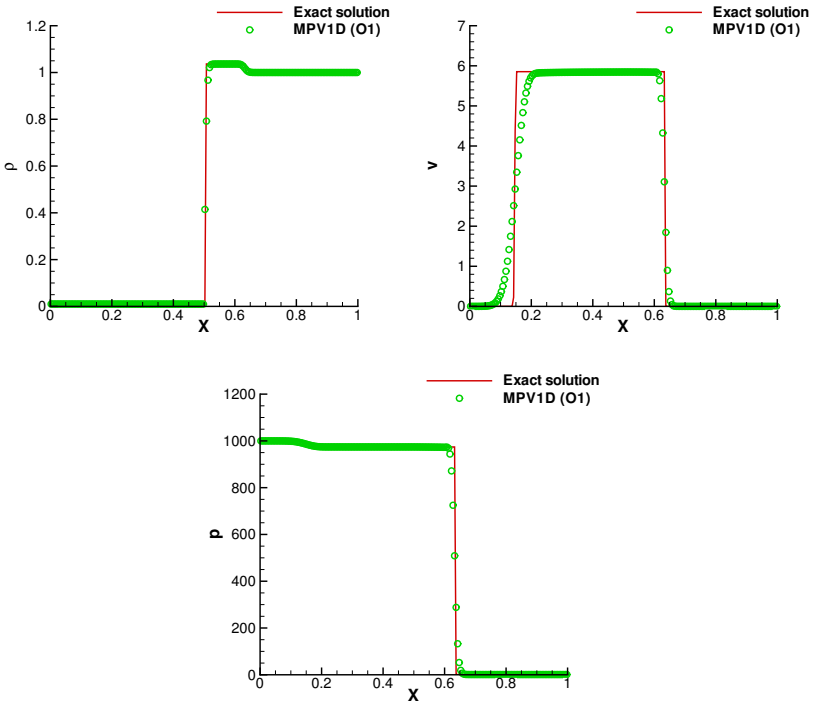

Figure 5.33.: Gas-water shock tube (perfect gas and Tait fluid): density, velocity and pressure plot of the MPV simulation and the exact solution at $t = 8 \cdot 10^{-4}$. The simulation is performed with 200 cells and the first order (O1) MPV scheme.

given by

$$\begin{pmatrix} \rho_L \\ v_L \\ p_L \\ \gamma_L \end{pmatrix} = \begin{pmatrix} 0.01 \\ 0 \\ 1000 \\ 2 \end{pmatrix} ; x < 0.5$$

$$\begin{pmatrix} \rho_R \\ v_R \\ p_R \\ \gamma_R \end{pmatrix} = \begin{pmatrix} 1 \\ 0 \\ 1 \\ 7.15 \end{pmatrix} ; \begin{pmatrix} k_0 \\ \rho_0 \\ p_0 \end{pmatrix} = \begin{pmatrix} 3310 \\ 1 \\ 1 \end{pmatrix} ; x > 0.5. \tag{5.21}$$

The initial conditions show much bigger density and pressure ratios than for the previous two-phase Sod shock tube (cf. equation (5.20)). Therefore, the test case is more challenging for the numerical scheme.
From the physical point of view, the test case can be characterized as follows. A shock wave is traveling through the water region and an expansion fan is propagating in the gas region.
The results of the first order MPV calculation with 200 grid cells are shown in Fig. 5.33. Again, the MPV approach shows a good, oscillation-free approximation of the exact solution, the shock and expansion waves are captured accurately.

5.1.5.4. Air bubble collapse

This last test case is an even more demanding two-phase shock tube that is characterized by a density ratio of almost 1000. Physically it corresponds to an air bubble collapse in one space dimension and has been taken from [77] where the initial conditions are given by

$$\begin{pmatrix} \rho_L \\ v_L \\ p_L \\ \gamma_L \end{pmatrix} = \begin{pmatrix} 1.0376 \\ 6.0151 \\ 1000 \\ 7.15 \end{pmatrix}; \begin{pmatrix} k_0 \\ \rho_0 \\ p_0 \end{pmatrix} = \begin{pmatrix} 3310 \\ 1 \\ 0.3477 \end{pmatrix}; x < 0.7$$
$$\begin{pmatrix} \rho_R \\ v_R \\ p_R \\ \gamma_R \end{pmatrix} = \begin{pmatrix} 0.001 \\ 0 \\ 1 \\ 1.4 \end{pmatrix}; x > 0.7. \tag{5.22}$$

The left side of the shock tube is filled with water at high pressure described by the Tait equation of state while the right part is filled with a perfect gas. Given these initial conditions a shock wave is created inside the gas region and an expansion fan is moving through the water.
The computational results of the multiphase MPV approach in conservative formulation are displayed in Fig. 5.34. For the calculation the first order scheme has been used and a spatial resolution of 700 grid cells has been necessary to accurately approach the exact solution. The numerical solution is close to the exact solution of this severe test case. However, it has to be mentioned that the flux calculation at the material interface has to be modified in a non-conservative way according to section 4.6 to capture the shock wave correctly.

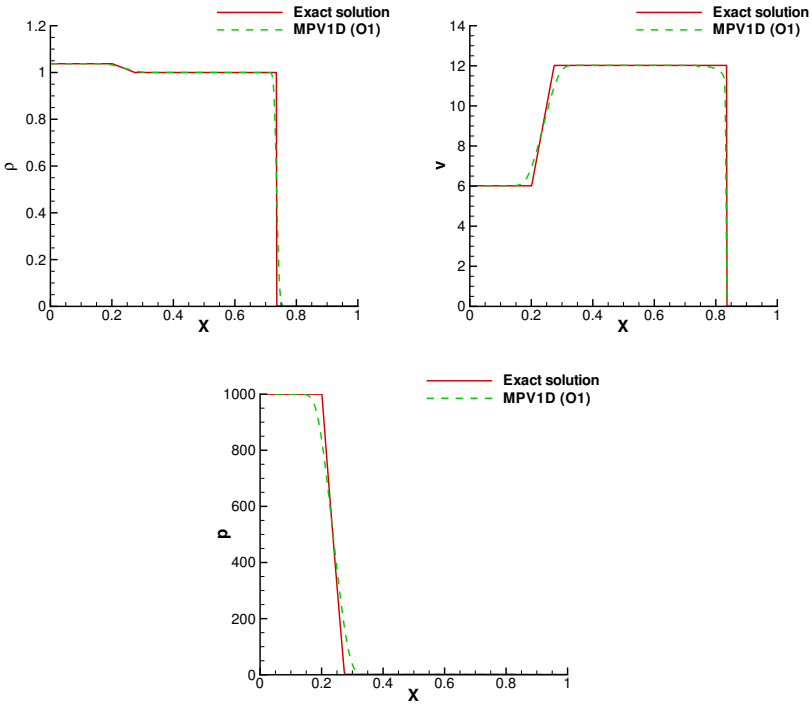

Figure 5.34.: Air bubble collapse test case (perfect gas and Tait fluid): density, velocity and pressure plot of the MPV simulation and the exact solution at $t = 3 \cdot 10^{-3}$. The simulation is performed with 700 cells and the first order (O1) MPV scheme using a special treatment of the pressure fluxes at the location of the material interface.

Without the modified pressure flux the shock strength and position are considerably mispredicted.

5.1.5.5. Conclusions

The MPV method shows to be able to simulate the propagation of pressure waves for multiphase flows. The first order method is free of pressure and velocity oscillations. This is true for the simple transport of a multi-material contact discontinuity as well as for shock tube test cases. Moreover, the semi-conservative MPV approach has been applied to the simulation of moderate shock waves where it proves to be able to simulate arbitrary equations of state without any difficulty, but also shows its limitations with respect to shock-capturing. The MPV approach in conservative formulation is successfully applied to challenging gas-water shock tube problems.

5.2. Three-dimensional calculations

In the following, three-dimensional incompressible and compressible two-phase flows are investigated. For the incompressible regime, the modeling of surface tension and the reduction of unphysical spurious currents in the context of the FS3D code is in the focus of this work.
The compressible MPV two-phase approach is applied to two shock-droplet interaction test cases where it proves its capability for the three-dimensional simulation of pressure waves in gas and liquid.

5.2.1. Reduction of parasitic currents in FS3D

The results of two numerical test cases for the validation of the balanced-force surface tension approach of the FS3D code introduced in section 4.3 are shown subsequently. The original study can be found in [47]. First, a static spherical droplet is investigated. Afterwards, surface tension driven oscillations are simulated.

5.2.1.1. Static droplet in equilibrium

For this test a static drop in equilibrium without gravity is considered with the FS3D code. In the absence of any outer forces, the drop should maintain its initial shape and the velocities should be zero everywhere throughout the whole computation. Moreover, for a spherical droplet the pressure jump across the interface, caused by surface tension, can be determined from equation (2.53). For this purpose, the curvature κ is calculated analytically as

$$\kappa = \frac{2}{R}, \tag{5.23}$$

where R is the droplet radius. The corresponding simulation is performed with a spherical water droplet with radius $R = 10^{-3}m$ that is surrounded by air. The drop is placed at the center of a cubic computational domain with an edge length of $4 \cdot 10^{-3}m$. The domain is discretized by 64 equidistant grid cells in each space direction. The computation has been run with the standard CSF and CSS models as well as with the newly implemented balanced-force CSF model of section 4.3.1.

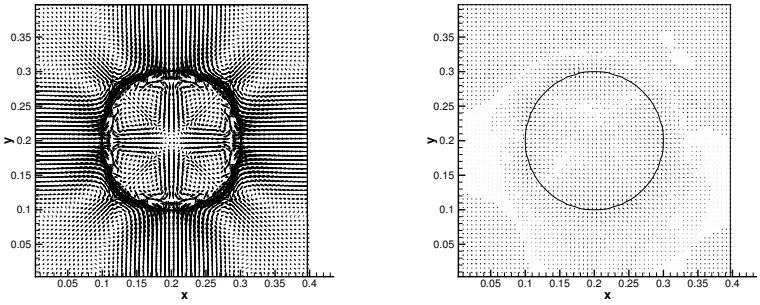

(a) Previous CSF model $|v_{max}| = 33.09 \frac{cm}{s}$.

(b) Balanced-force CSF model $|v_{max}| = 0.026 \frac{cm}{s}$ (vectors scaled by factor 100).

Figure 5.35.: Velocity field around and inside the static droplet in the xy-plane at $t = 0.03s$ (cut through the center of the droplet).

The resulting velocity distributions for both, the standard CSF implementation and the new balanced-force surface tension approach, are shown in Fig. 5.35. A vector plot of the velocities on a plane through the droplet center is shown for the previous CSF model in Fig. 5.35(a) and for the new, balanced-force CSF implementation in Fig. 5.35(b). The vectors in Fig. 5.35(b) are scaled by a factor 100 compared to the length of those in Fig. 5.35(a). From the velocity plots it is obvious that there is a dramatic reduction of spurious currents in the computational domain.
In order to get a more quantitative evaluation, the temporal evolution of the maximum velocity and the kinetic energy is depicted in Fig. 5.36. Compared to

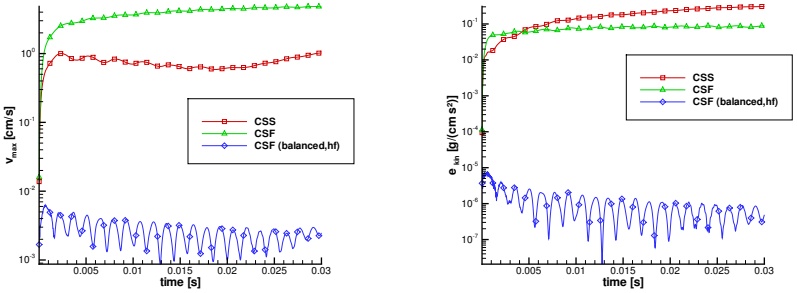

(a) Maximum velocity v_{max}.

(b) Kinetic energy e_{kin}.

Figure 5.36.: Comparison of maximum velocity and kinetic energy in the static droplet case for the CSS, CSF and the balanced-force CSF surface tension models.

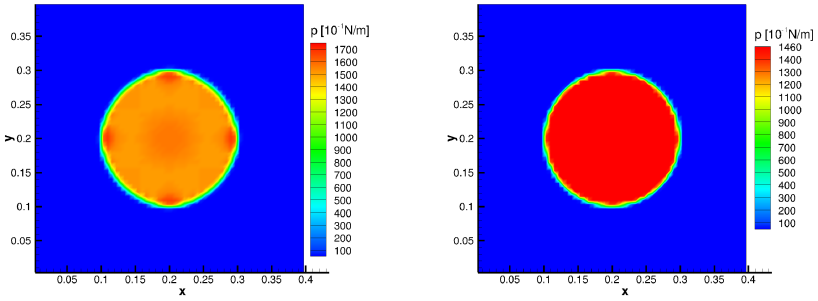

(a) Previous CSF model.

(b) Balanced-force CSF model.

Figure 5.37.: Pressure distribution around and inside the static droplet in the xy-plane at $t = 0.03s$ (cut through the center of the droplet).

the standard CSS and CSF models, the balanced-force CSF method reduces the maximum velocity by two orders of magnitude. While this maximum velocity only contains information about one special location in the domain, the kinetic energy represents the entirety of the spurious currents. A strong reduction of the kinetic energy can be observed with the balanced-force model (five orders of magnitude).
Tests with prescribed, constant curvature make the parasitic velocities completely vanish. This indicates that the above discussed remaining spurious currents of the balanced-force CSF model are due to the still not perfect calculation of curvature.
The pressure jump across the interface is predicted quite well by the balanced-force method as can be seen in Fig. 5.37. The Young-Laplace equation (2.53) gives a pressure jump of $\Delta p = 1460 \cdot 10^{-1} \frac{N}{m}$ that is accurately reproduced by the balanced-force approach. Moreover, the sharper interface resolution due to the more local discretization of the surface tension force, presented in section 4.3.1, can be notified.

5.2.1.2. Oscillating droplet

This test case aims at the computation of surface tension driven oscillations. Therefore, an initially non-moving ellipsoidal droplet, whose polar radius is bigger than its equatorial radii, is investigated with the FS3D code. Due to the non-spherical shape, the droplet starts to oscillate because of surface tension. For small deformations there exists an analytical approach by Lamb [78] that describes the oscillations. Neglecting the density of the surrounding fluid, he derived the following equation for the angular frequency of the oscillations

$$\omega^2 = l(l-1)(l+2)\frac{\sigma}{\rho_1 R^3}. \tag{5.24}$$

The parameter l characterizes the oscillation mode and for ellipsoidal deformations $l = 2$. Here, R represents the radius of the equivalent spherical droplet corresponding to the mass of the ellipsoidal droplet.
The deviation of the calculated oscillation periods from the analytical value of equation (5.24) is given in Tab. 5.6 for various test cases with droplets of different sizes. While the results for the standard CSF and CSS models are acceptable, an improvement can be observed when the balanced-force surface tension method is used.
This improvement gets even more evident by looking at the amplitude of the oscillation, given in Fig. 5.38 by the temporal evolution of the surface area. While

		Deviation [%]		
Mass $[g]$	T (Eq. (5.24)) $[s]$	CSS	CSF	CSF (balanced,hf)
$3.689489 \cdot 10^{-5}$	$7.7164 \cdot 10^{-4}$	-4.10	-6.43	1.73
$2.951591 \cdot 10^{-4}$	$2.18251 \cdot 10^{-3}$	-5.16	-7.68	1.95
$9.961621 \cdot 10^{-4}$	$4.00954 \cdot 10^{-3}$	-5.85	-7.47	2.01
$2.361273 \cdot 10^{-3}$	$6.17308 \cdot 10^{-3}$	-6.14	-7.74	1.97
$4.611861 \cdot 10^{-3}$	$8.62715 \cdot 10^{-3}$	-6.34	-7.85	2

Table 5.6.: Droplet oscillations, polar radius 10% bigger than the equatorial radii: Comparison of the oscillation periods for the CSS, CSF and the balanced-force CSF surface tension models.

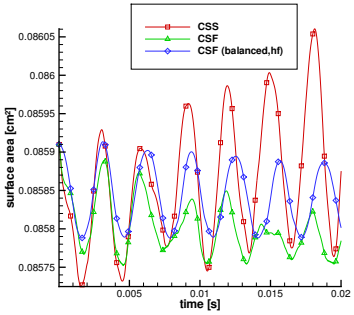

Figure 5.38.: Droplet oscillations, polar radius 10% bigger than the equatorial radii, mass $m = 2.361273 \cdot 10^{-3} g$: Comparison of the oscillation periods and amplitudes for the different surface tension models.

the periodic deformation of the droplet is described nicely with a constant minimum and a slight damping by the balanced-force method, the standard CSF method shows an erratic development of the droplet's surface area. Looking at the CSS method, things get worse as the amplitude of the droplet oscillation increases in time, thus there is a generation of kinetic energy due to the

spurious currents.

5.2.1.3. Conclusions

The computational results of a balanced-force CSF method for the calculation of surface tension within the framework of the incompressible VOF code FS3D have been presented. The main features of the method are a balanced discretization of the volume force at the interface as well as an improved curvature calculation using height functions and a local paraboloid fitting (cf. section 4.3.1).
The balanced-force method shows a strong reduction of spurious currents for the calculation of a droplet in equilibrium. The maximum velocity of the spurious currents can be reduced by two orders of magnitude and the kinetic energy caused by the parasitic currents even shows a reduction of five orders of magnitude. Looking at the case of an oscillating droplet, there is a clear improvement with regard to the prediction of the oscillation frequency and the temporal evolution of the oscillation amplitude.
In [79] this approach has also been successfully applied to study the rise behavior of small bubbles with the FS3D code.

5.2.2. Shock-droplet interactions

In the following, the focus is on three-dimensional simulations with the compressible multiphase MPV approach. Two shock-droplet interaction test cases, without the modeling of surface tension, are presented that originally have been investigated in [58]. They are inspired by the test cases of Chang *et al.* [80], whereas they only performed two-dimensional calculations.
Unless otherwise stated, the computations are set up as follows: The perfect gas equation of state with the adiabatic exponent $\gamma = 1.4$ is used for the surrounding gas phase and the stiffened gas equation of state with $p_\infty = 3309$ is applied to the liquid phase inside the droplet. For the Tait equation of state (2.8) this corresponds to the following choice of constants for the liquid: $k_0 = 3310$, $p_0 = 1$ and $\rho_0 = 1000$. For all test cases, the shock is initialized as a discrete wave to minimize the effects of numerically caused spurious waves created at the start-up phase. The discrete shock wave is taken from the results of the MPV solver for the corresponding one-dimensional Riemann problem. With this initialization, still weak waves are created that travel in x-direction to the left (cf. Fig. 5.39(b)) while the shock is propagating to the right. To prevent the waves from influencing the computational results by reflections at

the boundaries, the domain size in the x-direction is chosen twice as large as in the other two spatial directions. This also necessitates to double the number of grid cells in this direction, such that for the standard case 128 equidistant grid cells in x-direction and 64 equidistant grid cells in each of the other two spatial directions are used. The computations are carried out with the second order RK2CN MPV method.

5.2.2.1. Single droplet

The first test case describes the impact of an initially planar shock wave on a spherical droplet. The simulation is characterized by the propagation of pressure waves inside and outside the water droplet including several reflections. The initial conditions of the test case are specified in Fig. 5.39(a) and the pressure distribution on a slice through the center of the droplet at the instant $t = 7.5 \cdot 10^{-3}$ is shown in Fig. 5.39(b).

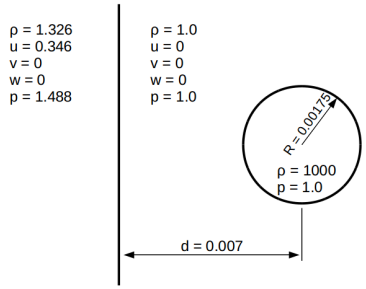

(a) Sketch of the setup for the three-dimensional shock-droplet interaction test case including a single spherical droplet.

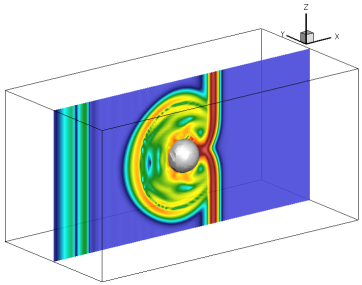

(b) Slice through the droplet center at $t = 7.5 \cdot 10^{-3}$ showing the distribution of the pressure gradient $\log(|\nabla p| + 1)$.

Figure 5.39.: Three-dimensional shock-droplet interaction: single droplet.

A more detailed analysis of the pressure field can be carried out by having a closer look at the pressure and the pressure gradient distributions at different instants that are given in Fig. 5.40. It is obvious that by plotting the gradient of the pressure $\log(|\nabla p|+1)$, the wave structures can be resolved in more detail.

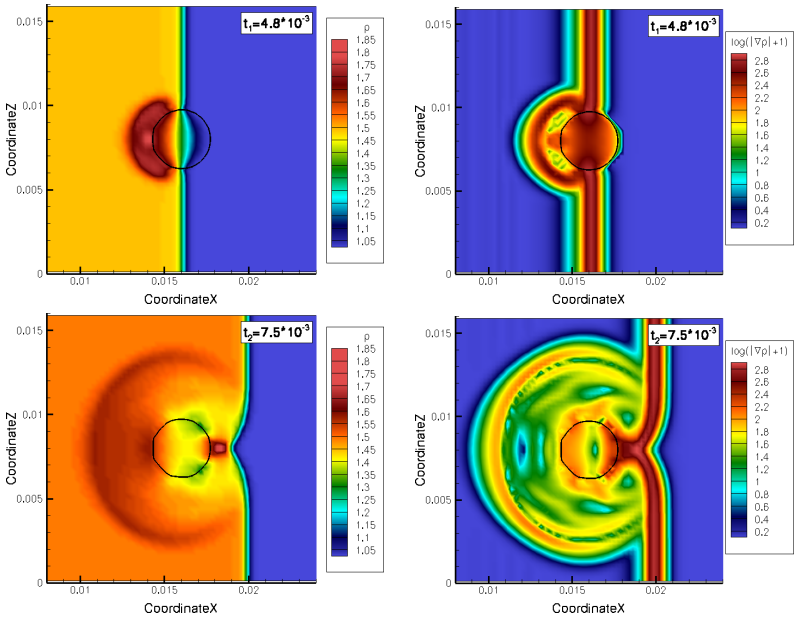

Figure 5.40.: Three-dimensional shock-droplet interaction test case including a single droplet. Pressure p and pressure gradient $\log(|\nabla p| + 1)$ at $t_1 = 4.8 \cdot 10^{-3}$ (top) and $t_2 = 7.5 \cdot 10^{-3}$ (bottom), slices through the droplet center.

When the shock wave is impinging on the droplet surface, the shock is reflected as well as transmitted into the droplet. While the reflected wave forms a bow shock due to the spherical geometry of the droplet, the transmitted wave is traveling through the droplet. Because of the higher speed of sound inside the droplet, the shock wave obviously is moving faster inside than outside. This is evident from the plot at $t_1 = 4.8 \cdot 10^{-3}$ in Fig. 5.40. The pressure distribution inside the droplet is no longer uniform, especially with respect to the pressure gradient, indicating that the shock has already traveled through the complete droplet. Moreover, the shock is reflected at the rear part as an expansion that is moving back to the front. During the following time steps, the waves are

reflected several times inside the droplet. At $t_2 = 7.5 \cdot 10^{-3}$, the shock wave has made its way around the droplet and the waves are interacting at the rear part, forming a curved shock front in the gas phase.
Looking at the plots of pressure and pressure gradient, both are indicating a perfectly symmetric distribution at any time.
The MPV method with the interface treatment presented in section 4.6 is not suffering from any pressure or velocity oscillations near the interface. This is illustrated in three space dimensions by the results displayed in Fig. 5.41. The contour lines of pressure show a smooth transition between the two phases. Additionally, the velocity vectors are not indicating any oscillations. Hence, the pressure-based MPV method proves to give oscillation-free results for the three-dimensional simulation of compressible two-phase flows.

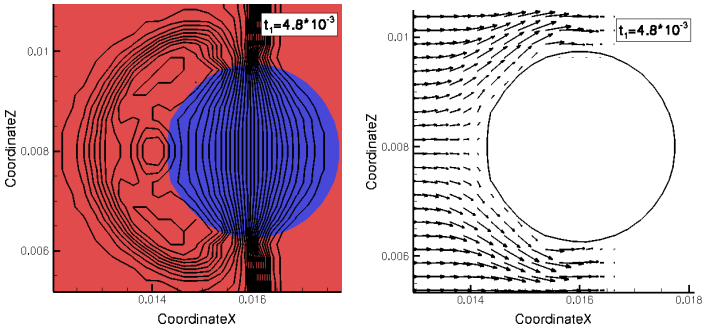

(a) Contour lines of pressure.

(b) Velocity field with vectors at each grid node.

Figure 5.41.: Three-dimensional shock-droplet interaction test case: slice through the droplet center at $t_1 = 4.8 \cdot 10^{-3}$.

5.2.2.2. Two droplets

As a modification to the previous shock-droplet test case, a second spherical droplet is introduced. This generates additional wave reflections and interactions that finally result in a more complex wave pattern.
The initial setup is presented in Fig. 5.42(a) and the pressure gradient distribution on a slice through the droplet centers at the time $t = 8.3 \cdot 10^{-3}$ is depicted

in Fig. 5.42(b). Similar to the single droplet case, Fig. 5.43 illustrates the pressure as well as the pressure gradient distribution at the instant $t = 8.3 \cdot 10^{-3}$.

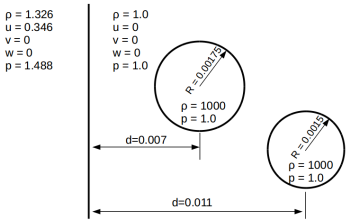

(a) Sketch of the setup for the three-dimensional shock-droplet interaction test case including two spherical droplets.

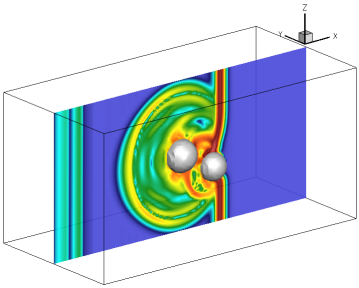

(b) Slice through the droplet centers at $t = 8.3 \cdot 10^{-3}$ showing the distribution of the pressure gradient $\log(|\nabla p| + 1)$.

Figure 5.42.: Three-dimensional shock-droplet interaction: two droplets.

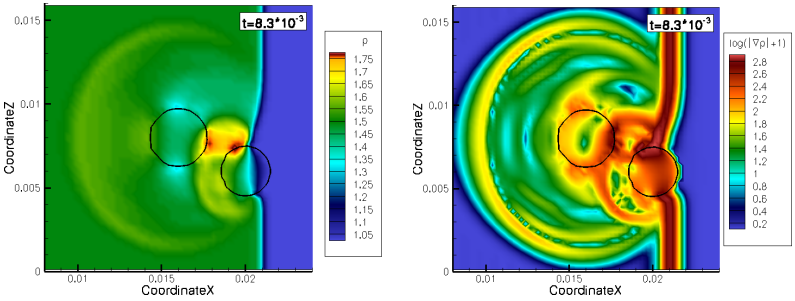

Figure 5.43.: Three-dimensional shock-droplet interaction test case including two droplets. Pressure p and pressure gradient $\log(|\nabla p| + 1)$ at $t = 8.3 \cdot 10^{-3}$, slices through the droplet centers.

Inside the bigger droplet, the distribution of pressure is non-symmetric at $t = 8.3 \cdot 10^{-3}$. This is particularly evident from the pressure gradient distribution. This effect is due to the presence of the smaller droplet. The right moving initial shock wave finally impinges on the surface of the smaller droplet where it is reflected. The reflected wave has a curved shape, it travels back towards the bigger droplet and hits its surface in the rear part. This impact influences the wave pattern inside the big droplet.

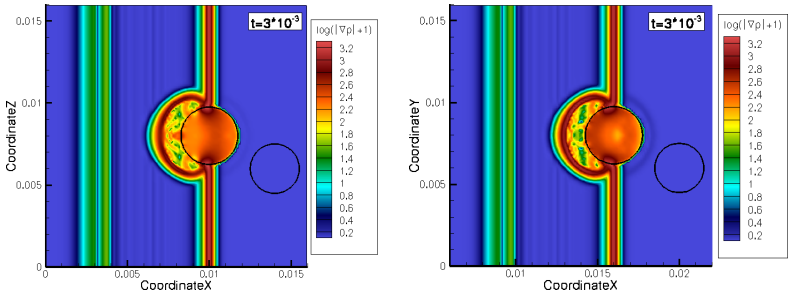

Figure 5.44.: Comparison of two-dimensional (128^2 grid cells; right) and three-dimensional (256×128^2 grid cells; left) computations for the shock-droplet interaction test case including two droplets. Distribution of the pressure gradient $\log(|\nabla p|+1)$ at $t = 3{\cdot}10^{-3}$, slices through the droplet centers.

In Fig. 5.44 a three-dimensional simulation is compared to a two-dimensional one at the instant $t = 3 \cdot 10^{-3}$. For the three-dimensional case, the initial setup of Fig. 5.42(a) has slightly been modified. Firstly, the spatial resolution has been increased using 256 grid cells in x-direction and 128 cells in the y- and z-direction. Due to this higher spatial resolution it is possible to initialize the shock closer to the droplet interface such that the initial distance from shock wave to droplet center can be reduced to $d = 0.0045$ and computational time can be saved. For the two-dimensional calculation, the same code has been employed with a two-dimensional version of the above presented initialization and spatial resolution, such that the size of the grid cells is equal.
There are two points to remark. First of all, the wave patterns inside the droplets look different. This is due to three-dimensional effects, caused by the spherical shape of the three-dimensional droplet that creates different wave

reflections in comparison to the two-dimensional case. Moreover, behind the bigger droplet, a very weak shock wave is visible in both cases. This wave is the transmitted initial shock wave that has moved through the droplet and is now propagating through the air behind the droplet. It is clearly more pronounced in the two-dimensional case than in the three-dimensional calculation.

5.2.2.3. Conclusions

The presented three-dimensional shock-droplet interactions show that the MPV method is able to resolve complex wave patterns including several wave reflections inside and outside of liquid droplets. Moreover, the three-dimensional scheme proves to be oscillation-free in the vicinity of the interface and a comparison between a two- and a three-dimensional computation reveals that pressure waves are reflected differently in the two cases due to the differences in geometry and topology.

6. Conclusion and prospects

In this thesis a pressure-based numerical method for the DNS of compressible multiphase flows is presented. The numerical approach is suited to the extension of incompressible multiphase flow solvers to the compressible regime. In the context of this work, several investigations have been performed that range from fundamental one-dimensional considerations for the coupling of compressible and incompressible flow regions to the three-dimensional simulation of shock-droplet interactions. From a physical and mathematical point of view, the focus of this work is on the compressible and incompressible flow equations and their connection. Hence, the coupling of compressible and incompressible flow regions has been investigated. Several iterative coupling procedures have been presented for the one-dimensional case. Such a coupling is challenging due to the differences in the physical modeling and in the underlying mathematical equations. It has been shown that the role of pressure changes during the transition from the compressible to the incompressible flow equations. The different coupling schemes are distinct in the way the pressure of the compressible flow region is coupled to the incompressible pressure. Numerical results indicate the accordance of the presented coupling schemes with a fully compressible two-phase flow solver that approaches the incompressible flow region by a weakly compressible fluid.

With respect to the simulation of incompressible two-phase flows, surface tension modeling has been investigated in the context of so-called parasitic currents. It has been shown that the magnitude of the numerically induced spurious velocities is directly dependent on the discretization of the capillary force and the calculation of the interface curvature that is used in the surface tension model. The presented results prove that the implementation of a balanced-force surface tension approach in combination with an improved numerical curvature estimation reduces the spurious velocities by several orders of magnitude.

The fundamental theoretical analysis concerning the coupling of compressible and incompressible flow regimes and the topic of surface tension modeling are complemented by intensive numerical investigations and developments for the pressure-based MPV method. This numerical scheme originally extends an incompressible flow solver to the simulation of compressible single-phase flows in

conservative formulation. The conservative MPV method has been extended to the treatment of compressible two-phase flows. This includes its combination with a level set interface tracking approach. It has been shown that the spatial discretization of the MPV scheme allows to handle contact discontinuities between two different compressible fluids in an oscillation-free manner. The jump in the equation of state is taken into account similar to a sharp interface approach, while the density jump is numerically smeared by the scheme. Additionally, a semi-conservative approach has been derived that replaces the energy equation by a nonconservative pressure equation allowing the use of arbitrary equations of state.

The conservative numerical approach has been thoroughly assessed with respect to single- and two-phase flows. A detailed numerical study on the shock-capturing and wave propagation properties of the single-phase MPV scheme has been presented. The results have been extensively discussed and compared to those of a standard Godunov-type finite volume solver. The comparison shows that the MPV scheme is often inferior to the finite volume solver and that the origin of this behavior is the less accurate upwind flux calculation due to the lack of a Riemann solver. However, this lack can also be beneficial, as the MPV scheme does not have any trouble in handling test cases that are delicate to Godunov-type methods. This includes for example the case of slowly moving shocks for which the use of Riemann solvers introduces spurious oscillations, or low density flows, where certain Riemann solvers break down. In the case of compressible two-phase flows, standard multi-material Riemann problems have been computed in one space dimension.

The MPV method proves to be able to simulate the propagation of pressure waves for single-phase as well as for multiphase flows. Moreover, the scheme has also been applied successfully to three-dimensional shock-droplet interactions where the propagation and reflection of pressure waves has been simulated.

In general, the MPV scheme demonstrates its ability to simulate compressible two-phase flows, including the propagation of pressure waves. However, the simulation of shock waves with the MPV method has also shown certain limitations, as the approach is inferior to density-based schemes in the case of strong shocks and rarefactions, even in its conservative formulation. Therefore, the MPV approach seems to be rather suitable to the weakly compressible regime, where in the absence of strong shocks other compressible effects like phase change play a dominant role. Besides, there are still a lot of open questions:

- The current MPV scheme is limited to the stiffened gas equation of state.

Although this approach contains the perfect gas equation of state as well as the Tait equation of state, the use of more realistic equations of state is desirable. Such equations of state allow to simulate the thermodynamic behavior more accurately and offer the possibility to take into account a variety of physical effects like phase change and cavitation. For this purpose, suitable cubic equations of state have to be implemented to the pressure-based numerical scheme. In this context, a thermodynamically consistent interface treatment will have to be derived for the MPV approach. It has already been proven in this thesis that due to the use of pressure as primary variable, the prevention of pressure oscillations is facilitated. However, for a pressure-based scheme, the thermodynamically consistent explicit insertion of a cubic equation of state into the energy equation is not trivial.

- Multiphase flow simulations including liquid and gas are characterized by high density ratios. It has been shown that the second order version of the MPV scheme has difficulties in handling strong density jumps across contact discontinuities, even for single-phase flows. In order to improve the spatial order of accuracy without suffering from spurious oscillations, a solution to this problem has to be found. A possible remedy may be the use of the first order scheme in combination with an adaptive mesh refinement in the direct vicinity of the density jump, i.e. at the interface location.

- The investigation of the boundary conditions for the compressible MPV solver on a staggered grid is of special interest, too. It has been found and shown that the standard treatment for finite volume schemes cannot be applied.

- At the interface, a lot of physical phenomena are happening that are of interest for the numerical simulation, but that are not yet taken into account by the present MPV approach for compressible multiphase flows. This includes the modeling of surface tension as well as the thermodynamically consistent simulation of phase change.

- The tracking and resolution of the interface is crucial for the DNS of two-phase flows. Especially the simulation of phenomena linked to the interface topology (e.g. surface tension, phase change) requires an accurately resolved material interface. In this context, a worthwhile aim is to use a sophisticated interface tracking scheme. This may be realized

by discretizing the level set equation with a high-order DG scheme. The polynomial representation of the level set function allows to easily and accurately evaluate its derivative that is needed to determine topology informations like surface normals and curvature.

A. SBDF time discretization

Based on the method of lines approach of equation (4.22) the second order time discretization for the MPV scheme with the SBDF (semi-implicit backward differentiation formula) method can be written as follows

$$\begin{aligned} \vec{U}^{n+1} &= \frac{1}{1+2q}\left[(1+q)^2\vec{U}^n - q^2\vec{U}^{n-1}\right] + \\ &\quad \frac{(1+q)\Delta t}{1+2q}\left[(1+q)\boldsymbol{f}(\vec{U}^n) - q\boldsymbol{f}(\vec{U}^{n-1}) + \boldsymbol{g}(\vec{U}^{n+1})\right], \end{aligned} \tag{A.1}$$

where q is the time step ratio

$$q = \frac{t^{n+1} - t^n}{t^n - t^{n-1}}. \tag{A.2}$$

It is obvious that the SBDF method requires the flow variables of the instants t^{n-1} and t^n in order to compute the flow variables $\vec{U}^{n+1}$ at the new instant of time.

B. One-dimensional DG sharp interface approach for compressible two-phase flows

The following description of the one-dimensional DG solver for multiphase flows is an excerpt from [59] by Jaegle *et al.* where a more detailed description can be found.
The multiphase solver is based on the compressible Euler equations and the flow domain is discretized in space using a nodal DG approach [81] whose order of accuracy can be adapted by choice of the polynomial degree of the basis functions. The temporal discretization is done with a Runge-Kutta method of order four. In order to avoid numerical oscillations that appear in high-order formulations, a simple artificial viscosity approach based on a Jameson-type sensor is available. The numerical fluxes are obtained using two different kinds of Riemann solvers: in the single-phase regions, a standard HLL Riemann solver [60] is used. The flux calculation only has to be modified at the location of the liquid-gas interface. There, the numerical flux is evaluated on the basis of one of the two-phase Riemann solvers described in [59]. The interface position is advanced by time-integration of a level set transport equation where the interface velocity is used that is given by the two-phase Riemann solver. The sharp interface approach of the one-dimensional framework avoids numerical smearing of the two phases imposing jump conditions (e.g. from a Riemann solver) at the sharp interface between two grid cells. A technique similar to the ghost fluid approaches by [82, 83] is used in the present case: at the cell boundary closest to the position of the interface, the fluid type is discretely switched between gas and liquid. The grid cells are either assigned to the gaseous or the liquid phase as the material interface is shifted to the closest cell boundary. Figure B.1(a) illustrates an interface with gas on the left and liquid on the right side. For the solution of the Riemann problem, the two-phase Riemann solver uses information from both fluids as initial data. A closer look at the right side of Fig. B.1(b) shows that the numerical flux on the gaseous side is calculated with information from the part of the Riemann solution left of the contact discontinuity, while the flux in the liquid phase is based on the

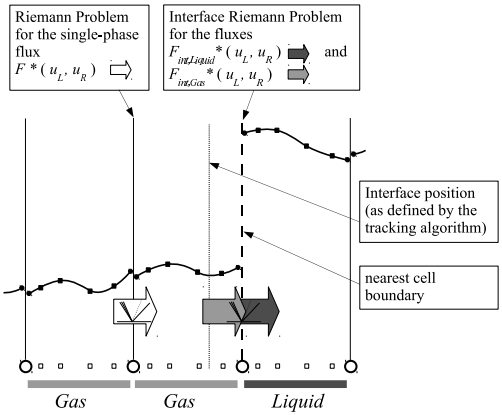

(a) Schematic of the DG polynomials and the definition of the intercell Riemann problems.

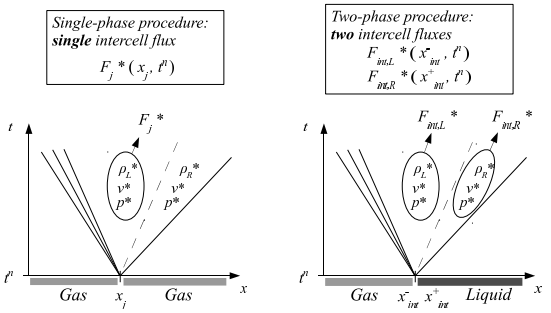

(b) Example for the wave pattern of single- and multiphase Riemann problems.

Figure B.1.: Schematic of the DG polynomials and the Riemann solvers used by the one-dimensional sharp interface framework. Sketches by Felix Jaegle [59].

flow variables of the right half of the Riemann solution.
Besides the case of a stationary interface, this approach can also be applied to a moving interface as the interface position is tracked accurately and independently from the grid. The interface (i.e. the cell boundary closest to the actual interface position) always moves from one grid node to the next. In such a situation, an extrapolation step is needed. *The one-dimensional framework uses information from the two-phase Riemann solution to assign the unknown state inside a cell that changes its fluid type during a time step. Just as with the standard ghost-fluid method, conservation is not guaranteed. However, in the temporal average the error on mass conservation can be expected to be small if the interface position is accurately tracked.*[1]

[1] by Felix Jaegle, cited from [59]

C. Godunov-type finite volume approach

In the following, a short description of the basic ideas of a finite volume method is given. More details can be found in the literature, for example in [54, 84]. The present finite volume code CFDFV solves the compressible Euler equations for single-phase flows in two space dimensions. The Euler equations are a system of hyperbolic partial differential equations that describe the conservation of mass, momentum and energy. The conservative formulation of this system is given as follows

$$\vec{U}_t + \nabla \cdot f(\vec{U}) = 0, \tag{C.1}$$

where $\vec{U}$ is the vector of the conserved quantities and $f(\vec{U})$ describes the flux tensor

$$\vec{U} = \begin{pmatrix} \rho \\ \rho u \\ \rho v \\ e \end{pmatrix}, \qquad f(\vec{U}) = \begin{bmatrix} \rho u & \rho u^2 + p & \rho v u & u(e+p) \\ \rho v & \rho u v & \rho v^2 + p & v(e+p) \end{bmatrix}. \tag{C.2}$$

The basic idea of the finite volume method is to use integral conservation equations, instead of the discrete conservation equations (C.1) that cause problems at the location of discontinuities (shock waves for example). The integral formulation of the equations is obtained by integration over the control volume V_i and the time t:

$$\int_{t^n}^{t^{n+1}} \int_{V_i} \vec{U}_t dV dt + \int_{t^n}^{t^{n+1}} \int_{V_i} \nabla \cdot f(\vec{U}) dV dt = 0. \tag{C.3}$$

As a next step, the Gauss theorem is applied to equation (C.3)

$$\int_{t^n}^{t^{n+1}} \int_{V_i} \vec{U}_t dV dt + \int_{t^n}^{t^{n+1}} \int_{\partial V_i} f(\vec{U}) \cdot \vec{n} dS dt = 0. \tag{C.4}$$

Then, integral averages of the conserved quantities are introduced for each control volume V_i at each time t^n and defined as

$$\vec{U}_i^n = \frac{1}{|V_i|} \int_{V_i} \vec{U}^n dV. \tag{C.5}$$

The temporal integration of the conservation equation (C.4) in the interval $[t^n, t^{n+1}]$ leads to

$$\vec{U}_i^{n+1} = \vec{U}_i^n - \frac{1}{|V_i|} \int_{t^n}^{t^{n+1}} \int_{\partial V_i} f(\vec{U}) \cdot \vec{n} dS dt. \tag{C.6}$$

This is an evolution equation for the integral cell averages $\vec{U}_i^n$. Up to now, this evolution equation is exact as the conservation of the integral quantities is guaranteed automatically. It is evident from equation (C.6) that the cell average $\vec{U}_i^n$ is updated on the basis of the fluxes across the domain boundaries. Now, the difficulty lies in the evaluation of the flux integrals. At each surface s_i that confines the control volume, the corresponding flux integral has to be evaluated

$$f_{s_i} = \frac{1}{|V_i|} \int_{t^n}^{t^{n+1}} \int_{s_i} f(\vec{U}) \cdot \vec{n} dS dt. \tag{C.7}$$

In general, it is not possible to exactly evaluate these integrals as the quantities at the domain boundaries and their temporal variation are unknown. Therefore, approximations have to be introduced to compute the flux integrals.
First of all, the flow variables at the domain boundaries have to be known. They may be reconstructed from the integral quantities. In the simplest first order case, the flow variables are supposed to be constant in the whole control volume and therefore they are identical to the integral cell averages. Once the flow variables at the boundaries are determined, the evaluation of the fluxes is not directly evident, as at each domain boundary the quantities are discontinuous. The characteristic of Godunov-type schemes is to use Riemann solvers to determine the quantities at the location of the control volume border on the basis of discontinuous flow quantities and to describe their evolution in the temporal interval $[t^n, t^{n+1}]$. There exist a lot of different Riemann solvers and an excellent overview is given in the book of Toro [60].

Bibliography

[1] C. Hirsch. *Numerical Computation of Internal and External Flows: The Fundamentals of Computational Fluid Dynamics.* Butterworth-Heinemann, 2007.

[2] A. J. Chorin. Numerical Solution of the Navier-Stokes Equations. *Math. Comput.*, 22(104):745–762, 1968.

[3] A. T. Harlow and J. E. Welch. Numerical calculation of time-dependent viscous incompressible flow of fluid with a free surface. *Phys. Fluids*, 8:2182–2189, 1965.

[4] O. Janzen. Beitrag zu einer Theorie der stationären Strömung kompressibler Flüssigkeiten. *Phys. Zeits.*, 14:639–643, 1913.

[5] L. Rayleigh. On the flow of compressible fluid past an obstacle. *Philos. Mag. Series 6*, 32(187):1–6, 1916.

[6] S. Klainerman and A. Majda. Compressible and incompressible fluids. *Commun. Pur. Appl. Math.*, 35:629–653, 1982.

[7] R. Klein. Semi-implicit extension of a Godunov-type scheme based on low Mach number asymptotics I: one-dimensional flow. *J. Comput. Phys.*, 121:213–237, 1995.

[8] H. Bijl and P. Wesseling. A Unified Method for Computing Incompressible and Compressible Flows in Boundary-Fitted Coordinates. *J. Comput. Phys.*, 141:153–173, 1998.

[9] D. R. van der Heul, C. Vuik and P. Wesseling. A conservative pressure-correction method for flow at all speeds. *Comput. Fluids*, 32:1113–1132, 2003.

[10] C.-D. Munz, S. Roller, R. Klein and K.-J. Geratz. The extension of incompressible flow solvers to the weakly compressible regime. *Comput. Fluids*, 32:173–196, 2003.

[11] J. H. Park and C.-D. Munz. Multiple pressure variables methods for fluid flow at all Mach numbers. *Int. J. Numer. Meth. Fl.*, 49:905–931, 2005.

[12] R. Scardovelli and S. Zaleski. Direct numerical simulation of free-surface and interfacial flow. *Annu. Rev. Fluid Mech.*, 31:567–603, 1999.

[13] V.-T. Nguyen, J. Peraire, B. C. Khoo and P.-O. Persson. A Discontinuous Galerkin Front Tracking Method for Two-Phase Flows with Surface Tension. *Comput. Fluids*, 39(1):1–14, 2010.

[14] S. O. Unverdi and G. Tryggvason. A Front-Tracking Method for Viscous, Incompressible, Multi-fluid Flows. *J. Comput. Phys.*, 100:25–37, 1992.

[15] C. W. Hirt and B. D. Nichols. Volume of fluid (VOF) method for the dynamics of free boundaries. *J. Comput. Phys.*, 39(1):201–225, 1981.

[16] S. Osher and J. A. Sethian. Fronts propagating with curvature-dependent speed: Algorithms based on Hamilton-Jacobi formulations. *J. Comput. Phys.*, 79(1):12–49, 1988.

[17] J. A. Sethian and P. Smereka. Level set methods for fluid interfaces. *Annu. Rev. Fluid Mech.*, 35:341–372, 2003.

[18] M. Sussman and E. Fatemi. An efficient interface-preserving level set redistancing algorithm and its application to interfacial incompressible fluid flow. *SIAM J. Sci. Comput.*, 20(4):1165–1191, 1999.

[19] E. Marchandise, J.-F. Remacle and N. Chevaugeon. A quadrature-free discontinuous Galerkin method for the level set equation. *J. Comput. Phys.*, 212:338–357, 2006.

[20] M. Sussman, A. S. Almgren, J. B. Bell, P. Colella, L. H. Howell and M. L. Welcome. An adaptive level set approach for incompressible two-phase flows. *J. Comput. Phys.*, 148:81–124, 1999.

[21] M. Herrmann. A balanced force refined level set grid method for two-phase flows on unstructured flow solver grids. *J. Comput. Phys.*, 227:2674–2706, 2008.

[22] M. Sussman and E. G. Puckett. A Coupled Level Set and Volume-of-Fluid Method for Computing 3D and Axisymmetric Incompressible Two-Phase Flows. *J. Comput. Phys.*, 162(2):301–337, 2000.

[23] M. Sussman. A second order coupled level set and volume-of-fluid method for computing growth and collapse of vapor bubbles. *J. Comput. Phys.*, 187:110–136, 2003.

[24] S. P. van der Pijl, A. Segal, C. Vuik and P. Wesseling. A mass-conserving Level-Set method for modelling of multi-phase flows. *Int. J. Numer. Meth. Fluids*, 47:339–361, 2005.

[25] J. U. Brackbill, D. B. Kothe and C. Zemach. A continuum method for modeling surface tension. *J. Comput. Phys.*, 100(2):335–354, 1992.

[26] B. Lafaurie, C. Nardone, R. Scardovelli, S. Zaleski and G. Zanetti. Modelling Merging and Fragmentation in Multiphase Flows with SURFER. *J. Comput. Phys.*, 113(1):134–147, 1994.

[27] M. M. François, S. J. Cummins, E. D. Dendy, D. B. Kothe, J. M. Sicilian and M. W. Williams. A balanced-force algorithm for continuous and sharp interfacial surface tension models within a volume tracking framework. *J. Comput. Phys.*, 213(1):141–173, 2006.

[28] S. Popinet. An accurate adaptive solver for surface-tension-driven interfacial flows. *J. Comput. Phys.*, 228(16):5838–5866, 2009.

[29] J. Schlottke and B. Weigand. Direct numerical simulation of evaporating droplets. *J. Comput. Phys.*, 227:5215–5237, 2008.

[30] R. Fedkiw, T. Aslam, B. Merriman and S. Osher. A non-oscillatory Eulerian approach to interfaces in multimaterial flows (the ghost fluid method). *J. Comput. Phys.*, 152(2):457–492, 1999.

[31] T. G. Liu, B. C. Khoo and K. S. Yeo. Ghost fluid method for strong shock impacting on material interface. *J. Comput. Phys.*, 190:651–681, 2003.

[32] S. Karni. Multicomponent Flow Calculations by a Consistent Primitive Algorithm. *J. Comput. Phys.*, 112:31–43, 1994.

[33] R. Abgrall. How to Prevent Pressure Oscillations in Multicomponent Flow Calculations: A Quasi Conservative Approach. *J. Comput. Phys.*, 125:150–160, 1996.

[34] R. Saurel and R. Abgrall. A simple method for compressible multifluid flows. *SIAM J. Sci. Comp.*, 21(3):1115–1145, 1999.

[35] M. R. Baer and J. W. Nunziato. A two-phase mixture theory for the deflagration-to-detonation transition (DDT) in reactive granular materials. *Int. J. Multiphas. Flow*, 12(6):861–889, 1986.

[36] R. Saurel and R. Abgrall. A multiphase Godunov method for compressible multifluid and multiphase flows. *J. Comput. Phys.*, 150(2):425–467, 1999.

[37] A. Murrone and H. Guillard. A five equation reduced model for compressible two phase flow problems. *J. Comput. Phys*, 202(2):664–698, 2005.

[38] M. Rieber. *Numerische Modellierung der Dynamik freier Grenzflächen in Zweiphasenströmungen*. PhD thesis, Universität Stuttgart, 2004.

[39] G. K. Batchelor. *An Introduction to Fluid Dynamics*. Cambridge University Press, 1967.

[40] G. H. Miller and E. G. Puckett. A high-order Godunov method for multiple condensed phases. *J. Comput. Phys.*, 128:134–164, 1996.

[41] W. J. Rider and D. B. Kothe. Reconstructing Volume Tracking. *J. Comput. Phys.*, 141(2):112–152, 1998.

[42] M. Boger, F. Jaegle, R. Klein and C.-D. Munz. Coupling of compressible and incompressible flow regions using the multiple pressure variables approach. *Math. Meth. Appl. Sci.*, 2014. DOI: 10.1002/mma.3081.

[43] R. Abgrall and S. Karni. Computations of compressible multifluids. *J. Comput. Phys.*, 169:594–623, 2001.

[44] R. Caiden, R. P. Fedkiw and C. Anderson. A numerical method for two-phase flow consisting of separate compressible and incompressible regions. *J. Comput. Phys.*, 166(1):1–27, 2001.

[45] M. Rieber and A. Frohn. Navier-Stokes simulation of droplet collision dynamics. In *Proceedings of the Seventh International Symposium on Computational Fluid Dynamics*, 1997.

[46] M. Rieber and A. Frohn. A numerical study on the mechanism of splashing. *Int. J. Heat Fluid Fl.*, 20:455–461, 1999.

[47] M. Boger, J. Schlottke, C.-D. Munz and B. Weigand. Reduction of parasitic currents in the DNS VOF code FS3D. In *Proceedings of the 12^{th} Workshop on Two-Phase Flow Predictions*, 2010.

[48] M. Meier, G. Yadigaroglu, and B. L. Smith. A novel technique for including surface tension in PLIC-VOF methods. *Eur. J. Mech. B-Fluid*, 21(1):61–73, 2002.

[49] I. Ginzburg and G. Wittum. Two-Phase Flows on Interface Refined Grids Modeled with VOF, Staggered Finite Volumes, and Spline Interpolants. *J. Comput. Phys.*, 166(34):302–335, 2001.

[50] Y. Renardy and M. Renardy. PROST: A Parabolic Reconstruction of Surface Tension for the Volume-of-Fluid Method. *J. Comput. Phys.*, 183(2):400–421, 2002.

[51] A. Jafari, E. Shirani and N. Ashgriz. An improved three-dimensional model for interface pressure calculations in free-surface flows. *Int. J. Comput. Fluid D.*, 21(11):87–97, 2007.

[52] S. J. Cummins, M. M. François and D. B. Kothe. Estimating curvature from volume fractions. *Comput. Struct.*, 83(6-7):425–434, 2005.

[53] R. Courant, K. O. Friedrichs and H. Lewy. Über die partiellen Differentialgleichungen der mathematischen Physik. *Math. Ann.*, 100:32–74, 1928.

[54] R. J. Leveque. *Finite-Volume Methods for Hyperbolic Problems*. Cambridge University Press, 2004.

[55] B. van Leer. Towards the ultimate conservative difference scheme. V. A second-order sequel to Godunov's method. *J. Comput. Phys.*, 32:101–136, 1979.

[56] R. Fedkiw, X.-D. Liu and S. Osher. A General Technique for Eliminating Spurious Oscillations in Conservative Schemes for Multiphase and Multispecies Euler Equations. *Int. J. Nonlin. Sci. Num.*, 3:99–105, 2002.

[57] M. Boger, F. Jaegle and C.-D. Munz. A Pressure-Based Method for the Direct Numerical Simulation of Compressible Two-Phase Flows. In *Proceedings of the 24th European Conference on Liquid Atomization and Spray Systems (ILASS)*, 2011.

[58] M. Boger, F. Jaegle, B. Weigand and C.-D. Munz. A pressure-based treatment for the direct numerical simulation of compressible multiphase flow using multiple pressure variables. *Comput. Fluids*, 2014. http://dx.doi.org/10.1016/j.compfluid.2014.01.029.

[59] S. Fechter, F. Jaegle and V. Schleper. Exact and approximate Riemann solvers at phase boundaries. *Comput. Fluids*, 75:112–126, 2013.

[60] E. F. Toro. *Riemann Solvers and Numerical Methods for Fluid Dynamics: A Practical Introduction*. Springer, 2009.

[61] G. A. Sod. A Survey of Several Finite Difference Methods for Systems of Nonlinear Hyperbolic Conservation Laws. *J. Comput. Phys.*, 27:1–31, 1978.

[62] J. H. Park. *Ein konservatives MPV-Verfahren zur Simulation der Strömungen in allen Machzahlbereichen*. PhD thesis, Universität Stuttgart, 2003.

[63] H. Tang and T. Liu. A note on the conservative schemes for the Euler equations. *J. Comput. Phys.*, 218:451–459, 2006.

[64] S. Kudriakov and W. H. Hui. On a new defect of shock-capturing methods. *J. Comput. Phys.*, 227:2105–2117, 2007.

[65] J. J. Quirk. A contribution to the great Riemann solver debate. *Int. J. Numer. Meth. Fl.*, 18:555–574, 1994.

[66] T. W. Roberts. The Behavior of Flux Difference Splitting Schemes near Slowly Moving Shock Waves. *J. Comput. Phys.*, 90:141–160, 1990.

[67] B. Einfeldt, C.-D. Munz, P. L. Roe and B. Sjögreen. On Godunov-Type Methods near Low Densities. *J. Comput. Phys.*, 92:273–295, 1991.

[68] W. F. Noh. Errors for Calculations of Strong Shocks Using an Artificial Viscosity and an Artificial Heat Flux. *J. Comput. Phys.*, 72:78–120, 1978.

[69] M.-S. Liou and C. J. Steffen, Jr. A New Flux Splitting Scheme. *J. Comput. Phys.*, 107(1):23–39, 1993.

[70] M.-S. Liou. *Ten Years in the Making: AUSM-family*. National Aeronautics and Space Administration, Glenn Research Center, 2001.

[71] M.-S. Liou. A Sequel to AUSM: AUSM$^+$. *J. Comput. Phys.*, 129(2):364–382, 1996.

[72] P. L. Roe. Approximate Riemann Solvers, Parameter Vectors, and Difference Schemes. *J. Comput. Phys.*, 43:357–372, 1981.

[73] R. Liska and B. Wendroff. Comparison of several difference schemes on 1D and 2D test problems for the Euler equations. *SIAM J. Sci. Comput.*, 25(3):995–1017, 2003.

[74] R. Menikoff. Errors when shock waves interact due to numerical shock width. *SIAM J. Sci. Comput.*, 15(5):1227–1242, 1994.

[75] W. J. Rider. Revisiting Wall Heating. *J. Comput. Phys.*, 162:395–410, 2000.

[76] X. Y. Hu and B. C. Khoo. An interface interaction method for compressible multifluids. *J. Comput. Phys.*, 198(1):35–64, 2004.

[77] X. Y. Hu, N. A. Adams and G. Iaccarino. On the HLLC Riemann solver for interface interaction in compressible multi-fluid flow. *J. Comput. Phys.*, 228:6572–6589, 2009.

[78] H. Lamb. *Hydrodynamics*. Cambridge University Press, 1957.

[79] H. Weking, J. Schlottke, M. Boger, P. Rauschenberger, B. Weigand and C. -D. Munz. DNS of Rising Bubbles Using VOF and Balanced Force Surface Tension. In *High Performance Computing on Vector Systems 2010*, pages 171–184. Springer, 2010.

[80] C.-H. Chang and M.-S. Liou. A robust and accurate approach to computing compressible multiphase flow: Stratified flow model and AUSM$^+$-up scheme. *J. Comput. Phys.*, 225:840–873, 2007.

[81] D. A. Kopriva. *Implementing Spectral Methods for Partial Differential Equations*. Springer, 2009.

[82] C. Merkle and C. Rohde. The sharp-interface approach for fluids with phase change: Riemann problems and ghost fluid techniques. *ESAIM-Math. Model. Num.*, 41(6):1089–1123, 2007.

[83] C. W. Wang, T. G. Liu and B. C. Khoo. A real ghost fluid method for the simulation of multimedium compressible flow. *SIAM J. Sci. Comp.*, 28(1):278–302, 2006.

[84] C.-D. Munz and T. Westermann. *Numerische Behandlung gewöhnlicher und partieller Differenzialgleichungen*. Springer, 3rd edition, 2012.

List of Tables

List of Figures